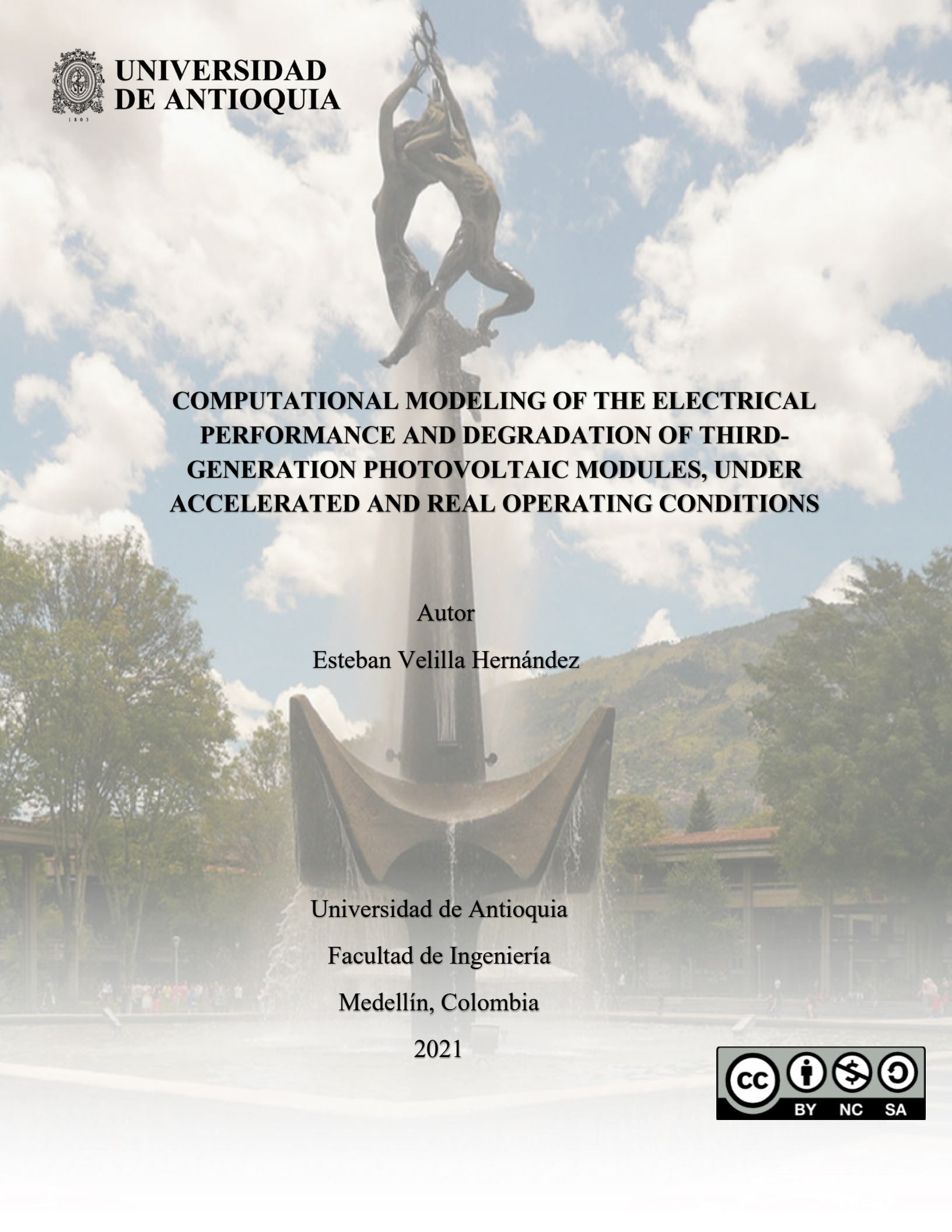

UNIVERSIDAD DE ANTIOQUIA

COMPUTATIONAL MODELING OF THE ELECTRICAL PERFORMANCE AND DEGRADATION OF THIRD-GENERATION PHOTOVOLTAIC MODULES, UNDER ACCELERATED AND REAL OPERATING CONDITIONS

Autor

Esteban Velilla Hernández

Universidad de Antioquia

Facultad de Ingeniería

Medellín, Colombia

2021

Computational Modeling of the Electrical Performance and Degradation of Third-generation Photovoltaic Modules, Under Accelerated and Real Operating Conditions

Esteban Velilla Hernández

Tesis presentada como requisito parcial para optar al título de:

Doctor en Ingeniería de Materiales

Asesor:

Franklin Jaramillo Isaza, Ing. PhD

Línea de Investigación:

Energía, Celdas Solares Fotovoltaicas de Última Generación

Grupo de Investigación:

Centro de Investigación, Innovación y Desarrollo de Materiales, CIDEMAT

Universidad de Antioquia

Facultad de Ingeniería

Medellín, Colombia

2021.

Acknowledgments

Firstly, I am very grateful to the people linked directly or indirectly in this process. I particularly thank my family for their unending love, support, and patience, to my wife Carolina, son Daniel and daughter Violeta. They are everything to me.

I thank my supervisor Franklin Jaramillo for his leadership, enthusiasm, and support. He was always ready and able to give guidance, feedback, and advice, also many thanks to the members of the research group. I particularly thank Daniel Ramírez, Rafael Betancur, and Ignacio Uribe for the technical discussions and perovskite solar cell fabrication training.

Further, I am very grateful to Juan B. Cano for the unconditional support, technical discussions, and suggestions related to various topics included in this project. To help me develop the I-V curve tracers and Solar Cell Outdoor Performance Laboratory of the University of Antioquia (OPSUA), vital tools for evaluating the outdoor performance of photovoltaic devices.

Thank Cesar Londoño, Santiago Restrepo, and Keonny Jimenez for the unconditional support and essential role in developing the I-V curve tracers and Solar Cell Outdoor Performance Laboratory of the University of Antioquia (OPSUA).

Thank German Moreno, Jaime Valencia, Fernando Villada, and Felix Echeverria for motivating me to roll on in this fantastic adventure.

Finally, I would like to thank Iván Mora Seró for his encouragement and helpful reviews. He played a crucial role in my doctoral training and research internship. He motivated and encouraged me to study the ideality factor theory, a central aspect of this work. Moreover, I am very grateful to the University Jaime I (UJI) members and technical staff. I particularly thank Felipe Laporta, Jorge Caram, Sofia Masi, and Andrés Gualdrón for the friendship, support, and extraordinary experiences during the research internship.

Thank the University of Antioquia for the study commission's support and Colombia's Administrative Department of Science, Technology and Innovation (COLCIENCIAS) for the national doctoral scholarship number 727-2015 (contract No. FP44842-124-2017). Also, I am grateful for the Colombia Scientific Program's support within the framework of the call Ecosistema Científico (Contract No. FP44842- 218-2018).

Abstract

This work evaluated the perovskite solar technology's outdoor performance. An emerging technology that was not commercial at the beginning of this work (Velilla et al., 2017). Therefore, minimodules with an inverted mesoporous $MAPbI_3$ structure ($N_iO_x/Al_2O_3/MAPbI_3$/PCMB/rhodamine/Au), were fabricated in a drybox by spin coating (Ramirez et al., 2019). The devices formed for 4 cells interconnected in series and 8.0 cm^2 of an active area were fabricated on ITO substrates of 5 x 5 cm and manually encapsulated with ethylene-vinyl acetate (EVA). These were analyzed by impedance frequency response and ideality factor following the procedure shown in (Yoo et al., 2021, 2020), providing physical insight into the recombination mechanism dominating the performance and fully characterize the devices under indoor conditions.

Accordingly, a methodology based on the international standard IEC 61853-1 to evaluate the perovskite technology's outdoor performance was proposed (Velilla et al., 2019b) because no international standards have been fully established, and most published works have focused on laboratory-scale cells (i.e., 1 cm^2 or smaller in size). This methodology was implemented as Python's functions (scripts) in a remote server to estimate the photovoltaic device's outdoor performance. Hence, the developed I-V curve tracers (Cano et al., 2015) were synchronized with a weather station (to record the irradiance levels and ambient/device temperatures). This procedure allowed validated the power rating conditions for commercial modules of different technologies such as silicon, HIT, and CIGS according to the manufacturers' reported values in its datasheets (Velilla et al., 2019a). Then, the procedure was extended to evaluate perovskite minimodules performance under outdoor conditions.

The perovskite minimodules outdoor evaluation under natural sunlight without a tracker in the Solar Cell Outdoor Performance Laboratory (OPSUA, University of Antioquia, Medellín-Colombia) allowed observation of three maximum power (P_{max}) evolution patterns, named convex, linear, and concave patterns because of the exhibited shapes. In this sense, all the analyzed minimodules can be statistically associated with one of these three patterns, commonly described for degradation processes in the literature to study possible degradation paths and estimate the failure time. Therefore, to analyze these degradation behaviors, well-known statistical models such as linear regression models were used to estimate the degradation rate and lifetime (T_{80}).

Relating to ideality factor also called quality factor or shape curve factor, which is the most reported parameter for different solar cell technologies. This parameter has been used to define the electrical behavior of solar devices due to its relationship with conduction, transport, recombination, and behavior at interface junctions, providing physical insight into the recombination mechanism dominating the performance. Consequently, the changes in n_{ID} could be correlated with the recombination mechanisms or degradation processes occurring in the device, highlighting the importance of this parameter to complete the device's characterization.

Therefore, the n_{ID} values were estimated from the relationship between the open-circuit voltage and light intensity, from the impedance frequency response (IFR) under different light intensities calculating the recombination resistance (R_{rec}) (Yoo et al., 2021, 2020), and fitting the I-V curve to one-diode model to extract this parameter. In these cases, an agreement has been shown between the n_{ID} value estimated from the recombination resistance extracted through IFR analysis and the value calculated from V_{oc} at different light intensities (Almora et al., 2018; Yoo et al., 2020). Therefore, an Autolab's procedure was implemented to record the device's V_{oc} and IFR as a light function. Besides, to estimate the R_{rec} fitting the IFR to a circuit model or extract the one-diode model's parameters fitting the I-V curve to this model, a global optimization process involving a genetic algorithm (GA) and the simplex method was implemented, following the previous work's methodology (Velilla et al., 2018).

Moreover, due to the day-night cycles, including dawn and noon conditions, which can naturally provide a broad range of illumination conditions, it was proposed to estimate n_{ID} from the open-circuit voltage (V_{oc}) dependence on irradiance and ambient temperature (outdoor data). Consequently, the changes in n_{ID} could be correlated with the recombination mechanisms or degradation processes occurring in the device. In this context, it was observed that the three different degradation patterns identified for P_{max} can also be identified by n_{ID}. Hence, these three

representative power loss tendencies were compared with their corresponding ideality factor (n_{ID}). To this end, we defined Tn_{ID2} as the time at which n_{ID} first reaches a value of 2, with a physical meaning related to the transition point between bulk SRH recombination through a single level to recombination through multiple levels because of device degradation. Thus, based on the linear relationship between T_{80} and the time to reach n_{ID}=2 (Tn_{ID2}) is demonstrated that n_{ID} analysis could offer important complementary information with important implications for this technology's outdoor development.

Finally, we must admit that the photovoltaic industry has invested efforts in developing diagnostic tools intended to improve the energy production's reliability and the installations' safety. In this sense, although n_{ID} has not been employed to monitor device evolution to see how the relevant processes evolve, for example, in degradation, this work proposed a methodology to characterize the technology's outdoor performance evolution and improve the conventional P_{max} analyses, using the n_{ID} as a figure of merit (Velilla et al., 2021). This methodology could be quickly adapted by research groups to estimate the status and evaluate the device's performance evolution and by the industrial sector to develop equipment or tools to perform diagnostic devices.

List of Publications

Velilla, E., Jaramillo F., Mora-Seró, I., 2020. High-throughput analysis of the ideality factor to evaluate the outdoor performance of perovskite solar minimodules. Nature Energy 6, 54–62 (2021). DOI: https://doi.org/10.1038/s41560-020-00747-9.

Yoo, S.-M., Lee, S., Kim, G., **Velilla Hernández, E.**, Mora-Seró, I., Yoon, S.J., Shin T., Lee, Sel-Hi, Seok-Hoon, A., Min-Kyoung, S., Kim, M. and Lee, H.J., 2020. Preparation of Nanoscale Inorganic CsPbIxBr3-x Perovskite Photosensitizers on the Surface of Mesoporous TiO2 Film for Solid-State Sensitized Solar Cells. 551, 149387, 2021. Applied Surface Science. ISSN 0169-4332. DOI: https://doi.org/10.1016/j.apsusc.2021.149387.

Yoo, S.-M., Lee, S., **Velilla Hernández, E.,** Kim, M., Kim, G., Shin, T., Nazeeruddin, M.K., Mora-Seró, I., Lee, H.J., 2020. Nanoscale Perovskite-Sensitized Solar Cell Revisited: Dye-Cell or Perovskite-Cell? ChemSusChem 13, 2571–2576. https://doi.org/10.1002/cssc.202000223.

Velilla, E., Cano, J.B., Jaramillo, F., 2019. Monitoring system to evaluate the outdoor performance of solar devices considering the power rating conditions. Solar Energy 194, 79–85. https://doi.org/10.1016/j.solener.2019.10.051.

Velilla, E., Ramirez, D., Uribe, J.-I., Montoya, J.F., Jaramillo, F., 2019. Outdoor performance of perovskite solar technology: Silicon comparison and competitive advantages at different irradiances. Sol. Energy Mater. Sol. Cells 191, 15–20. https://doi.org/10.1016/j.solmat.2018.10.018.

Ramirez, D., **Velilla, E.,** Montoya, J.F., Jaramillo, F., 2019. Mitigating scalability issues of perovskite photovoltaic technology through a p-i-n meso-superstructured solar cell architecture. Sol. Energy Mater. Sol. Cells 195, 191–197. https://doi.org/10.1016/j.solmat.2019.03.014.

Velilla, E., Cano, J., Jimenez, K., Valencia, J., Ramirez, D., Jaramillo, F., 2018. Numerical Analysis to Determine Reliable One-Diode Model Parameters for Perovskite Solar Cells. Energies 11, 1963. https://doi.org/10.3390/en11081963.

Velilla, E., Restrepo, S., Jaramillo, F., 2017. Cluster analysis of commercial photovoltaic modules based on the electrical performance at standard test conditions. Solar Energy. 144, 335–341. https://doi.org/10.1016/j.solener.2017.01.037.

Table of Contents

Table of Figures

1. Introduction

Perovskite solar cells (PSC) are expected to significantly impact the future if they can provide significant performance outdoors. Outdoor conditions are highly demanding, as they are characterized by day-night, seasonal, and weather cycles that correspond to drastic variations in irradiation, temperature, and moisture. While accelerated performance tests help predict the devices' behavior, continuous outdoor tests are also required to provide information on the applicability of this technology in the real world. The outdoor exploitation of solar devices requires encapsulation to protect the electrodes and active areas of cells against the environment, avoid corrosion processes, increase the electrical insulation to eliminate leakage currents, and provide thermal and mechanical support (Hasan and Arif, 2014). In this context, international standards such as IEC 61215 suggest various accelerated tests intended to identify potential failures in silicon photovoltaic modules (broken interconnects, cracked cells, delamination, dielectric breakdown, bypassed diodes, and corrosion). Thus, based on the experience gained in recent decades through such accelerated tests and field evaluations, these failures in photovoltaic modules have been correlated with various degradation modes, such as corrosion, delamination, discoloration, glass breakage, cell cracking, potential-induced degradation, current leakage, ion migration, hot spots, and soiling (Oliveira et al., 2018; Wang et al., 2013). Nevertheless, because the standards do not include all possible degradation modes and, in real operation, photovoltaic devices can be affected by different degradation modes simultaneously, it is not always possible to estimate the real lifetime from these tests (Osterwald and McMahon, 2009).

In emerging technologies such as PSC, no international standards have been fully established, and most published works have focused on laboratory-scale cells (i.e., 1 cm^2 or smaller in size). The first certificated minimodule of this technology was reported in 2016 by SJTU team, which corresponded to 12.1% of efficiency, 10 serial cells, and an illuminated area of 36.13 cm^2 (Green et al., 2017). Toshiba reported the last certified PSC module with an efficiency of 16.1%, 55 serial cells, and an illuminated area of 802 cm^2 (Green et al., 2020). Consequently, various upscaling works have been published (Green et al., 2018; Hu et al., 2019; Qiu et al., 2019), and different methods and materials have been used to evaluate the stability and degradation performance of this technology (Anoop et al., 2020; Cheacharoen et al., 2018; Domanski et al., 2018; Holzhey and Saliba, 2018; Tress et al., 2019; Yang et al., 2015). In this regard, a broadly-supported consensus statement on reporting data related to stability assessment was recently published, highlighting certain particularities of PSC technology that must be taken into account (Khenkin et al., 2020). For instance, in contrast to mature photovoltaic technologies such as Si and GaAs, PSCs show performance loss reversibility under day-night cycles (Domanski et al., 2017; Khenkin et al., 2018); a hysteresis effect in the current-voltage (I-V) curves, which could induce errors in the performance determination (Christians et al., 2015); and a lower dependence of performance and V_{oc} on temperature (Schwenzer et al., 2018).

While these peculiarities of PSC could be seen as drawbacks for their systematic analysis, they also provide new opportunities for PSC's characterization (Hoye et al., 2017). This technology is in its infancy, and there are scarce statistical data available for large devices operated outdoors (Hu et al., 2019). Therefore, there is not enough available data to fully establish or identify the degradation modes and mechanisms of PSCs and their impact on outdoor performance evolution. Moreover, under high-irradiance conditions, PSCs show significant differences from conventional Si cells. It has been demonstrated for perovskite minimodules operating outdoors (Velilla et al., 2019b) and for non-encapsulated solar cells under simulated weather conditions in the laboratory (Tress et al., 2019). These results indicate that PSCs show lower correlations of their performance and open-circuit voltage (V_{oc}) with temperature than other commercial technologies, such as silicon (Deng et al., 2019), for which the deleterious effects of temperature on performance are well known (Green et al., 1985; Osterwald et al., 1987). This difference in temperature sensitivity is an essential aspect of PSC technology to consider.

Conventionally, the performance evolution of solar cell devices is monitored through the systematic measurement of I-V curves as a function of the temperature and illumination conditions. In the laboratory, it is relatively easy to set up tests to track the performance, for instance, at the maximum power point; however, such control is intrinsically unreasonable outdoors. The illumination and temperature variations induced by day-night, seasonal, and weather conditions necessitate a systematic analysis of a high quantity of data, depending on the measurement sampling rate and exposure time (Wang et al., 2018). Hence, in such power loss studies, it is common to correct the I-V curves for temperature and irradiance in accordance with the standard test conditions (STC, corresponding to an irradiance of 1000 W/m^2 and a module temperature of 25 °C). However, such conditions are difficult to reach outdoors (Velilla et al., 2019a). Although the conventional method of monitoring outdoor module performance based on I-V curves produces rich numerical data, it offers no direct indication of the physical processes occurring in the device and thus provides no information about degradation modes.

In this context, to evaluate the photovoltaic device's lifetime, a parameter that refers to the time at which the device reaches 80% of its initial rated power (T_{80}) is commonly used as a figure of merit. T_{80} depends on various factors, such as the materials and procedures used for device fabrication, cell interconnects, weather conditions, seasonal variations, installation conditions, shading and soiling effects, and electrical mismatch between cells, among others (Makrides et al., 2014). This parameter is commonly obtained from the relationship between the maximum power and time in a long-term analysis of a device under real outdoor operating conditions. Moreover, considering that the performance over time shows seasonal behavior and a gradual performance loss tendency, T_{80} has been commonly fitted using statistical methods, such as linear regression, to estimate the degradation rate (Phinikarides et al., 2014). As a complementary analysis to this scheme, it is proposed to take advantage of the outdoor conditions' variability to track the perovskite minimodule performance by the determination of ideality factor (n_{ID}), also called the quality factor or shape curve factor.

Despite the potential of n_{ID}, this parameter has not been employed to monitor device evolution over time to see how the relevant processes evolve, for example, in degradation. Therefore, this work proposed to take advantage of the weak dependence of V_{oc} on T in PSCs (Schwenzer et al., 2018; Tress et al., 2019; Velilla et al., 2019b) to calculate n_{ID} and use it as a figure of merit for monitoring and characterizing the outdoor performance of this technology. Hence, day-night cycles, including dawn and noon conditions, can naturally provide a broad range of illumination conditions, allowing n_{ID} to be determined. Moreover, taking advantage of this exciting parameter to determine the physical processes acting on devices, this parameter was linked with the degradation modes. For this purpose, the outdoor performance for $MAPbI_3$ minimodules was tracked, recording the evolution of the maximum power (P_{max}) under power rating conditions suggested by the IEC61853-1 standard, precisely the nominal operating cell temperature (NOCT) conditions, to compare the resulting data with the n_{ID} evolution estimated only from V_{oc}, light irradiance, and ambient temperature. It was showing that this new methodology identifies similar features to those found using the classical approach based on P_{max}, enabling tracking of the physical processes occurring in the device. Finally, the linear relationship between the time at which the module reaches $n_{ID} = 2$ (Tn_{ID2}) and T_{80}, suggested the complementarity of these two parameters. This complementarity has important implications for improving the characterization and understanding of the degradation processes and, consequently, for the PSC's outdoor optimization.

2. MAPI Perovskite Devices Fabrication and Characterization

This chapter presented the fabrication and electrical performance characterization of $MAPbI_3$ minimodules of 8.0 cm^2 in size formed of 4 cells interconnected in series, with an inverted mesoporous structure ($ITO/N_iO_x/Al_2O_3/MAPI/PCMB/Rhodamine/Au$, **Figure 2-1**a-b). This structure has been demonstrated to be feasible for fabricating large-area devices up to 100 cm^2 in dry-box conditions by spin coating (Ramirez et al., 2019; Velilla et al., 2019b). In this structure, the incorporation of NiO_x and mesoporous layer (Al_2O_3) improves the reproducibility for fabrication over large-areas and reduces hysteresis (Ciro et al., 2017b; Ramirez et al., 2018a), while the incorporation of rhodamine improves the electronic effects (Ciro et al., 2017a). Moreover, to evaluate these devices at outdoor conditions, the electrical contacts (ITO and Au contact) were extended using an adhesive silver tape and encapsulated in a glovebox with ethylene-vinyl acetate (EVA)/glass. The borders were covered with epoxy resin to minimize the direct exposure of the EVA (**Figure 2-1**c). Finally, fabricated devices were characterized by impedance frequency response (IFR) and ideality factor (n_{ID}). Therefore, an experimental procedure was implemented to estimate the n_{ID} from the relationship between V_{oc} and light intensity and from the relationship between the bias and R_{rec} in IFR test. This procedure was used in previous works (Yoo et al., 2021, 2020), allowing identification of the device's recombination mechanism and demonstrating an excellent agreement with the n_{ID} values calculated for both methodologies. Therefore, it was possible to identify the Shockley-Read-Hall (SRH) recombination mechanism dominating the devices, based on the n_{ID} values ranged between 1 and 2.

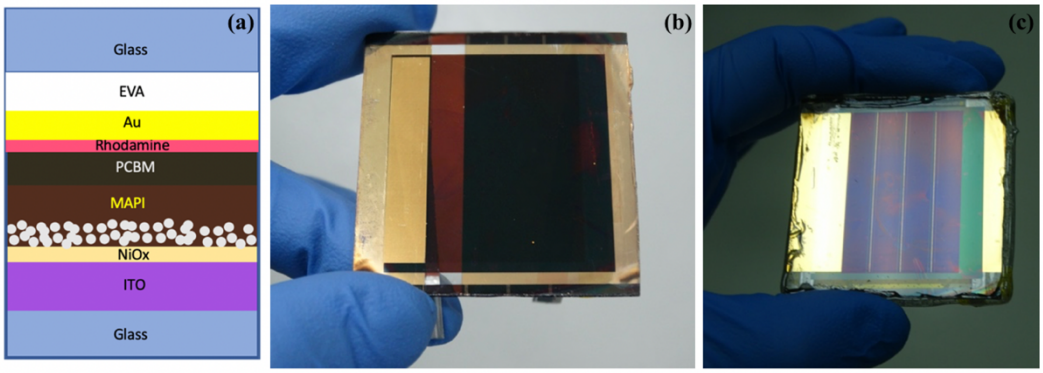

Figure 2-1. **MAPI devices**.
a) *scheme of layers involved in the devices.* ***b)*** *unencapsulated solar cell and* ***c)*** *encapsulated minimodule. Devices were fabricated on ITO substrate of 5 x 5 cm.*

2.1 Device Fabrication

2.1.1 Perovskite Solar Cells

The spin coating procedure carried out in dry-box conditions enables us to obtain uniform films of perovskite and interlayers also on large areas substrates, as was mentioned in (Ramirez et al., 2019). Thus, similar conditions related to the preparation of precursor solution and spin-coating parameters were exploited to deposit each layer and fabricate the whole device on an ITO substrate of 5 x 5 cm.

2.1.1.1 Layers Deposition

The NiO_x hole transporting layer was dynamically spin-coated at 3000 rpm for 30 s using a concentration of 23 mg/mL in deionized water. The nanoparticles of NiOx were synthesized by our laboratory personnel using the chemical precipitation method, as was mentioned in (Ciro et al., 2017b). The mesoporous layer of Al_2O_3 was dynamically spin-coated at 4000 rpm for 30 s using a commercial alumina nanoparticles dispersion diluted in isopropanol with a ratio of 1:5. MAPI layer was dynamically spin-coated at 3000 rpm for 30 s, by using a molar

ratio of 1.06 between methyl ammonium (MAI) and lead iodide (P_bI_2), dissolved in acetonitrile/methylamine solvent. A surface treatment with methyl ammonium chloride (5 mg/mL in IPA) was carried out by dynamical spin-coated at 4000 rpm for 30 s. Next, the substrate was thermally annealed at 100 °C for 10 min. PCBM was dynamically spin-coated at 2000 rpm using a concentration of 20 mg/mL in chlorobenzene. Rhodamine was dynamically spin-coated at 4000 rpm using a concentration of 0.5 mg/mL in anhydrous ethanol. Finally, the contact layer of gold was thermally evaporated under vacuum at 0.1 nm/s, **Figure 2-1**.

The complete characterization of the MAPI layer, which included a solvent treatment with methyl ammonium chloride (MACl), was shown in previous works (Ramirez et al., 2019), remarking the advantage of incorporating the Al_2O_3 layer to avoid pin-holes and increase the reproducibility in the fabrication process. In this context, **Figure 2-2** shows the top-view SEM images taken at different locations of the perovskite film deposited on the top of NiO_x/Al_2O_3 substrates of 10 x 10 cm, which were cut on pieces of 2x8 cm. Therefore, it was possible to observe pin-holes in the film deposited on the top of the planar NiO_x substrate (**Figure 2-2**a). At the same time, the morphologies improve on the top of the mesoporous layer (**Figure 2-2**d-f), indicating a more uniform film in the case of the mesoporous device due that the Al_2O_3 layer completely covers the ITO layer.

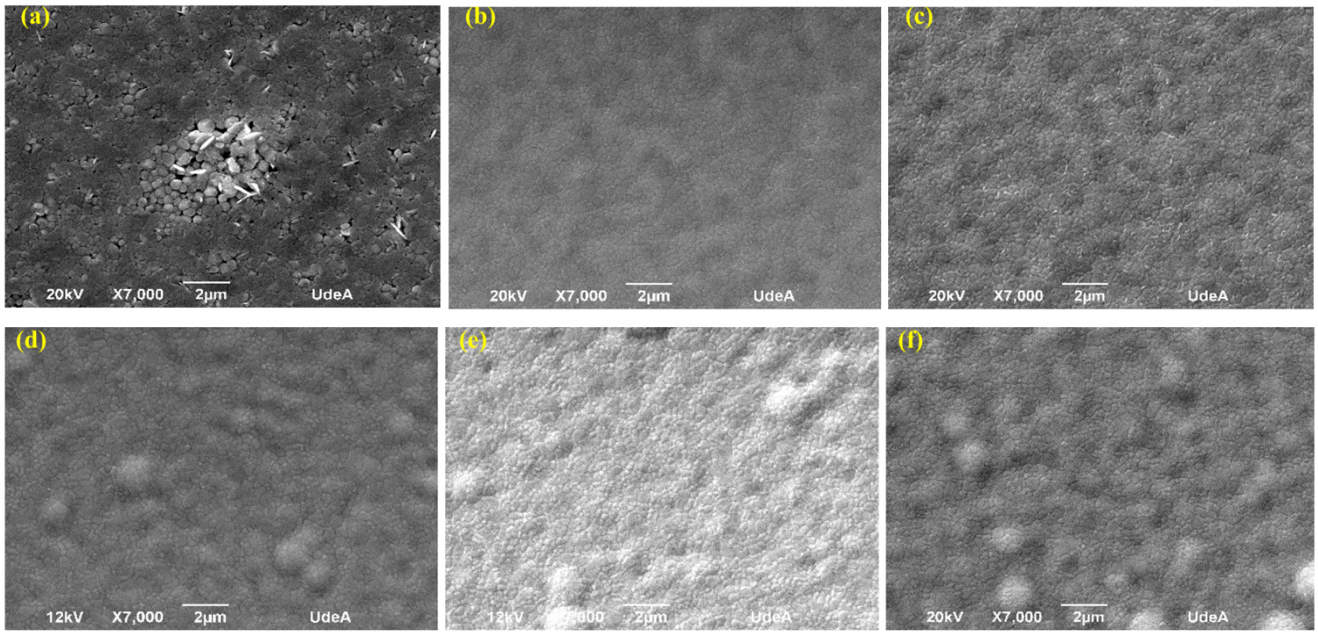

Figure 2-2. SEM of MAPI layer deposited on ITO substrate of 10 x 10 cm.

a-c) *related to a perovskite layer on the planar structure, being evident the pin-holes on the sample (a).* ***d-f)*** *related to a perovskite layer on top of the mesoporous layer, which allowed to fully cover the substrate and obtained homogenous layers. a) and d) on the top of the samples.* ***b)*** *and* ***e)*** *on the center of the samples and* ***c)*** *and* ***f)*** *on the bottom of the samples. These SEM corresponding to pieces of 2 x 8 cm from the central region.*

Figure 2-3 shows the cross-section SEM images of layers deposited on ITO substrate of 5 x 5 cm to validate aspects related to morphology and layers thickness. From these SEM images, it is observed the thickness of the NiO_x and the mesoporous layer of approximately 20 nm and 100 nm, respectively. Also, it is observed that the mesoporous layer covers the NiO_x layer creating a uniform layer between MAPI and the hole transport layer. On the other hand, ***Figure 2-4*** shows some representative AFM images of the layers on the NiO_x film's top. From this, it is possible to observe the effect of incorporating different layers, which help to fill spaces or passive defects on the previous layers, reducing the roughness of the final films based on the lower deviation measured (STD) on the region evaluated.

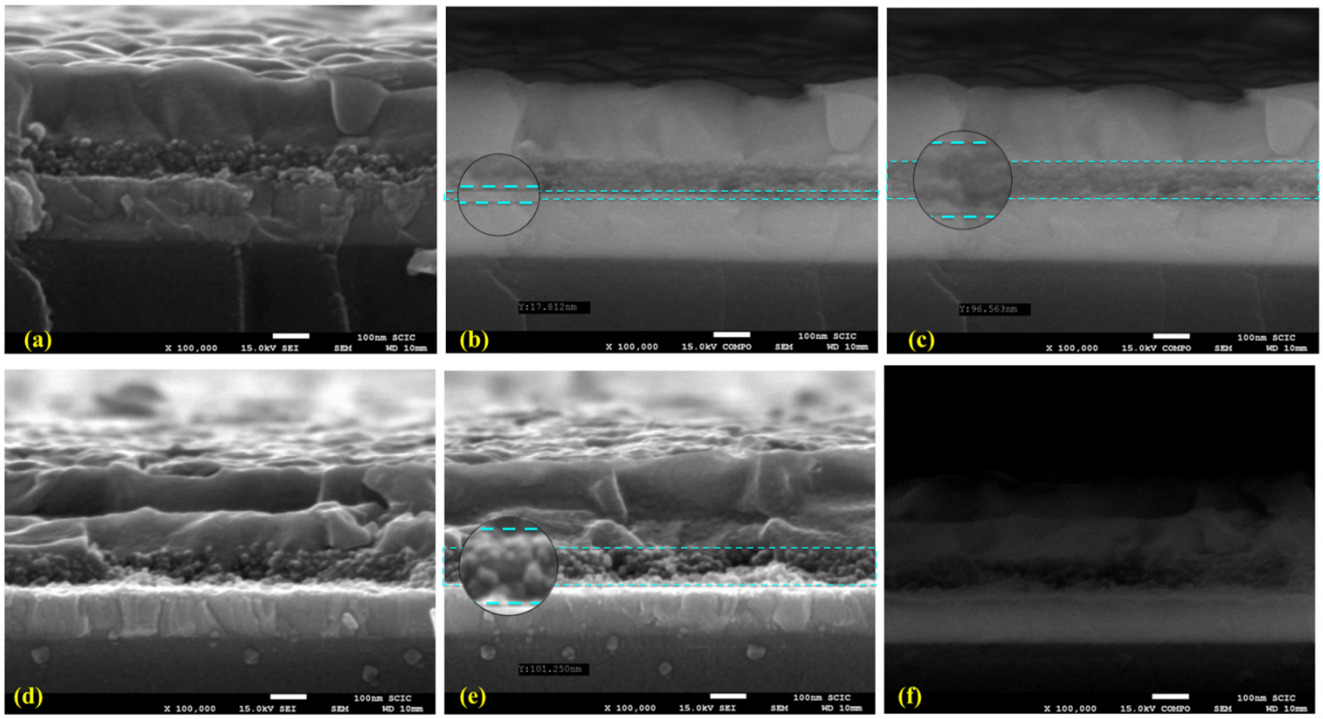

Figure 2-3. Cross-section SEM images of MAPI mesoporous devices deposited on ITO substrate of 5 x 5 cm. ***a)*** *intended to illustrate the layer morphology.* ***b)*** *intended to illustrate the thickness of the NiO_x layer of approximately 20 nm.* ***c)*** *intended to illustrate the thickness of the mesoporous layer of approximately 100 nm.* ***d-f)*** *related to another sample.* ***d)*** *intended to illustrate the effect of depositing the PCBM layer on MAPI.* ***e)*** *the thickness of mesoporous layer (Al_2O_3) and* ***f)*** *secondary electrons image of the image showed in e.*

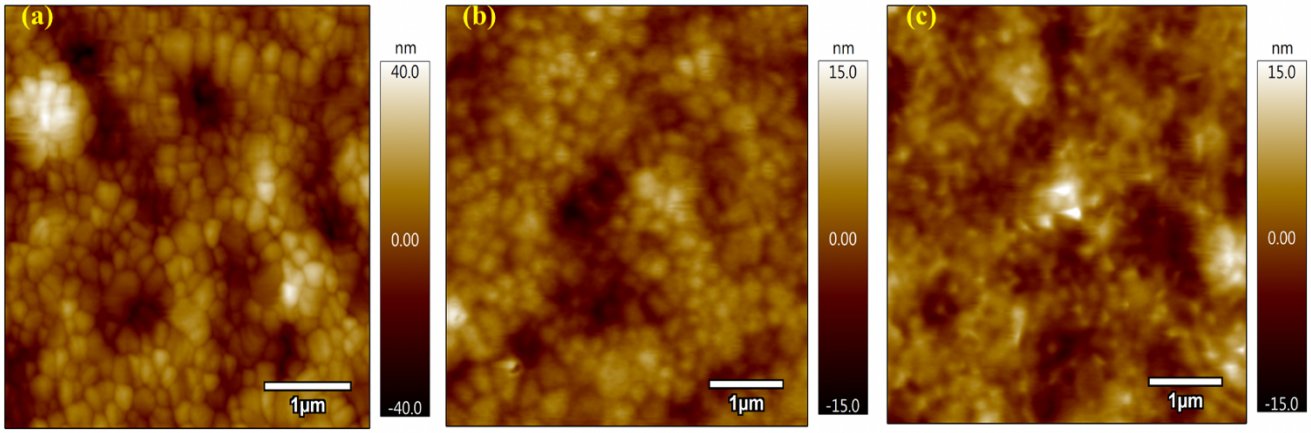

Figure 2-4. AFM of layers involved in the device.
Corresponding ***a)*** *to NiO_x/Al_2O_3/MAPI (STD=10.181nm).* ***b)*** *to NiO_x/Al_2O_3/MAPI/PCMB (STD=3.063nm) and* ***c)*** *to NiO_x/Al_2O_3/MAPI/PCMB-Rhodamine (STD=3.461nm). The layers were deposited on ITO subtracted of 5x5 cm.*

2.1.1.2 Area Effect on the Electrical Performance

Once uniform layers were obtained on ITO substrate of 5 x 5 cm, solar cells of MAPI inverted structure were fabricated, changing the active areas between 1 and 11.2 cm^2, ***Figure 2-5***a-b. A laser etching on the ITO substrate was performed on the borders (width of 0.5 cm) to limit the active area. Therefore, the ITO effective area was 16 cm^2. Finally, regarding the contact electrodes width of 0.7 cm for ITO and 0.5 for gold (left part and right part on ***Figure 2-5*** a-b), the maximum active area for the device was limited to 11.2 cm^2. ***Figure 2-5***c shows some representative I-V curves to illustrate the electrical operative range of the variables involved in the fabricated

devices' performance. It is to highlight that the I-V curves were measured using an Oriel Sol3A sun simulator and a 4200SCS Keithley system, being the maximum current limit of 120 mA. For that reason, the maximum active area of the cell was limited to 10 cm^2.

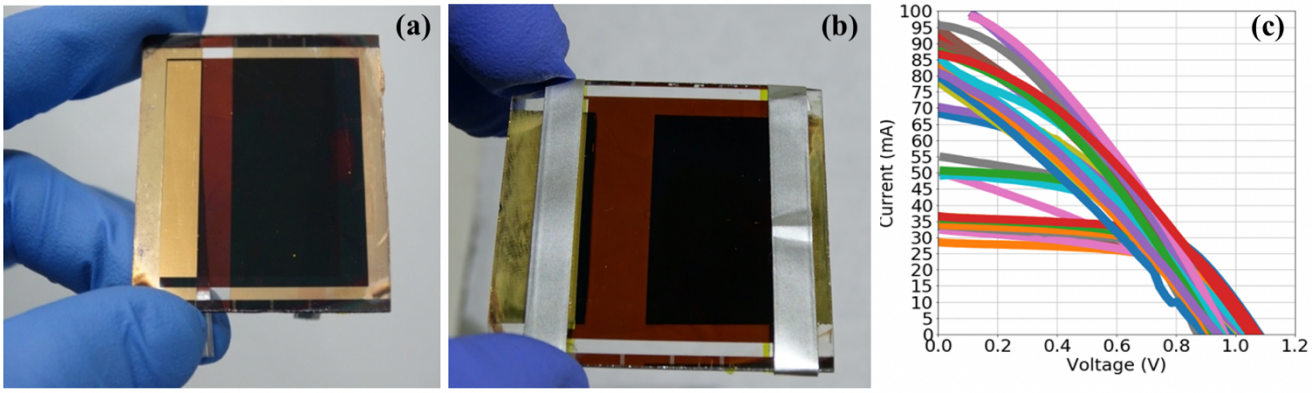

Figure 2-5. Solar cell fabricated on ITO substrate of 5 x 5 cm.
a) *photo of the fabricated device with an active area of approximately 8.4 cm^2.* ***b)*** *photo of the fabricated device with an active area of approximately 7.0 cm^2. The photo shows the silver tape used to extend the electrical contacts.* ***c)*** *Representative I-V curves of perovskite solar cells (monolithic) to illustrate the electrical performance of devices according to active areas ranging between 2 and 11 cm^2.*

Figure 2-6 shows the parameters extracted from the I-V curves in the form of scatter plots. These plots included trend lines corresponding to the fitted second-order polynomial to visually guide the effect of the area on the electrical performance. From these results, it is easy to observe that larger active areas correlated with higher P_{max} and lower efficiencies (***Figure 2-6***a-b). The areas of approximately 2 cm^2 correlated with higher efficiencies (greater than 10 %) and higher FF (greater than 50%), ***Figure 2-6***a-c. Also, the behavior shown by P_{max} and I_{sc} as a function of area (***Figure 2-6***d) suggested a stabilization trend as the active area increase, pointing to the performance losses because of the larger areas.

On the other hand, because similar V_{oc} values were obtained for the large-area solar cells and small-area solar cells ranging between 0.09 and 0.52 cm^2 as was shown in (Ramirez et al., 2019), the area effect on the V_{oc} could be neglected (***Figure 2-6***e). These results mainly suggested that similar perovskite layer thickness was obtained for the active areas up to 9 cm^2 (as can be seen in ***Figure 2-3*** and ***Figure 2-4***). Finally, the linear relationship between V_{oc} and I_{sc} illustrated the central aspect related to the ITO losses (***Figure 2-6***f). Higer I_{sc} correlates with lower V_{oc} (involving in the large areas), while higher V_{oc} correlates with lower I_{sc} (involving in the smaller areas). This fact suggested that the drop in V_{oc} is related to ohmic resistances (series resistances). This aspect is evidenced in the behavior of the I-V curves near the V_{oc} (***Figure 2-5***c).

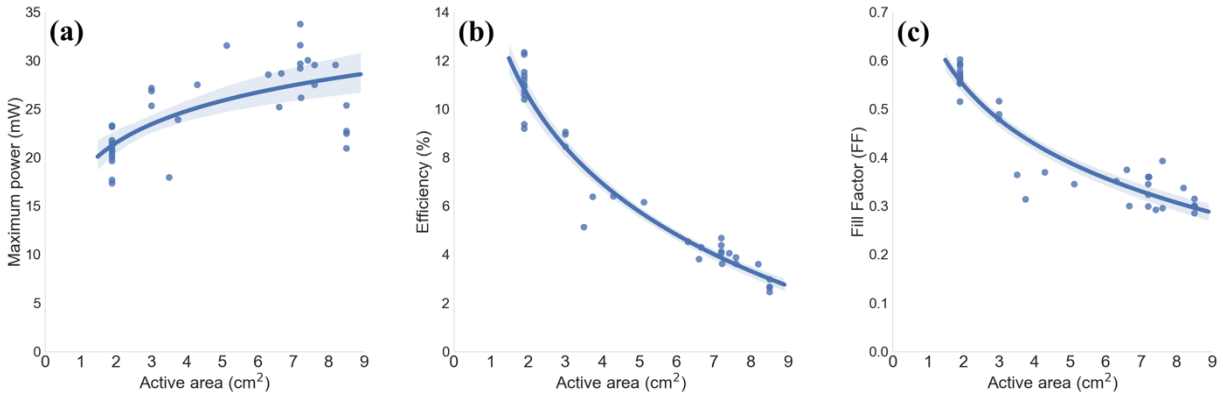

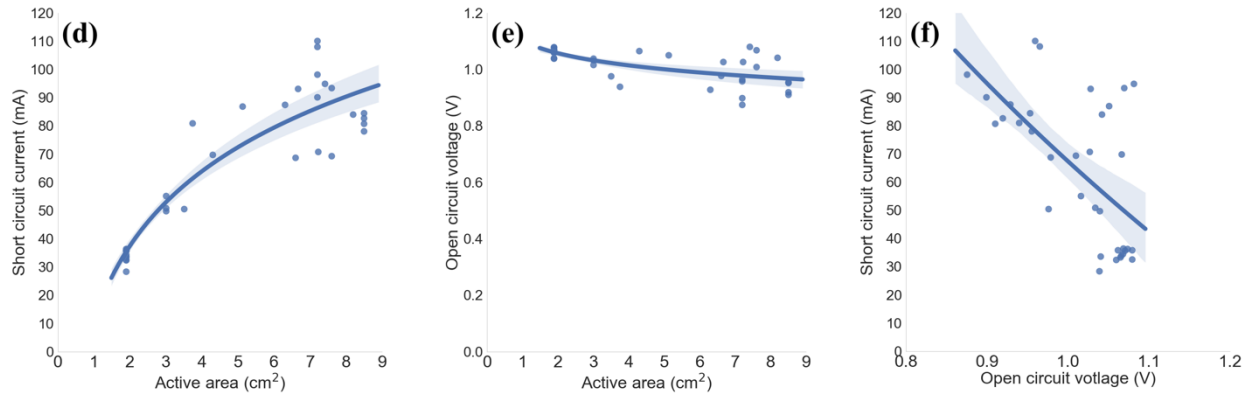

Figure 2-6. Effect of the active area on the electrical performance of solar cells.
Corresponding to ***a)*** *the maximum power.* ***b)*** *the efficiency.* ***c)*** *the fill factor.* ***d)*** *the short-circuit current.* ***e)*** *the open-circuit voltage and* ***f)*** *the relationship between the open-circuit voltage and short circuit current. The dots correspond to the data, and continuous lines correspond to the data fit (second-order polynomial functions).*

2.1.2 Perovskite Solar Minimodules

Despite that perovskite technology is an emerging technology, different works in the literature allowing the determination of the architecture, area, number of cells, and electrical performance in the upscaling of PSC devices (Green et al., 2018; Hu et al., 2019; Qiu et al., 2019). Highlighting that most of these devices used three scribe lines or patterns (P1, P2, and P3) to interconnect the cells in series. This technique is widely employed in other thin-film photovoltaic technologies as silicon, CIGS, and polymer (Booth, 2010; Harald et al., 2012), ***Figure 2-7***a-b.

In the case of perovskite cell interconnection, a complete description of these patterns was shown in (Moon et al., 2015). Briefly, the P1 scribe line is performed on the transparent conductive oxide layer (ITO or FTO) to limit the sub-cells area. The P2 scribe line is performed on the charge transport layers (electron and hole layers) and perovskite layer, intended to clear the ITO or FTO layer and allow interconnection between the back electrode and the charge transport layers. Finally, the P3 scribe is performed to remove the back-contact layer and separate the cells. Therefore, the active area is limited by P1 and P3 lines. In contrast, the death-area is limited by P3 and P1 lines (***Figure 2-7***c).

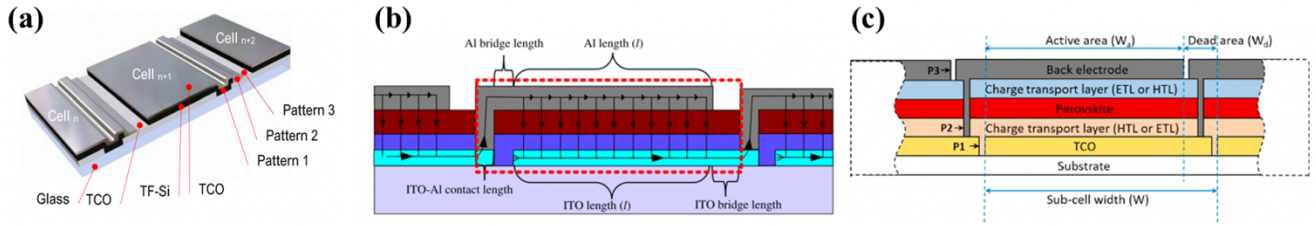

Figure 2-7. Schematic of scribe patterns.
a) *thin-film silicon cell interconnection (Booth, 2010).* ***b)*** *polymer cell interconnection* (Harald et al., 2012). ***c)*** *perovskite cell interconnection (Galagan, 2018).*

2.2.2.1 Minimodule Design

The experience in the fabrication of PSC in large-areas (***Figure 2-6***) and minimodules using the three scribe lines to interconnect the cells (Ramirez et al., 2019; Velilla et al., 2019b) indicated that an active area of approximately 2 cm^2 per sub-cell is required to reach efficiencies higher than 10% and mitigate the series resistances issues (evidenced in large-areas devices). Thus, 4 cells were determined, fixing the distance between cells to 0.7 cm

(distance between P3 lines) to reduce electrical losses (Moon et al., 2015) and the distance between P1 and P3 to 0.1 cm to limit width cell to 0.6 cm. Therefore, the maximum active area of the minimodule was limited to 9.6 cm^2 (estimated area after excluding the edge, death, and conductor areas, see ***Figure 2-8***). Here, it is remarked that P1 is the scribe line performed on the ITO layer to delimit the active area of sub-cells, which is filled with the following layers. P2 is a scribe line intended to connect the cells in series when the gold contacts the ITO. For that, this scribe must remove previous layers to clear the ITO (N_iO_x/Al_2O_3/MAPI/PCBM/Rhodamine). P3 is a scribe line performed on the gold layer to insulate the cells electrically. Finally, the designed device could be considered as minimodule following the device's definition shown in (Hu et al., 2019) because the device has 4 cells interconnected in series and an active area per cell of approximately 2 cm^2.

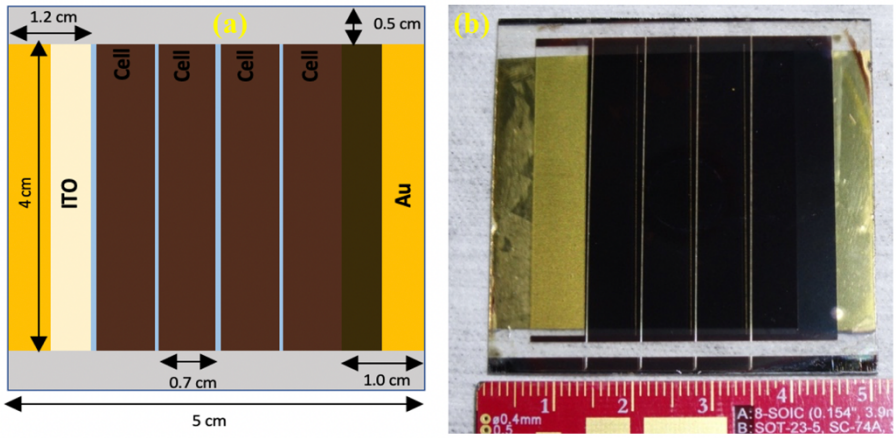

Figure 2-8. Designed and fabricated minimodule.

a) *minimodule scheme including the dimensions. The gray region corresponds to the edges in which the laser etching was performed. The blue regions correspond to the death areas in which the scribe lines must be included (P1, P2, and P3). The brown regions correspond to the active area of 4 cells. The dark brown and beige regions are intended to contact the gold (Au) and ITO, respectively. The orange regions are intended to extend the electrodes from the device with silver tape.* ***b)*** *fabricated device.*

2.2.2.2 Effect of Scribe Lines (P1, P2, and P3) on the Active Area

Figure 2-9 shows representative scribe lines on different devices. Corresponding the dark line to P1 (laser scribe on ITO), yellow line to P2 (laser scribe to remove previous layers and clear the ITO), and orange line to P3 (mechanical scribe to remove the gold and insulate the cells electrically). From these representative cases, it is observed that the death area could be different and, therefore, the active area. At this point, some aspects must be highlighted:

a) P1 and P2 are laser scribe lines, so the alignment between the substrate and equipment is visually carried out. For that, keeping similar alignment in both cases could be tricky, resulting in different gaps between P1 and P2 (***Figure 2-9***).
b) P3 is a mechanical scribe line carried out using a 3D printer adapted with a needle (***Figure 2-10***a). A G-code was written to control the printer and perform the mechanical scribe on the defined area (***Figure 2-8***a). However, the needle was located manually on the marked guides performed at the top and bottom of the device to start the scribe process (run the G-code). Hence, it is possible that the needle cannot always be over and center on the marks, resulting in distances between P1 and P3 greater than expected (1000 µm), ***Figure 2-10***c. This visual error could increase the death area, reducing the cell width from 0.6 to approximately 0.5 cm and the active area of each cell from 2.4 to 2.0 cm^2.
c) The marked guides for P3 are carried out by laser at the top and bottom of the device while the P2 scribe line is performed. So, P2 scribe lines and P3 guides are in alignment, but may not be aligned with P1, due that both scribes are performed at different times in the fabrication process. Besides, to keep the guides,

these guides on both sides are cover with a Kapton tape of 0.63 cm of width before the gold evaporation (***Figure 2-5***). So, the Kapton tape could reduce the cell length from 4 cm to 3.7 cm.

d) P3 is a mechanical scribe line. Hence, the line width may not always be the same, as is shown in ***Figure 2-9***. This effect is observed in a better way in the SEM images of ***Figure 2-10***b-c. So, the gold electrode's mechanical deformation or delamination caused by the needle (P3 scribe line) could introduce a deviation in the effective active area that is not easy to estimate. Moreover, the delamination (***Figure 2-9***b) or particles of Au could affect the cell insulation or produce short circuits between cells, effects reflected on the V_{oc}.

e) The ITO substrates of 5 x 5 cm were obtained, cutting 10 x 10 cm substrates manually. Hence, some imperfections on the borders could be difficult for the alignment to perform the scribe lines, affecting the device's active area.

f) Finally, despite drawbacks related to scribe lines (P1, P2, and P3), it is expected that these were parallel to each other to avoid short circuits and connect the cells in series. Corresponding the ideal case to P2 centered between P1 and P3. Nevertheless, if the gap between P2 and P3 is greater than the defined gap (500 µm), the probability of short circuits between cells is reduced, corresponding to the most common case obtained.

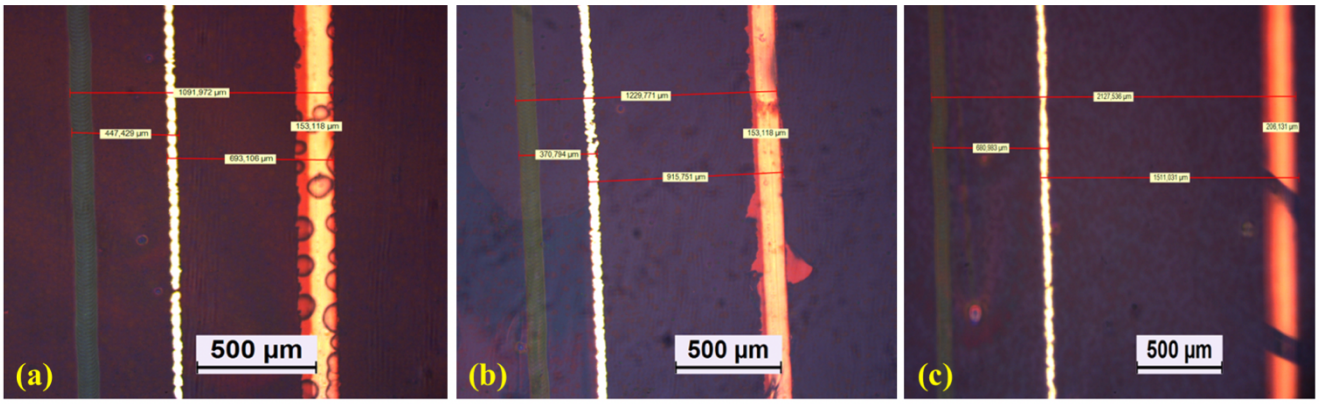

Figure 2-9. Representative scribe lines measured with an optic microscope.
In the photos, P1 lines are on the left (dark color), P2 lines are on the center (yellow color related to gold), and P3 lines are on the right (orange color).

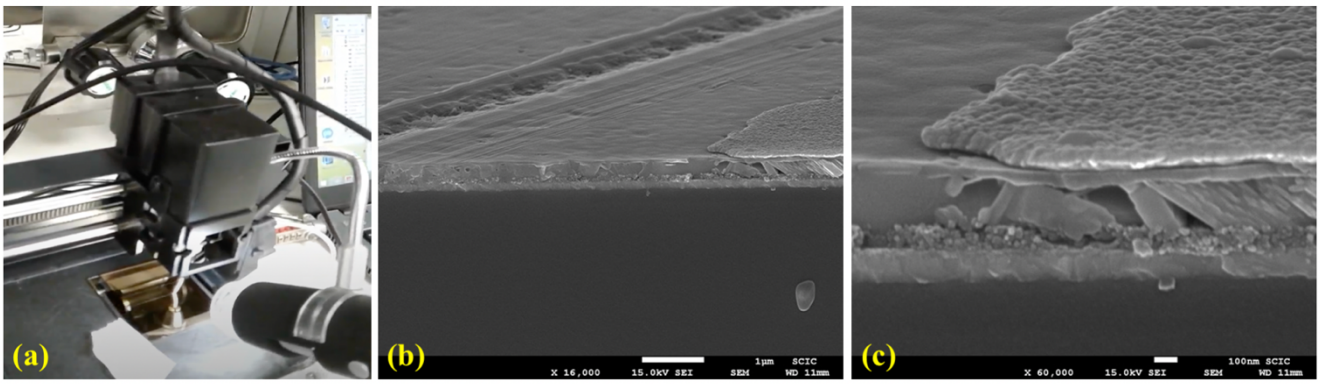

Figure 2-10. P3 scribe line.
a) *3D printed adapted with a needle and an optical microscope to perform the mechanical scribe on the gold electrode.* ***b)*** *Transversal SEM on minimodule to observe the P3 pattern on the device.* ***c)*** *zoom on the transversal SEM image.*

2.2.2.3 Minimodules Electrical Performance

Figure 2-11 shows the electrical performance of minimodules fabricated from different batches considering the inverted structure (**Figure 2-1**). The I-V curves were measured using similar conditions as were performed in solar

cells ***Figure 2-6***. Hence, from the I-V curve data, electrical performance parameters such as P_{max}, I_{sc}, V_{oc}, and FF were extracted and analyzed in the form of boxplots to illustrate the data dispersion and median values. These plots allowed highlighting some aspects.

a) In large-area cells (***Figure 2-6***a), a P_{max} of approximately 26 mW is reached with a minimodule equivalent area of 8 cm^2 (***Figure 2-11***). However, in minimodules, an average P_{max} of approximately 57 mW was reached. These results evidenced the advantage of minimodules over the large area cells.
b) Based on the results of ***Figure 2-6***c, an FF of approximately 35% for active areas of approximately 8 cm^2 is expected. However, the average FF in the minimodules was higher than 54%. This fact highlighted the advantages of interconnecting the minimodules cells instead of large-area cells, considering similar areas.
c) Considering that the minimodule has 4 cells in series and the I_{sc} corresponded to the minimal current of one of the cells (current correlated with the active area), the dispersion on I_{sc} suggested that the active area was not constant. This result allowed validation of the drawbacks mentioned before, related to different factors that affect the device's active area.
d) Considering the behavior shown in ***Figure 2-6***d related to I_{sc} as a function of the area in cells, which was fitted appropriately to second-order polynomial function ($I_{sc}(A) = -2.25A^2 + 30.93A - 17.4$), this result may be used to estimate the active area of the minimodules cell as a function of the current, ***Figure 2-11***a. Therefore, 50% of the I_{sc} data ranging between 26 and 38 mA, corresponding this current to an active area of the minimodule cell ranging between 1.6 and 2.1 cm^2. Thus, the mean I_{sc} of approximately 29 mA correlated with an active area of 1.7 cm^2.
e) Considering the efficiency commonly related to the total area, aperture area, or illuminated area (Hu et al., 2019), if the polynomial function fitted to reproduce the behavior between I_{sc} and area is used to estimate the illuminated area, the average efficiency value increase from 6.8 to 8.1%, and the maximum efficiency increase from 12.2 to approximately 15 % (***Figure 2-11***b).
f) Based on the V_{oc} results show in ***Figure 2-11***b, the data dispersion suggested a mean value of approximately 4 V for the minimodules. In this context, the V_{oc} obtained in minimodules allowed us to validate the series connection of the 4 cells because an average V_{oc} of approximately 1.01 V was obtained on large-area cells (***Figure 2-6***e).
g) Furthermore, it is well known that the ITO sheet resistance (R_{sheet}) is related to the electrical losses (Harald et al., 2012). This parameter is the main issue on large-area devices (***Figure 2-6***) and studied in the literature (Galagan et al., 2016; Li et al., 2020) that directly affect the P_{max}, *FF,* and V_{oc}.
h) The drawbacks related to the manual fabrication process can be seen in the data dispersion shown in the form of boxplots in ***Figure 2-11***. Being the data dispersion mainly due to the changes in the active area of devices, as was mentioned before (this area is not constant). Moreover, it highlights that these diagrams included all fabricated devices from different batches (history of devices). Thus, these diagrams illustrated the devices' reproducibility status and allowed visualization of the trend and operative range of variables. ***Figure 2-11***c shows representative cases of the last batch fabricated, intended to illustrate the improvement in the fabrication process based on the higher FF and V_{oc} reached, corresponding the brown I-V curve to the higher efficiency reached (12,2% considering an area of 2 cm^2 per sub-cell).
i) Finally, despite that the structure used in this work is not considered as the most efficient in the literature (Huang et al., 2019), various devices reached values in the range of efficiencies reported in the literature, this is between 10 and 17 % for minimodules with the similar area (Liu et al., 2020).

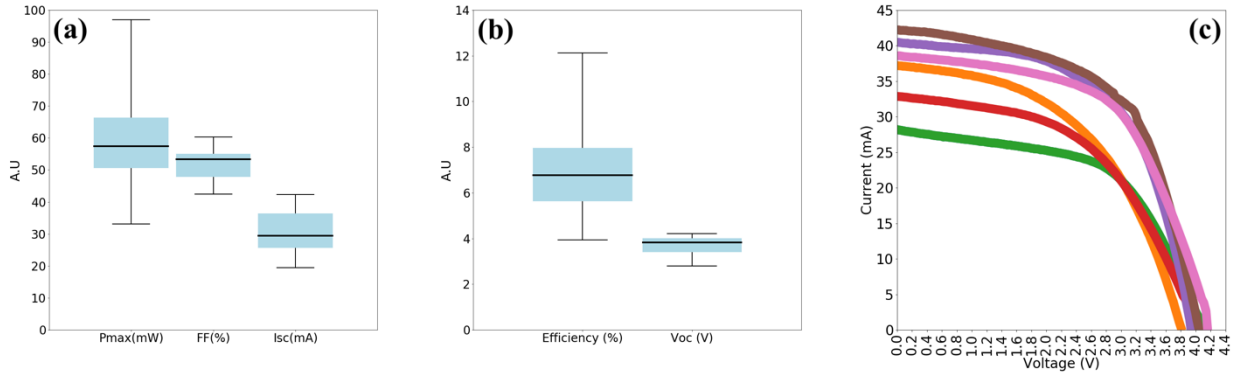

Figure 2-11. Electrical performance of minimodules fabricated.

a-b) *variables related to the electrical performance of devices are shown in the form of boxplots to illustrate the data deviation due to the evolution in the fabrication process.* ***c)*** *Representative cases from the last batch in which the higher efficiency was reached (12.2 %).*

2.1.3 Encapsulation Process

The electrode contacts were extended using silver tape (***Figure 2-12***a). Then, they were encapsulated with EVA between the device and another glass. EVA was annealed on the glass at 140 ^{0}C on a hotplate in a glovebox for 10 minutes. Then, it was put on the device and annealing at 80 ^{0}C on another hotplate for 5 minutes. Finally, the borders of devices were covered with epoxy resin (***Figure 2-12***b-c).

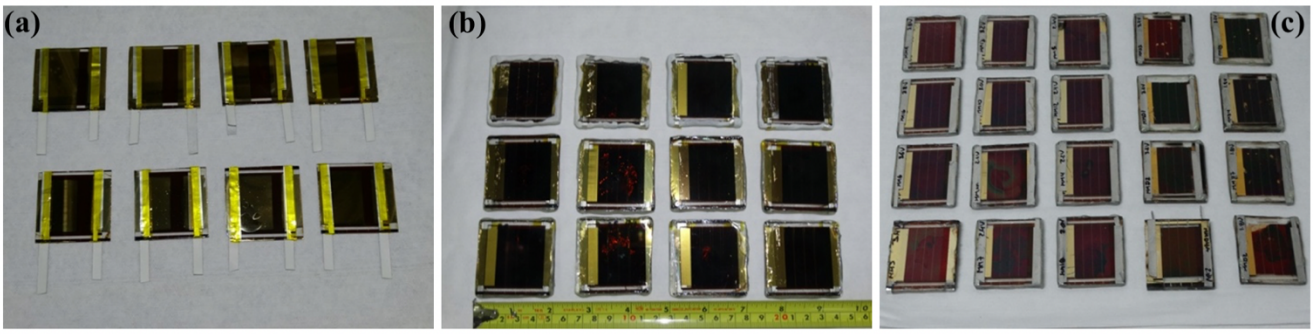

Figure 2-12. Fabricated devices.

a) *extending the contact with silver tape.* ***b)*** *encapsulated devices and covered borders with epoxy resin.* ***c)*** *representative batch.*

The selection of EVA for encapsulating the perovskite devices was due to different reasons. a) it is commonly used in the silicon solar industry (Hasan and Arif, 2014; Osterwald and McMahon, 2009; Wang et al., 2013). b) there are different accelerated tests included in International Standards for solar modules as IEC 61215 and their older version IEC 61646, intended to identify potential failures, such as break interconnects, cracked cells, delamination, dielectric breakdown, bypass diode, and corrosion (IEC 61215-1-2, 2004; IEC 61646, 2008). c) perovskite solar cells have been successfully encapsulated with EVA to withstand the temperature cycles (Cheacharoen et al., 2018). The temperature cycles test is one of the accelerated tests suggested by IEC 61215 and applied in perovskite solar cells using different encapsulating materials (Shi et al., 2017).

Consequently, the conditions to encapsulate the devices resulted from different accelerated tests carried out to evaluate the encapsulation process. For instance, ***Figure 2-13*** shows an accelerated test performed using a Xenon Test Chamber to evaluate EVA encapsulation on MAPI layers and cells exposed to light intensity (0.1 Sun) and temperature (85 ^{0}C). A significant color change was observed from these tests on the back electrode of devices

with silver as the electrode (***Figure 2-13***b). This effect correlated with the faster device's performance degradation (***Figure 2-13***c). Hence, after this, all the devices were fabricated using gold instead of silver.

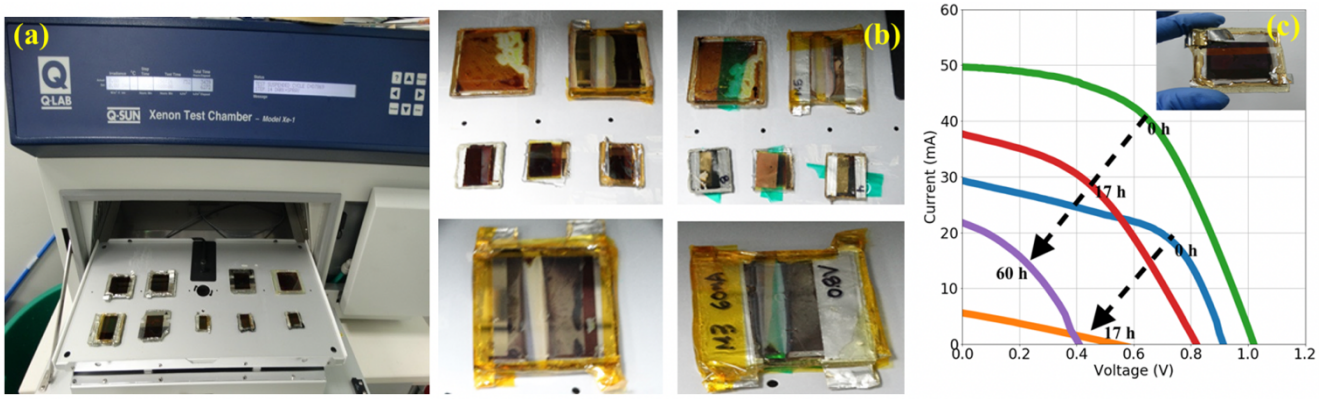

Figure 2-13. Light and temperature accelerated test.

a) *Xenon test chamber used to set the temperature at 85 ^{0}C and light intensity to 0.1 Sun.* ***b)*** *image collage to show the accelerated test's visual effect on devices after 17 h of exposure, images on the left are for the front part of devices, while the images on the right are for the back part of devices.* ***c)*** *effect on the electrical performance of the accelerated test for 60 h. Two representative cases are shown: the device with gold as the electrode and another for the device with silver as the electrode.*

The EVA encapsulation process required annealing the devices at 140 ^{0}C and extract the air to avoid the air bubbles (with vacuum during the process). To mitigate the effect of the temperature on the MAPI devices, the annealing process was divided into two parts. The first, in which the EVA over a clean glass is annealing at 140 ^{0}C in a hotplate for 10 minutes. The second, in which the perovskite devices (layers on ITO) are put on the EVA and annealing at 80 ^{0}C in another hotplate for 5 minutes. Finally, the borders of devices are sealed with an epoxy resin.

To evaluate the moisture withstands of encapsulating devices, these are exposed to 100 % of humidity, ***Figure 2-14***a. ***Figure 2-14***b shows encapsulated devices evaluated for 5 days using two different epoxy resins. According to the manufacturer, the transparent Epoxy Quick resin by Loctite is suitable for temperatures lower than 100 ^{0}C, while the white Epoxy Bonder resin by Loctite is suitable for temperatures lower than 200 ^{0}C. From different tests, the transparent resin better withstands the humidity test because the white resin in only two days showed visual degradation (***Figure 2-14***b), which can be observed in a better way under a microscope (***Figure 2-14***d-f). After 5 days of exposure, a complete degradation was observed (***Figure 2-14***c). Devices sealed with a transparent Epoxy Quick Set resin by Loctite did not show visual degradation effects during the exposure, even under a microscope. Hence, the transparent resin was selected to seal the devices.

To validate the batch encapsulation process, a 100% humidity test is performed on randomly selected samples for one day, ***Figure 2-15***. The batch passes the test if the performance of the tested devices does not show significant changes. Then, the devices belong to this batch are suitable for other tests (such as outdoor conditions). ***Figure 2-15***b shows the I-V curves of three devices belonging to the same batch. Here, the batch's encapsulation process is successful because no significant changes were observed in the performance (black marks on the figure).

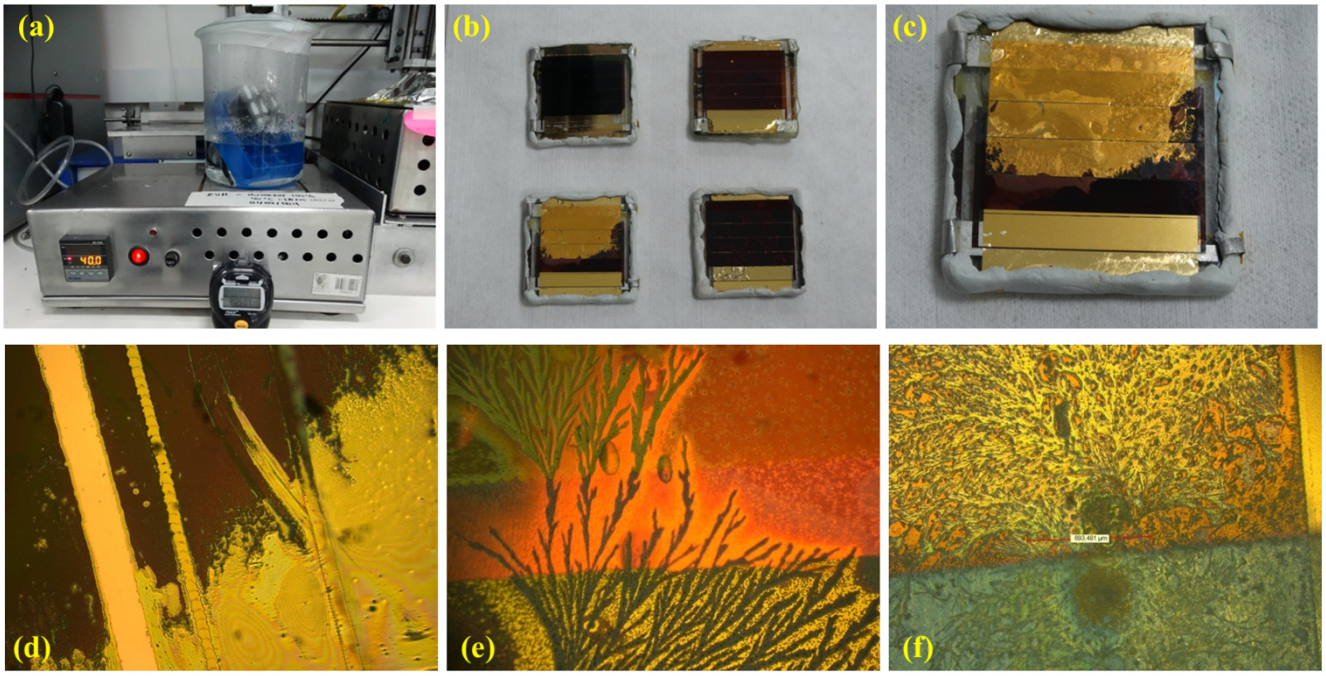

Figure 2-14. Humidity Accelerate test.

a) *experimental setup, corresponding to a sealed glass container with deionized water and devices. The glass container is put on a hotplate at 40 ^{0}C. The devices are placed on a rubber container to avoid direct contact with water.* ***b)*** *devices sealed with different epoxy resins after 2 days of exposure.* ***c)*** *failure of encapsulation that allowed the humidity ingress of device tested, photo corresponding to 2 days of exposure.* ***d-f)*** *microscope images related to samples showed in* ***Figure 2-14****b-c with visual degradation. The paths or marks shown in these images correlated with the ingress of moisture or humidity.*

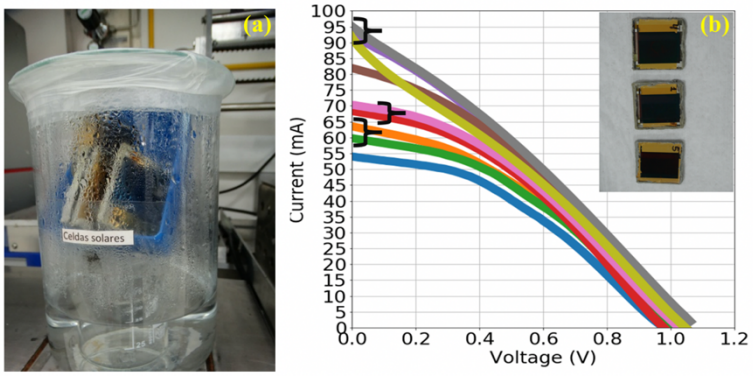

Figure 2-15. Testing the encapsulated process.

a) *samples randomly selected and exposed at 100 % of humidity for 1 day.* ***b)*** *Changes in the electrical performance after the test. Corresponding the blue, orange, and green lines to device 1 (blue to the unencapsulated device, orange to the encapsulated device, and green after the test). Pink and red lines to device 4 (pink to the encapsulated device, and red after the test). Brown, gray, and yellow lines to device 5 (brown to the unencapsulated device, gray to the encapsulated device, and yellow after the test). The black marks are visual guides to illustrate the deviation in the performance between encapsulated and exposed device.*

2.2 Device Characterization

Conventionally, the performance of photovoltaic devices is characterized by the I-V curve considering the ambient/device temperature and illumination conditions, such as the Standard Test Conditions (1000 W/m^2 and

25 ^{0}C of cell temperature). From this curve, main variables such as V_{oc}, I_{sc}, and P_{max} are extracted to define the electrical performance. However, due that the ideality factor (n_{ID}) is the most reported parameter for different solar cell technologies based on their relationship with conduction, transport, recombination process, and interface junctions, here this parameter is calculated to improve the device characterization. Therefore, different methodologies to estimate this parameter were implemented, including the impedance frequency response and the relationship between V_{oc} and irradiance (Almora et al., 2018; Yoo et al., 2021, 2020).

2.2.1 Impedance Frequency Response (IFR)

Impedance Frequency Response (IFR) is a non-invasive nor destructive technique widely used in different modeling applications within power systems, high-speed interconnects, electronic packages, and microwave systems (Gustavsen and Semlyen, 1999). Briefly, in solar cells, it has been used to characterize electrical properties of materials and their interfaces (Barsoukov and Macdonald, 2005), to characterize the corrosion-induced degradation and life prediction of organic coatings on metals (Kendig and Scully, 1990), to observe degradation effects in Dye-Sensitized Solar Cell (Wang and Gra, 2005), to identify the photovoltaic behavior related to transport and recombination mechanism and to compare different architectures of perovskite solar cells (Gonzalez-Pedro et al., 2014), to study the surface recombination on perovskite devices (Zarazua et al., 2016), to observe insights related to degradation of perovskite solar cells because the moisture ingress (Ma et al., 2017), to show the link between Dye-Sensitized and perovskite solar cells (Yoo et al., 2019), to classify new nanoscale perovskite-sensitized solar cell (Yoo et al., 2020), to model the drift-diffusion on perovskite solar cells (Riquelme et al., 2020), among others. All these applications have been possible because the IFR scans the impedance of devices, changing the frequency of input sinusoidal wave and measure the output signal in a broad range of frequencies (typically between 100m Hz and 1 MHz). This result is considered as a fingerprint of devices, which is a function of the operative condition such as bias and light intensities conditions (Pitarch-Tena et al., 2018).

Considering that the impedance is a complex term formed by resistance (real part) and admittance (imaginary part), the impedance is displayed in the form of complex diagrams such as Nyquist, Bode, or capacitance-frequency, ***Figure 2-16***. In the Nyquist diagram, the x-axis corresponds to the resistance, and the y-axis corresponds to admittance. In this context, the impedance behavior is characterized by semi-arcs representing different dynamic characteristics (physical processes), corresponding to the high-frequency response to the data close to the y-axis and the low-frequency response to the data far from the y-axis. In the Bode diagram, the magnitude and phase are plotted as a function of frequency, allowing observation of the main impedance features in the analyzed frequency spectrum. Here, because both patterns are observed simultaneously, it is possible to observe a better correlation with electrical elements such as an inductor, capacitor, and resistance (Gustavsen and Semlyen, 1999). Finally, the capacitance-frequency diagrams show different capacitive processes and features in the analyzed frequency spectrum (Guerrero et al., 2016a). This last diagram commonly shows three patterns or plateaus that correlate with separated polarization processes depending on the frequency range. For instance, the low-frequency region (frequencies close to 0 Hz) correlates with electronic/ionic accumulation at electrode interfaces (oxide properties). The intermediate-frequency region (frequencies close to 1000 Hz) correlates with photogenerated carriers and surface recombination, and the high-frequency region (frequencies close to 1 MHz) correlates with the geometric capacitance and bulk of the device.

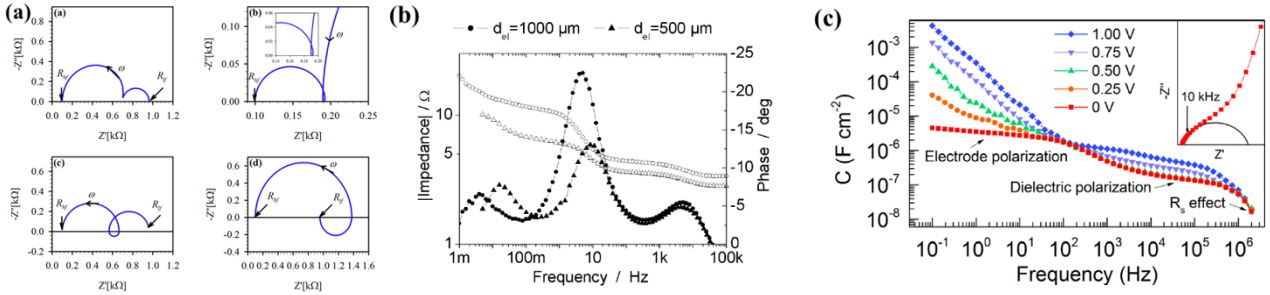

Figure 2-16. Diagrams used in literature to represent the Impedance frequency response.
a) *Nyquist diagram to illustrate the semi-arcs related to different kinetic relaxation constant (Ghahremanirad et al., 2017).* ***b)*** *Bode diagram to illustrate the effect of changing the TiO_2-layer thickness on the impedance of dye solar cells (Kern et al., 2002).* ***c)*** *Capacitance-frequency diagram for MAPI solar cell under different applied bias and dark conditions (Almora et al., 2016).*

2.2.1.1 IFR of Fabricated Devices

To characterize the impedance patterns for the fabricated devices, nine devices were analyzed: 3 without electron transport layers (ETL free, without Rhodamine and PCBM) and an active area of approximately 4 cm^2, 3 cells, and an active area between 2 and 3.6 cm^2, and finally 3 minimodules of 4 cells interconnected in series and an active area of approximately 8 cm^2. These were analyzed under dark and one sun conditions considering open-circuit conditions following the experimental setup shown in ***Figure 2-17***. Hence, a LED light system by Newport and potentiostat by Autolab PGSTAT-30 were used. Subsequently, the bias of a potentiostat was set to $V_{oc.}$ In this operative point, the IFR response analysis was performed in the range of 100 mHz and 1 MHz, using an AC signal of 10 mV in amplitude and scanning first from high to low frequency (down) and then from low to high frequency (up) to ensure the reliability of the measurement while avoiding parasitic effects.

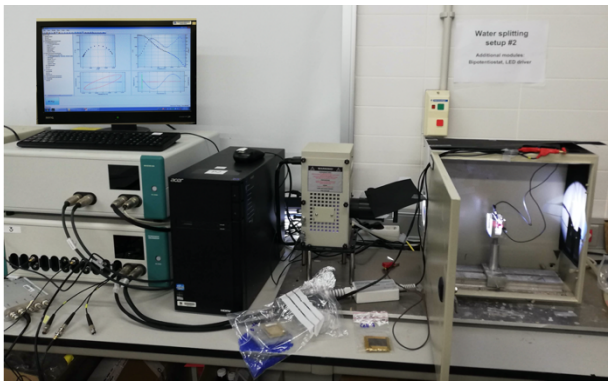

Figure 2-17. Impedance frequency response experimental setup.
To record the impedance, a potentiostat by Autolab PGSTAT-30 was used. To change the light conditions, a LED light system by Newport was used.

The IFR results are shown in the form of Nyquist diagrams (***Figure 2-18***) and Bode diagrams (***Figure 2-19***). From these results, it is possible to characterize the impedance of devices, for instance:

a) In a general way, Nyquist diagrams show two semi-arcs as it is conventionally observed for other solar cells.
b) Considering that both conditions showed different magnitude orders (Ω for light and kΩ for dark), the Bode diagram allows us to visualize in a better way both results at the same time to correlate some features with the frequency. In this way, cells and minimodules show similar behavior to the low pass filter, which is mainly characterized by two cut-off frequencies at which the impedance shows a "knee curve" defining a transition of the impedance by the two straight-line regions. Under dark conditions, one at approximately 10 Hz for cells and 100 Hz for minimodules, another at 100 kHz for cells, and 500 kHz for minimodules. Under light conditions, one at 50 kHz for cells and 100 kHz for minimodules, another at 200 kHz for cells,

and 1 MHz for minimodules. These cut-off frequencies define three regions. 1) Low-frequency region, in which the impedance is constant. 2) Intermediate region, in which the impedance decreases as the frequency increases. 3) High-frequency region, in which the impedance increases as the frequency increases.

c) In the ETL-free devices, the impendence patterns show four cut-off frequencies under dark conditions, approximately at 0 Hz, 10 Hz, 100 kHz, and 100 kHz. Nevertheless, under light conditions, the impedance patterns show similar behavior to other devices. These results allowed us to evidence the function of the ETL layer in the complete device, which changes the impedance pattern to get closer to the pattern behavior of the low pass filter, allowing the electrons collection and the electron direction as it can be seen in the Nyquist plots under illumination conditions test (***Figure 2-18***d-f). Besides, the ETL layer reduces the resistance at high frequencies (***Figure 2-19***a-c) and increases the impedance at low frequencies. This fact could be attributed to the capacitive effect of introducing the ETL to complete the device, which is reflected in the impedance angle behavior that tends to -90^0 (***Figure 2-19***d-e).

d) Based on the impedance phase, it is possible to observe well-defined peaks at approximately 100 kHz (high frequencies) under light conditions. Under dark conditions, two peaks appear in a short bandwidth at the intermedia frequencies for cells and minimodules. For devices without ETL, the peaks appear at 10 Hz and 10 kHz, respectively. These facts suggest that the first peak could be correlated with the interaction between the perovskite and the mesoporous layer. To confirm this, ***Figure 2-20*** shows the impedance pattern for different devices in ITO substrate of 2.5x2.5 cm. One related the perovskite layer between gold contacts (Caram et al., 2020), another related to mesoporous layer ($NiOx/Al_2O_3$) between ITO and Cu tape as contacts, and other related to planar device (*ITO/NiOx/MAPI/Au*). From these impedances, it is possible to observe that none of these devices shows a phase peak a low frequency as it was observed in the incomplete cell (without ETL) in ***Figure 2-19***c. In contrast, the perovskite layer between electron contacts shows an ideal capacitive behavior, acting as the low pass filter, reaching the maximum phase value of -90^0 at approximately 30 kHz. It suggests that the phase peak at low frequency could be correlated with the interaction between perovskite and the mesoporous layer as it was observed in dye solar cells according to the T_iO_2-layer thickness (Kern et al., 2002). Hence, this interaction is improved when the electron layer is included, as was mentioned in (Ramirez et al., 2018a).

e) Relating to the capacitance results, when complete devices are considered (cells and minimodules), it is observed that for frequencies lower than 10 kHz, the capacitance changes according to light intensities. For frequencies between 10 kHz and 100 kHz, the capacitance is almost constant, but at a higher frequency, the capacitance shows a decreasing trend.

f) Finally, based on these results, it is possible to see the advantages of connecting cells in series over the large area cells (monolithic). On the one hand, based on the parameters extracted from the I-V curve, the electrical losses reduction allowed the increase of FF and efficiency, as it was shown in ***Figure 2-11***, on the other hand, based on the IFR, a significant reduction of minimodules capacitance versus the cell capacitances, allowed improving the impedance over the frequency range evaluated (insulation), fact that it is evidenced in the impedance phase which tends to -90^0, pointing to a more capacitive effect (***Figure 2-19***g-i).

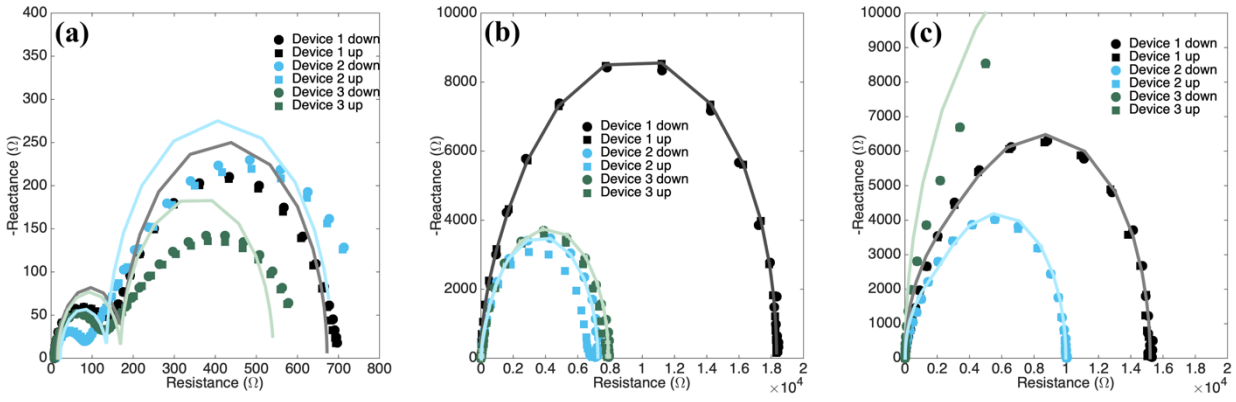

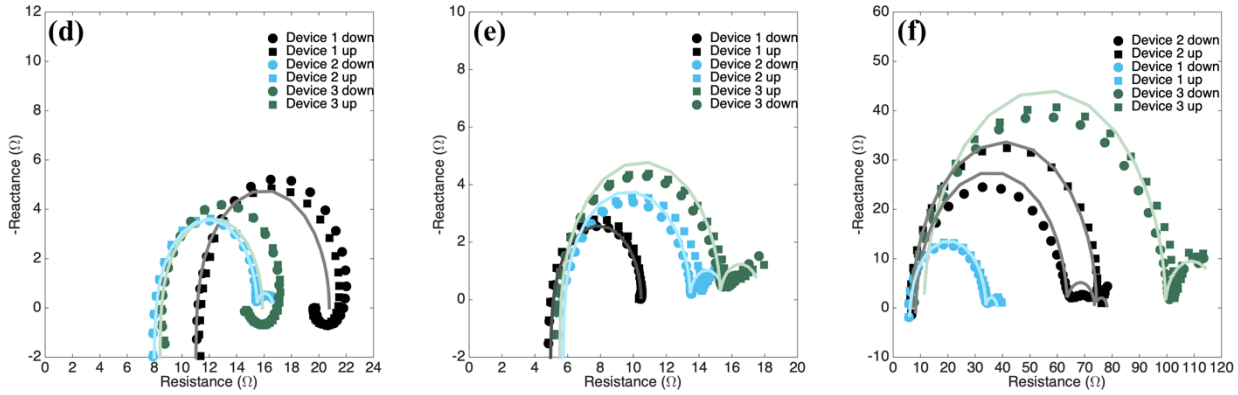

***Figure 2-18**. **Nyquist diagrams of the impedance frequency response of encapsulated devices**. **a-c)** Nyquist diagrams of impedance under dark conditions. **d-f)** Nyquist diagrams of impedance under 1 sun of light condition. Corresponding **a)** and **d)** to electron transport layer free (ITO/Ni_iO_x/Al_2O_3/MAPI/Au), **b)** and **e)** to complete cells, and **c)** and **e)** to complete minimodules. Markers are related to experimental data measured from high to low frequency (down), and from low to high frequency (up). The solid lines are related to data fit using the equivalent circuit shown in **Figure 2-21**.*

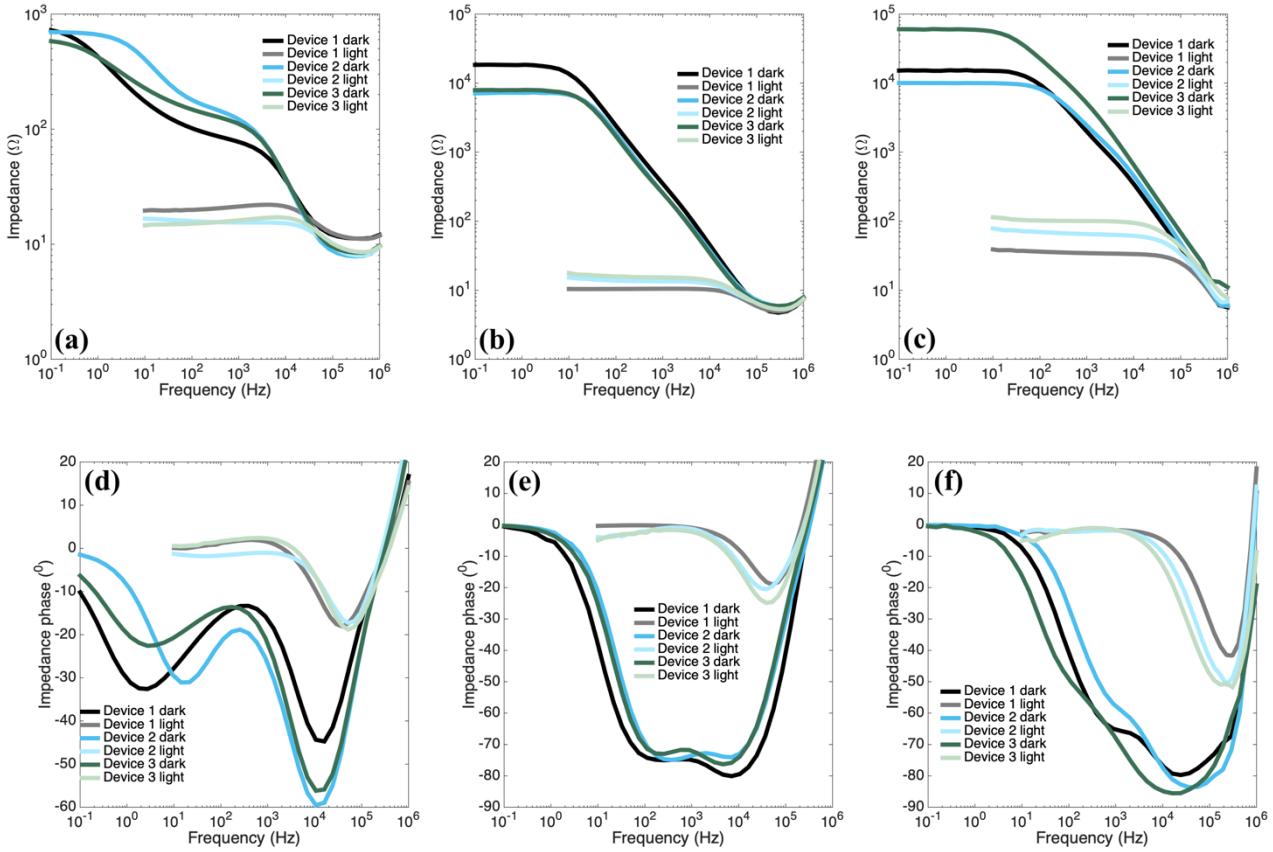

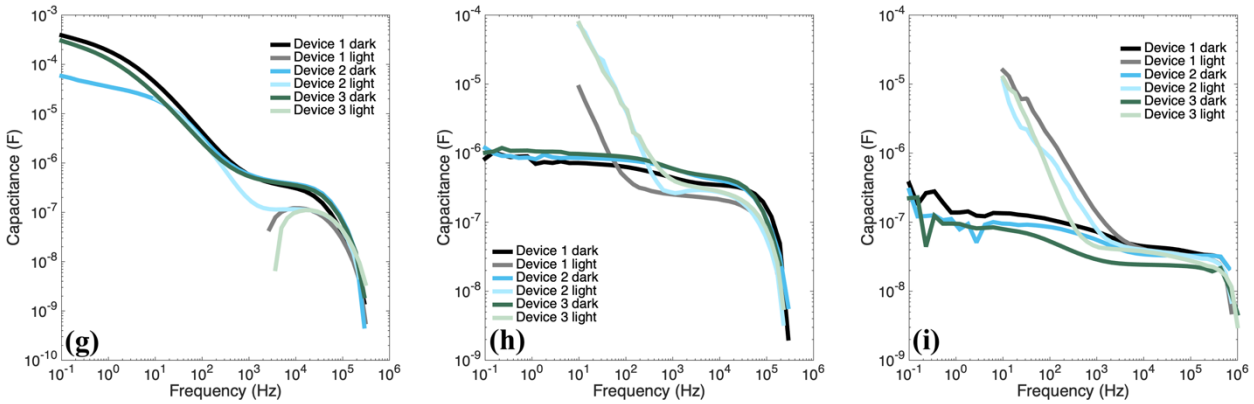

Figure 2-19. Bode diagrams of the impedance frequency response of encapsulated devices.
a-c) *impedance magnitude as a function of frequency.* ***d-f)*** *impedance angle as a function of frequency.* ***g-i)*** *capacitance as a function of frequency. Corresponding* ***a), d),*** *and* ***g)*** *to electron-free layers (ITO/Ni_Ox/Al_2O_3/MAPI/Au),* ***b), e,)*** *and* ***h)*** *to cells, and* ***c), e),*** *and* ***i)*** *to minimodules.*

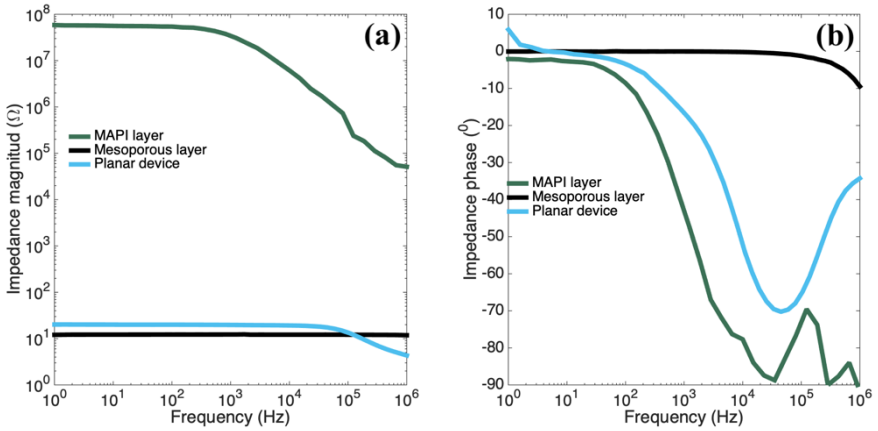

Figure 2-20. The impedance frequency response of the unencapsulated devices.
Corresponding ***a)*** *to the impedance magnitude and* ***b)*** *to the impedance phase. MAPI layer corresponds to the MAPI layer deposited on the glass between the gold layer (Caram et al., 2020). The mesoporous layer corresponds to NiOx and Al_2O_3 layer deposited on the ITO substrate, and the planar device corresponds to Ni_Ox/MAPI/Au layers deposited on the ITO substrate. The IFRs were performed under dark conditions.*

2.2.1.2 Equivalent Circuit to Represent the IFR

It is worth noting that different equivalent circuits have been used to reproduce the impedance spectra in the literature. Nevertheless, the equivalent circuits showed in ***Figure 2-21*** allowing reproduction of both arcs observed in the impedance spectra, and it is a simple circuit, allowing a better interpretation of the extracted parameters. Therefore, to complete the IFR characterization, impedances were fitting to this equivalent circuit model used in previous work to reproduce the impedance features (Yoo et al., 2020). Corresponding the series inductance (L_s) to electrical wires, series resistance (R_s) to wires and cell contacts, recombination resistance (R_{rec}) to resistance between electrical contacts of the device, geometric capacitance (C_g) to capacitance between electrical contacts of the device. Thus, R_{rec} and C_g are intended to reproduce the main features of impedance spectrum related to the low pass filter behavior, and other elements such as R_d and C_d are intended to produce some specific features of the spectrum and correlated with the second arc.

For impedance fitting, a global optimization process involving a genetic algorithm (GA) and the simplex method was implemented to minimize the square error between the measured impedance (Z) and the calculated impedance

using the equivalent circuit (Z_{model}) at the frequencies considered (f), considering all samples recorded (NS), **Equation 1**, in accordance with the methodology reported in previous work (Velilla et al., 2018). Therefore, the main parameters of the genetic algorithm considered to perform the optimization process were a randomly initialized population with a size of 200, tournament selection, a two-point crossover function, uniform mutation, and 600 generations as the stopping criterion. Once the GA finds the solution, it is used as the initial condition in the Simplex method to improve the error.

$$Equation\ 1.\ Error = \sqrt{\sum_{k=1}^{NS}\left(Z(f(k)) - Z_{model}(R_s, L_s, R_d, C_d, C_{g,} R_{rec}, f(k))\right)^2}$$

Figure 2-21 shows the parameters of one representative sample of each device analyzed in ***Figure 2-18*** and ***Figure 2-19***. In this scheme, C_g shows similar values to those obtained at dark conditions in a wide frequency range (***Figure 2-19***g-i), being this value almost constant under dark and light conditions, defining the electrical insulation of devices, it means the capacitance between electrical contacts including the perovskite capacitance and other interlayers. In addition, this parameter is approximately equal for the cell and the ETL free device, suggesting that this capacitance is mainly related to perovskite layer (bulk) or geometrical capacitance. In the case of minimodule, because four series cells are connected, this circuit could be approached as the connection of four circuits in series, resulting in four series capacitances. For that, the equivalent capacitance is lower, as it was observed in ***Figure 2-21***c. Other parameters are sensible on light, pointing that these parameters are mainly related to the photoconversion processes or are affected by the current flow in the device. For instance, the R_{rec} values in light conditions are lower than in the dark, suggesting a lower recombination process under light conditions. Finally, the values of the extracted parameters can be used as initial conditions to track the device evolution over time, intended to identify or correlate the changes on the parameters with physical elements of the device.

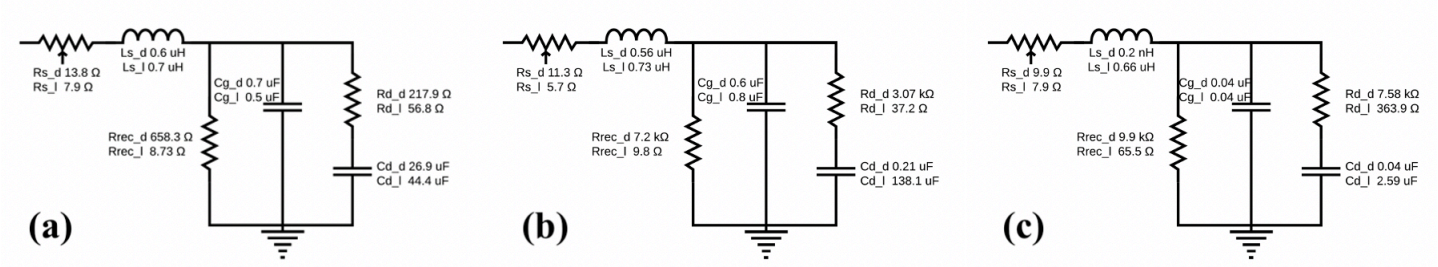

Figure 2-21. Equivalent circuits to represent the IFR of devices.
*Extracted parameter for **a)** ETL free, **b)** cell, and **c)** minimodule. Corresponding the subscript "d" to dark conditions and "l" to light conditions.*

2.2.2 Ideality Factor (n_{ID})

The ideality factor also called the quality factor or shape curve factor, is the most reported parameter for different solar cell technologies. This parameter has been used to define the electrical behavior of solar devices due to its relationship with conduction, transport, recombination, and behavior at interface junctions, providing direct information on the dominating recombination processes. Therefore, in silicon, n_{ID} has been widely studied and estimated in various ways, such as using the relationship between the open-circuit voltage (V_{oc}) and light intensity to overcome the effects of series resistance (Kerr and Cuevas, 2004), performing numerical calculations (Santakrus Singh et al., 2009), and extracting this parameter from I-V curves at different light intensities and temperatures using equivalent circuit models (Bashahu and Nkundabakura, 2007). For perovskite, although there are relatively few reports related to this parameter, Tress and coworkers have reported a full interpretation of n_{ID} for nonencapsulated cells, establishing the relationship between the dominating recombination process, the light intensity and V_{oc} (Tress et al., 2018). Besides, n_{ID} has been estimated through impedance/frequency-response (IFR) analysis (Almora et al., 2018; Contreras-Bernal et al., 2019; Yoo et al., 2020), from the I-V curve at standard test

conditions using a one-diode model (Velilla et al., 2018), and from the dark I-V curve through numerical simulation considering the continuity and Poisson's equations (Agarwal et al., 2014). Moreover, an agreement has been shown between the n_{ID} value estimated from the recombination resistance extracted through IFR analysis and the value calculated from V_{oc} at different light intensities (Almora et al., 2018; Yoo et al., 2020).

In the case of silicon solar cells, n_{ID} values are between 1 and 2. Close to 1 indicates ideal junctions, while equal to 2 would be related to degradation of the solar cell, non-uniformities on recombination centers, and shunt resistance effects (Jain and Kapoor, 2005). In dye-sensitized solar cells, n_{ID} values are between 2 and 3 (Murayama and Mori, 2006). In organic-solar cells, n_{ID} values are higher than 2 (Chegaar et al., 2006). In perovskite solar cells, ideality factors close to 2 have been reported due to carrier recombination and trap-assisted recombination under dark conditions (Agarwal et al., 2014; Wetzelaer et al., 2015). When several hole transport layer thicknesses are considered under dark conditions, the ideality factor ranging between 1.3 and 2.5 has been found (Marinova et al., 2015). However, due to the estimation of this parameter could be affected by different aspects such as hysteresis, slow relaxation processes, the open-circuit voltage dependence of light intensity and temperature, capacitive effects, and parasitic resistances, among others, the perovskite ideality factor estimated from the dark I-V curve could be higher than 2 (Almora et al., 2018).

2.2.2.1 Estimated n_{ID} from the I-V curve

Commonly this parameter is estimated fitting the I-V curve to circuital models based on Kirchhoff's current law as the one-diode model. This model is characterized to be implicit, nonlinear, and multivariable, **Equation 2.** Therefore, there is no way to calculate an exact solution from the I-V data. Hence, up to 34 methods have been proposed in the literature to extract or estimate the five parameters related to the model (Bashahu and Nkundabakura, 2007; Cotfas et al., 2013). The shunt resistance (R_{sh}) is related to the leakage current across the surfaces involving pin-holes, grain boundaries, and charge recombination processes (Mialhe et al., 1986). The series resistance (R_s) is reflected in the voltage drops and is related to the conductivity of the layers and interphases; this parameter is affected by space charges, traps, or other barriers (Li et al., 2013). Virtually, a proportional relationship between the photo-generated current (I_{ph}) and irradiance intensity is observed. The diode saturation current (I_o) is related to the material properties, junction configuration, recombination processes, and temperature. Thermal voltage (V_T) depends on the temperature (T), the Boltzmann constant (k), and electron charge (q), **Equation 3.** Finally, the ideality factor (n_{ID}) is related to the Shockley theory involving conduction, interfacial layers, transport, and recombination processes in the bulk and surface regions, directly affecting the shunt resistance and the open-circuit voltage (Khan et al., 2013).

$$\textit{Equation 2. } I = I_{ph} - I_0\left(e^{\left(\frac{V+I\cdot R_S}{n_{ID}\cdot V_T}\right)} - 1\right) - \frac{V+I\cdot R_S}{R_{sh}}$$

$$\textit{Equation 3. } V_T = k * T/q$$

However, since the estimation of the parameters of this model depends on different physical aspects (such as temperature, light condition, number of series cells, among others), mathematical assumptions to simplify or transform the problem, and the numerical method, which can be initial value-dependent (Bashahu and Nkundabakura, 2007) or instable in the results (Ishibashi et al., 2008), it is possible to obtain large relatively-errors in the optimization process due to unrealistic parameters, such as negative resistances (Chan et al., 1986) or higher diode ideality factors (Araki and Yamaguchi, 2003). This instability in the estimated parameters has been observed under measurement uncertainty when data noise or fewer points of the I-V curve are considered (Caracciolo et al., 2012). These facts remark the complexity that is involved in estimating reliable parameters from the I-V curve.

Standard classification of methods to extract the parameters is exact and numerical methods. Some methods are called exact because these parameters are expressed explicitly from algebraic manipulation. To obtain an analytical

expression for the involved parameters, the most exact methods evaluate the one-diode model equation and its derivative at specific points of the I-V curve, such as (V_{oc}, 0), (0, I_{sc}), and (V_{mpp}, I_{mpp}). Moreover, to extract the parameters, some assumptions have been incorporated to simplify the iterative process or reduce the number of variables to be estimated (Bai et al., 2014; Cubas et al., 2014; de Blas et al., 2002; Khan et al., 2013; Phang et al., 1984; Toledo and Blanes, 2016). Other methods are called numerical because they evaluate the one-diode equation and its derivate in different points of the I-V curve, obtaining a set of nonlinear equations that can be solved using the Newton-Raphson method (Hasan et al., 2016; Karatepe et al., 2006), iterative processes (Carrero et al., 2011), among others. Additionally, when the numerical methods used to estimate the parameters required to calculate the slope numerically at V_{oc} and/or the slope at I_{sc} as the initial conditions, instability and non-convergence of the solution can appear. Moreover, some of these methods can be sensitive to the initial conditions (Ishibashi et al., 2008). To figure out these problems, numerical methods that are related to artificial intelligence, such as particular swarm (Boutana et al., 2017), Genetic Algorithm (GA), has been successfully used to extract the five parameters of the one-diode model (Mellit and Kalogirou, 2008; Zagrouba et al., 2010). In these cases, one common way to express the parameter estimation as an optimization problem is minimizing the mean square error (MSE) **Equation 4,** which related the current measured (i_{exp}) and the current calculated evaluating the Equation 2, where the samples corresponding to the number of points that are considered in the I-V curve.

$$Equation\ 4.\ MSE = \frac{1}{samples}\sum_{k=1}^{samples}\left(i_{exp}(k) - i\left(\left(I_{ph}, I_o, n_{ID}, R_{sh}, R_s\right), k\right)\right)^2$$

In order to illustrate common problems related to the fitting process of I-V to one-diode model, ***Figure 2-22*** shows a sensitivity analysis of the estimated parameters for solar cells of different efficiencies (ranging between 4.6 and 12 %) and an active area of approximately 1 cm^2 (Velilla et al., 2018). From this analysis, it is easy to see why numerical methods that search for local solutions could be trapped in a specific region and why methods, such as GA, which explore global solutions could perform better. Additionally, these kinds of plots show that the estimation of the one-diode model parameters from the I-V curve is susceptible to minor differences in the involved parameters. Hence, different parameter combinations lead to MSE reduction even by solutions lacking physical meaning as negative resistances, being these feasible and local solutions, but not global and realistic solutions. However, MSE lower than 1×10^{-9} could be considered as an excellent metric to evaluate the fitting performance and determine meaningful and reliable parameters. Thus, solutions with lower MSE could be considered as a global minimum. In this sense, **Table 2-1** shows the estimated parameters related to the minimal MSE of the evaluated cells. Corresponding the lower ideality factor to the device with higher efficiency. Devices with n_{ID} in the expected range discussed in the literature (between 1 and 2) are characterized by an average series resistance of approximately 10 Ω, average shunt resistances higher than 800 Ω, Fill Factor higher than 0.5, and V_{oc} close to 1 V. Other cases related to n_{ID} higher than 2.9 correlated with lower efficiencies and FFs. This result is congruent with a defective cell or high losses effect because variables such as R_{sh}, I_o, and n_{ID} are reflected in the recombination processes.

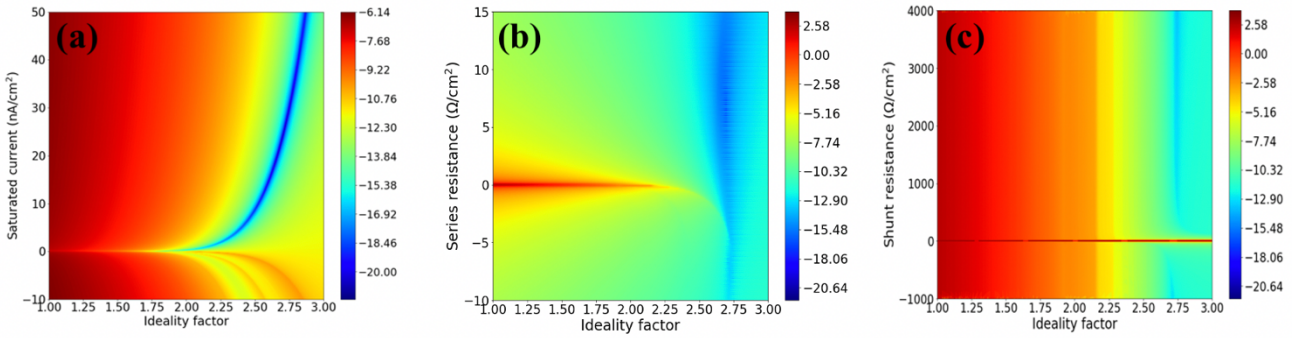

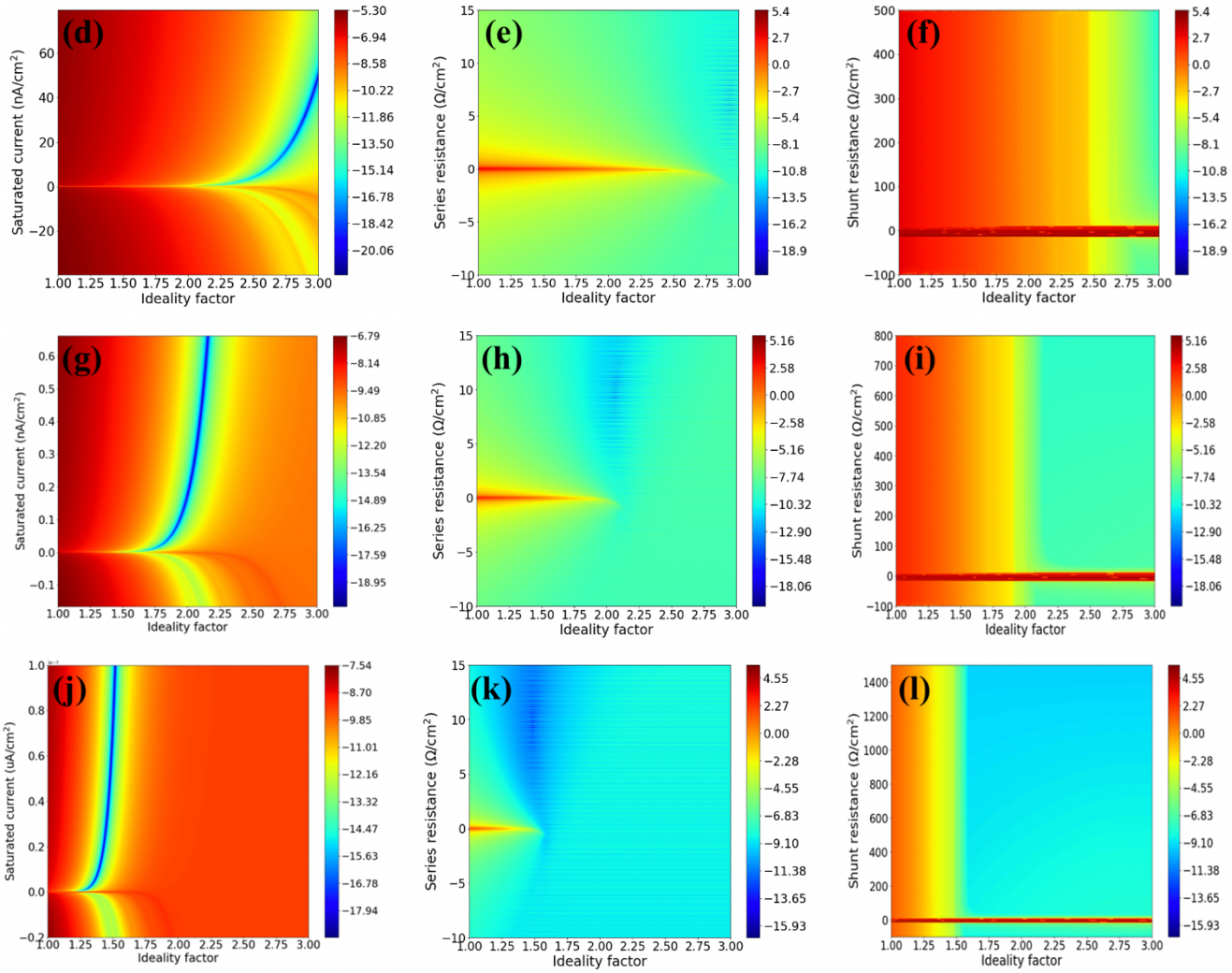

Figure 2-22. Sensitivity analysis of extracted parameters of one diode model.
Corresponding to ***a-c)*** *to the cell 1 with an efficiency of 4.6%.* ***d-f)*** *to the cell 5 with an efficiency of 9.3%.* ***g-i)*** *to the cell 8 with an efficiency of 10.4 %.* ***j-l)*** *to the cell 11 with an efficiency of 12%. The color bar shows the estimated error in the logarithmic scale using* ***Equation 4.***

Table 2-1. *Electrical performance and estimated parameters of the one diode model for solar cells. The solutions corresponded to the procedure mixing GA with the Simplex method to minimize the MSE between the data and model* (Velilla et al., 2018).

Cell	*n* (%)	FF	V_{oc} (V)	J (mA/cm²)	MSE 10^{-10}	I_{ph} (mA/cm²)	I_o (nA)	n_{ID}	R_s (Ω·cm²)	R_{sh} (Ω·cm²)
1	4.67	0.67	0.88	7.89	4.80	7.90	0.023	2.70	6.44	3392.12
2	4.68	0.32	0.78	18.38	7.21	18.51	12,943.355	5.01	0.46	59.02
3	4.62	0.34	0.79	17.04	7.83	17.16	3088.873	4.10	0.20	67.63
4	5.02	0.33	0.85	17.86	1.10	17.93	1401.235	4.06	0.20	64.98
5	9.35	0.59	0.97	16.31	4.20	16.58	39.718	2.95	5.51	352.36
6	9.41	0.64	0.99	14.81	3.97	15.06	0.002	1.70	11.32	828.66
7	9.81	0.63	0.99	15.51	1.18	15.66	0.238	2.15	9.98	1195.98

Cell	n (%)	FF	V_{oc} (V)	J (mA/cm²)	MSE 10^{-10}	I_{ph} (mA/cm²)	I_o (nA)	n_{ID}	R_s (Ω·cm²)	R_{sh} (Ω·cm²)
8	10.45	0.65	1.02	15.72	9.91	15.85	0.240	2.22	9.66	1491.74
9	10.68	0.59	0.95	18.87	1.78	19.1	0.331	2.07	9.65	586.06
10	10.95	0.67	1.01	16.22	2.06	16.26	3.976×10^{-3}	1.78	9.98	3951.71
11	12.18	0.67	1.01	17.98	5.19	18.05	5.993×10^{-5}	1.48	9.75	3184.29

2.2.2.2 Estimated n_{ID} from the Relationship Between V_{oc} and Light Intensity

Because the n_{ID} can be accurately estimated from the I-V curve using proper optimization methods, this procedure could be considered as successful if the I-V curves are well defined. In cases in which the I-V curves show an S-shape, this procedure could not be suitable, and other elements in the equivalent circuit such as another diode have been included to reproduce the I-V behavior, increasing the complexity and accurate interpretation of ideality factor (Bashahu and Nkundabakura, 2007; Cotfas et al., 2013). The S-shape behavior is associated with the chemical degradation of electrical contacts or charge accumulation on electrodes affecting the series resistance of the device (Guerrero et al., 2016b). In this sense, to avoid the series resistances issues, another method is used to estimate the n_{ID} the relationship between V_{oc} and light intensities, **Equation 5**. This equation shows the relationship between the V_{oc}, bandgap (E_g), thermal voltage, ideality factor, and logarithmic dependence on light.

Equation 5. $$e \cdot V_{OC} = m \cdot E_g + n_{ID} \cdot k_B \cdot T \cdot m \cdot ln\frac{G}{G_0}$$

Where e is the electron charge, m is the number of equal cells connected in series, E_g is the light absorber bandgap, k_B is the Boltzmann constant, T is the temperature, G is the irradiance or light intensity, and G_0 is a constant with the same units than G.

A complete interpretation of n_{ID} for PSC was reported in (Tress et al., 2018), corresponding ***Figure 2-23*** to the figure of merit of their work intended to illustrate its interpretation. In this scheme, they suggested three examples according to the slope between V_{oc} and light intensities. Example **A** is related to the band to band recombination, characterized by higher V_{oc} and moderate slope of 60 mV/dec. Example **B** is related to SRH recombination in bulk, characterized by intermedium V_{oc} values and a higher slope of 100 mV/dec. Example **C** is related to surface recombination on contacts, characterized by lower V_{oc} and a decreasing slope at high light intensities. Consequently, a general overview between the involved variables is established, allowing identification of the dominant recombination mechanism in the device.

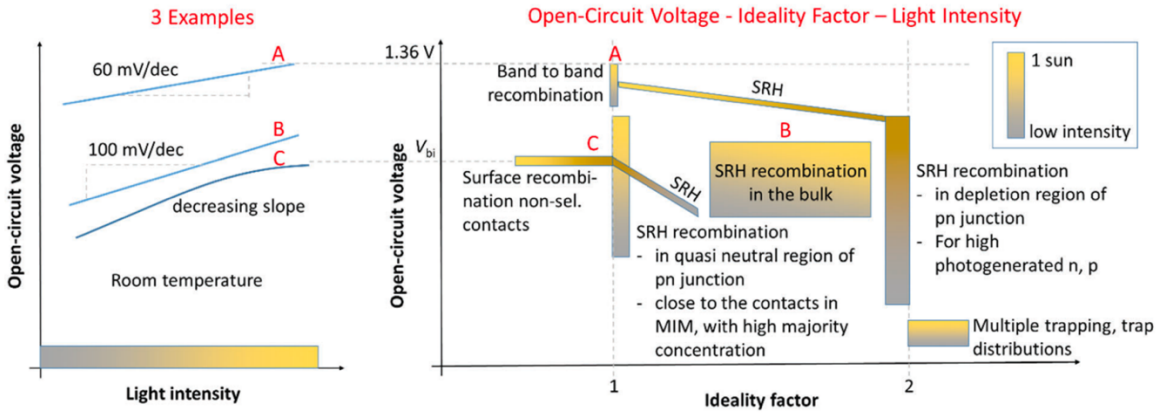

Figure 2-23. Interpretation of Ideality factor.

Here three different recombination mechanisms are illustrated and correlated with the V_{oc} sensitivity to light intensities, taken from (Tress et al., 2018).

To characterize perovskite devices according to **Equation 5**, a procedure using a solar simulator and optical filters was implemented to estimate the n_{ID} values. ***Figure 2-24*** shows some results published in previous works (Yoo et al., 2021, 2020), allowing identification of the surface recombination of this kind of perovskite devices, according to the behavior depicted at higher irradiances (V_{oc} decreases as the irradiance increases, indicating a decreasing slope, Case C in ***Figure 2-23***). Hence, the V_{oc} was calculated as the average value recorded for one minute at every light condition (***Figure 2-24***b). Then, the n_{ID} values were estimated according to **Equation 5** (***Figure 2-24***c).

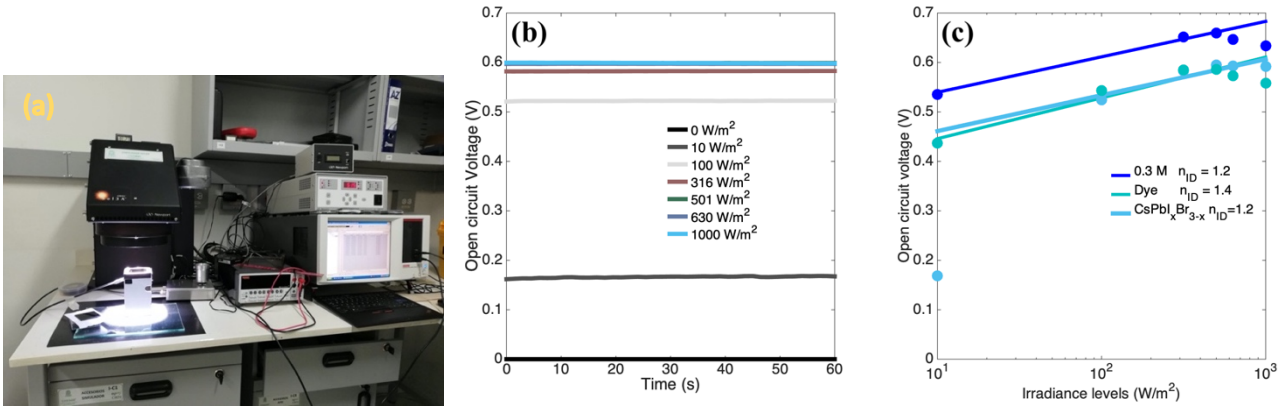

Figure 2-24. Procedure to estimate the ideality factor value.

a) *Experimental setup to measure the V_{oc} dependence on light using an Oriel sol3A sun simulator (Newport Corporation, Irvine, CA, USA), optical filters to change the light intensity, and a 4200SCS Keithley system (Tektronix, Beaverton, OR, USA) to record the V_{oc}.* ***b)*** *Voc recorded for one minute at each light intensity.* ***c)*** *estimated n_{ID} according to* ***Equation 5****.*

Figure 2-25 shows 5 representative cases obtained for the evaluation of various minimodules following the procedure shown in ***Figure 2-24***. The estimated n_{ID} values ranged between 1.1 and 2.1, suggesting in a general way the SRH recombination in bulk according to the interpretation shown in (Tress et al., 2018). Besides, based on the behavior displayed by V_{oc} as a function of light intensity (plot-shapes), it is not observed surface recombination in the modules. Hence, this procedure allows us to estimate reliable n_{ID} values representing the V_{oc} dependence on the light in a broad range of the light intensities (100 – 1000 W/m^2), pointing to the recombination process in the device.

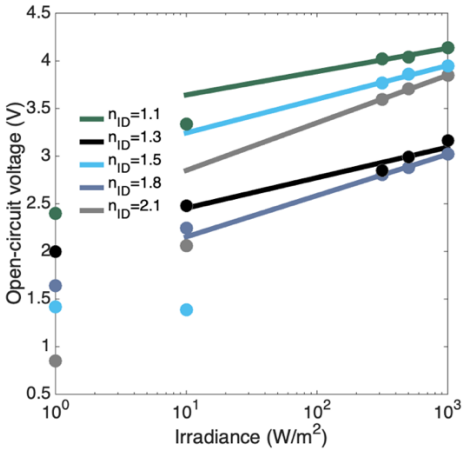

Figure 2-25. Ideality factor estimation for minimodules under indoor conditions.

Representative cases of evaluated minimodules are displayed. Each color corresponds to a particular minimodule. Color points correspond to experimental data, and solid color lines correspond to the fit between irradiance and V_{oc}. n_{ID} values were estimated in accordance with ***Equation 5.***

2.2.2.3 Estimated n_{ID} from Impedance Frequency Response

In indoor tests, excellent agreement between the n_{ID} values estimated from V_{oc}-*light intensity* data in accordance with **Equation 5** and the results of IFR analysis in accordance with **Equation 6** has been observed (Almora et al., 2018; Yoo et al., 2020). In this sense, an Autolab procedure was implemented to systematize the experimental process and estimate the n_{ID} values using both methodologies, ***Figure 2-26***. Hence, the first step is defined by the number of light conditions (LC) related to 1 sun. For instance, 0 is related to the dark condition, and 1 is associated with 1 sun; other values are related to the fraction of 1 sun. The loop allows the evaluation of each LC, which is defined by the optic filter. Once the time the filter is located and the LC is reached (gray box), the open-circuit voltage is recorded for 1 minute (light blue box). From the V_{oc} behavior over time, the average value is estimated (green box). This average value is used to estimate the n_{ID} value from the relationship between V_{oc} and light intensity in accordance with **Equation 5**. Besides, the last value is set up as bias (blue box) to perform the IFR in two directions to check the reproducibility of the measurements, from high to low frequencies (down) and from low to high frequencies (up). After the evaluation of the LCs, the sample is kept for 1 minute at the open circuit to stabilize the V_{oc}. Finally, the I-V curve at 1 sun is recorded (orange box) between -0.5 V and $1.2V_{oc}$. Usually, all tests are performed using an AC amplitude signal of 10 mV and room temperature (approximately 25ºC). After the test, the IFRs are fitted to the equivalent circuit shown in ***Figure 2-21*** to calculate the recombination resistance (R_{rec}) considering negligible transport and charge transfer resistances in both bulk and contact layers and interfaces (Contreras-Bernal et al., 2019; Fabregat-Santiago et al., 2011; Yoo et al., 2020). Then, n_{ID} can be calculated from the slope of the logarithmic plot of R_{rec} vs. V_{oc} in accordance with **Equation 6** (Contreras-Bernal et al., 2019; Fabregat-Santiago et al., 2011; Yoo et al., 2020).

Equation 6. $$R_{rec} = R_{00} e^{\left(\frac{-q \cdot V}{n_{ID} \cdot k_B \cdot T}\right)}$$

Where R_{00} is an independent parameter with resistance units.

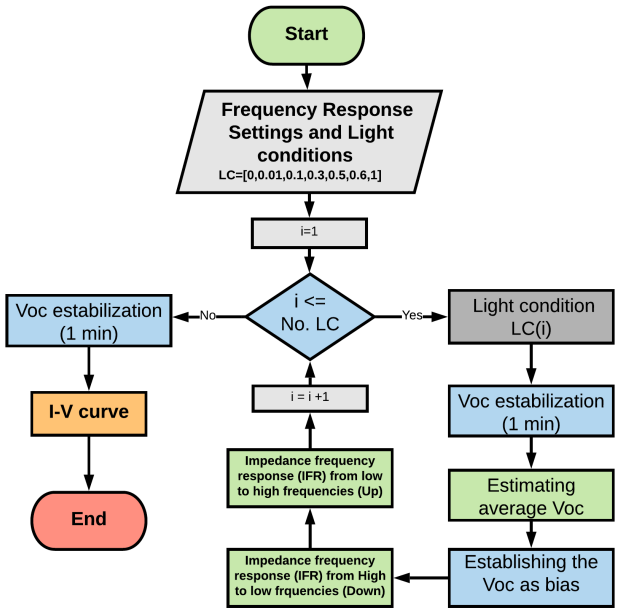

Figure 2-26. Flowchart to measure the IFR and V_{oc} dependence on light.

The light conditions (LC) are related to 1 Sun, corresponding 0 to dark and 1 to 1 Sun. These conditions are changed by optical filters. In this way, the impedance frequency response is performed at each light intensity considering the average V_{oc} recorded during 1 minute as bias and scanned in two ways, from high to low frequencies (down) and from low to high frequencies (up). Finally, at 1 sun, the I-V curve is recorded.

To illustrate the procedure shown in ***Figure 2-26***, ***Figure 2-27*** shows the results of evaluating this procedure for the cells analyzed in ***Figure 2-24***. From these results, important facts could be highlighted. First, the IFR changing the light intensity (***Figure 2-27***a) allowed reducing electrical noise comparing with the IFR changing the bias and fixing the light intensity at 0.1 sun (***Figure 2-27***b). Consequently, better-defined impedance patterns are obtained. Second, in both cases for the evaluated cases, the equivalent circuit used to fit the impedances adequately reproduces the impedance behaviors, indicating the accuracy of the optimization process employed to fit the impedance and extract the electrical parameters. Third, from the calculated R_{rec} values as a function of bias or V_{oc} (for IFR changing the light intensity), the n_{ID} values calculated using **Equation 5** (light) show excellent agreement with the n_{ID} values calculated using **Equation 6** (bias), ***Figure 2-27***c. The implemented procedure validated the calculation of n_{ID} and the recombination process of devices (surface recombination).

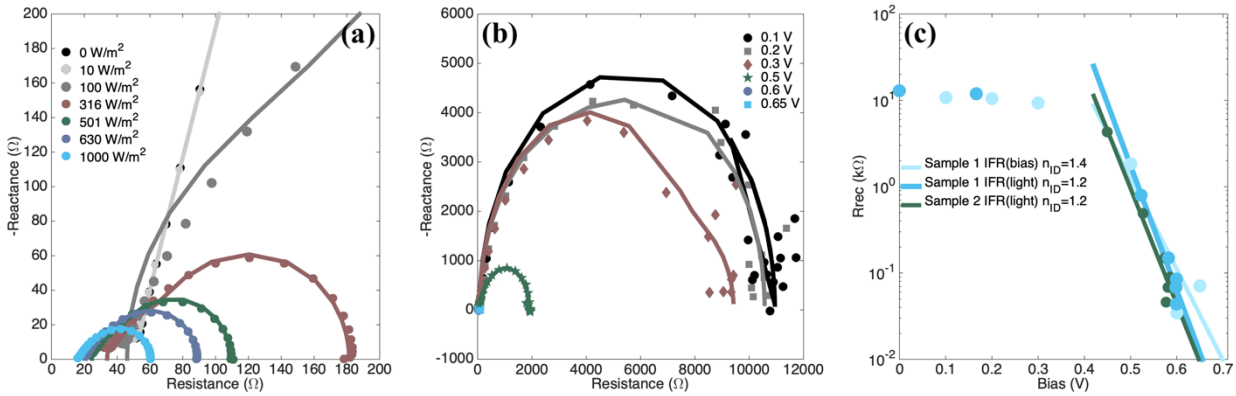

Figure 2-27. Ideality factor estimated from IFR.

a) *Nyquist diagrams of impedance as a function of the light intensities (dots) and their corresponding fit (solid lines).* ***b)*** *Nyquist diagrams of impedance as a function of the bias (dots) keeping constant the light intensity (0.1 suns) and their corresponding fit (solid lines).* ***c)*** *Estimated n_{ID} values considering both conditions: changing the light conditions and changing the bias keeping constant the light condition at 0.1 suns.*

2.3 Conclusions

Here, minimodules of approximately 8 cm^2 and 4 sub-cells connected in series were fabricated. These were optimized, considering the active area allowing efficiencies higher than 10 % on monolithic solar cells and performing the scribe lines called P1, P2, and P3. Moreover, these were encapsulated with EVA. Finally, fabricated devices were characterized by the I-V curve, impedance frequency response, and ideality factor.

From the I-V curves, the reached higher efficiencies (close to 12 %) were in the current range reported in the literature for minimodules with a similar area, that is, between 10 and 17 % (Liu et al., 2020). The extracted parameters from the minimodule's I-V curves demonstrated consistent V_{oc} values (close to 4 V corresponding to the voltage of 4 cells connected in series) comparing with those obtained for monolithic solar cells. Besides, the higher FF allowed validation of the interconnection process performed to reduces electrical losses. This is the main advantage of the series connection of cells instead of large-area solar cells.

From impedance frequency response, the impedance spectra of the incomplete cells (without ETL), cells, and minimodules were analyzed. Observing the advantages of the electron transport layer to increase the dielectric effect and extract the electrons. Also, main features related to the frequency behavior, such as the phase peak, cut-off frequencies, among others features, were observed. Hence, to improve the characterization of the IFR spectra, an optimization process was developed to fit the impedances to the equivalent circuit shown in ***Figure 2-21***, which combined the genetic algorithm and the Simplex method to reduce the error between the experimental and calculated data. The fitted circuit model successfully reproduced the impedance patterns under different light conditions (dark and 1 sun).

Relating to the ideality factor, an experimental procedure was implemented to estimate the n_{ID} based on the relationship between V_{oc} and light intensities and based on the relationship between the bias and R_{rec} obtained from the IFR analysis. Demonstrating an excellent agreement with the n_{ID} values calculated for both methodologies, as was shown in ***Figure 2-27***. Based on the previous literature reports, it was possible to identify the SRH recombination mechanism dominating this kind of device based on the n_{ID} values ranging between 1 and 2. Therefore, a numerical and experimental tool to characterize the devices were developed. Moreover, the I-V curves of nonencapsulated perovskite solar cells of approximately 2 cm^2 of an active area were fitted to the one-diode model to reproduce the electrical behavior, ***Figure 2-22***. Hence, an optimization process combining genetic algorithm and Simplex method was implemented to illustrate some drawbacks reported in the literature related to the parameter extraction, such as local solutions. Therefore, the results also indicated that efficient devices are correlated with n_{ID} ranging between 1 and 2. Nevertheless, it is worth noting that in this process to estimate the ideality factor, the effect of series resistance is involved, while in the procedure to estimate this parameter from the V_{oc} and light intensity, this effect is neglected. Hence, this last procedure could be considered more suitable to characterize these devices to study the recombination process and correlate this behavior with the performance.

Therefore, the devices were characterized not only by the I-V curve data but also by the ideality factor and impedance spectrums. In this regard, a Autolab procedure was implemented to estimate the n_{ID} under indoor conditions, in accordance with the flowchart shown in ***Figure 2-26***. This characterization could be used to track the performance evolution or degradation process for the devices under indoor or outdoor conditions.

3. Outdoor Performance (OP)

This chapter proposed a methodology to evaluate the perovskite solar devices' outdoor performance. This methodology was previously described in (Velilla et al., 2019b), considering the five power rating conditions according the International Standard IEC 61853-1, including the Standard Test Condition (STC) and Nominal Operative Cell Temperature condition (NOCT). Hence, a monitoring system was implemented to register and process the weather (temperature and irradiance) and electrical data (extracted from the I-V curve) in accordance with the proposed methodology. Moreover, based on the well-agreement between power rating conditions measured under outdoor conditions for different commercial technologies such as silicon, HIT, and CIGS, and the manufacturers' reported values in its datasheets, the monitoring system, and methodology were validated (Velilla et al., 2019a). Finally, from the outdoor performance of perovskite minimodules, a positive dependence of V_{oc} and P_{max} on temperature and irradiance was observed. The results indicate that PSCs show lower correlations of their performance and open-circuit voltage with the temperature than other commercial technologies, such as silicon, for which the deleterious effects of temperature on performance are well known. This difference in temperature sensitivity is a significant and competitive aspect of PSC technology that could provide new characterization opportunities.

3.1 Outdoor Performance Evaluation

The I-V curves conventionally defined the performance of solar devices according to temperature and illumination conditions. In this way, the Standard Test Conditions (STC) defined as 1000 W/m^2 of irradiance and 25 ^{0}C of cell temperature is the most common conditions to measure the I-V curve in order to extract the main parameters to describe the electrical performance of the solar device as efficiency, P_{max}, V_{oc} and I_{sc} (IEC 61215, 2003). STC is commonly measured under indoor conditions, addressed in the datasheet, and used to evaluate different solar technologies' progress over time (Green et al., 2020). As the STC conditions rarely occur outdoor (Dash et al., 2017), to evaluate the performance in real operating conditions, a systematic analysis of high quantity data is required to take into account the illumination and temperature variations induced by day-night, seasonal, and weather conditions (Wang et al., 2018). Nevertheless, considering that NOCT is defined as the equilibrium mean solar cell junction temperature of the module in the describe environment (IEC 61215, 2003) and these conditions are possible to achieve under outdoor test conditions (Velilla et al., 2019a), the outdoor performance of solar devices could be evaluated in a proper way at NOCT. In this way, considering various conditions such as STC and NOCT allows improving the characterization of weather variables' impact on the device's performance under outdoor conditions.

Related to performance, International Electrotechnical Commission (IEC) published a series of standards in IEC 61853 intended to establish the requirements for evaluating the performance of all photovoltaic technologies in term of power (IEC 61853-1, 2011) or term of energy and performance ratio (IEC 61853-3). In the case of energy, it is worth noting that the study involves another inverter's performance. For that, the performance depends not only on the solar device to be evaluated but also depends on the electronic device's efficiency and the maximum power tracking algorithm (Eltamaly et al., 2018). In the case of power, the study is mainly based on the I-V curve's extracted parameters representing the device's performance. Allowing the device's characterization at the maximum power point (MPP) or other operative points as the short circuit current, open-circuit voltage, Etc. Therefore, the standard called "Photovoltaic (PV) module performance testing and energy rating – Part 1: Irradiance and temperature performance measurements and power rating" allows status validation

devices of any solar technology, defining a pass/fail criteria, in which the success is reached if the power rating conditions measured fall within the power range specified by the manufacturer (IEC 61853-1, 2011). Corresponding the 5 power rating conditions to:

- Standard Test Condition (STC), defined at 1000 W/m^2 and cell temperature of 25 ^{0}C
- Nominal Operating Cell Temperature (NOCT), defined at 800 W/m^2 and ambient temperature of 20 ^{0}C
- Low Irradiance Condition (LIC), defined at 200 W/m^2 and cell temperature of 25 ^{0}C
- High Temperature Condition (HTC), defined at 1000 W/m^2 and cell temperature of 75 ^{0}C
- Low Temperature Condition (LTC), defined at 500 W/m^2 and cell temperature of 15 ^{0}C)

Consequently, the evaluation provides a complete device's characterization under various values of irradiance and temperature, allowing determination of the impact of weather variables on P_{max}, V_{oc}, I_{sc}. Besides, this characterization could be carried out using a solar simulator and specialized equipment to set up the temperature and illumination conditions or natural sunlight with and without a tracker.

Conventionally, solar device's performance evolution is monitored through the systematic measurement of I-V curves considering the temperature and illumination conditions. It is relatively easy to set up tests in the laboratory to track the performance at the maximum power point; however, such control is intrinsically unreasonable outdoors. The illumination and temperature variations induced by day-night, seasonal, and weather conditions necessitate a systematic analysis of a high quantity of data, depending on the measurement sampling rate and exposure time (Wang et al., 2018). Hence, in such power loss studies, it is common to correct for temperature and irradiance in the I-V curves in accordance with the standard test conditions (STC, corresponding to an irradiance of 1000 W/m^2 and a module temperature of 25 °C). However, such conditions are difficult to reach outdoors (Velilla et al., 2019a). Nevertheless, in a general way, the outdoor performance mainly is referenced to the observation of one variable over time, as the efficiency (Gaglia et al., 2017; Hamou et al., 2014; Makrides et al., 2008), maximum power (Velilla et al., 2014), series resistance (Deceglie et al., 2015), among others. In these cases, the evaluation could be affected by different factors such as weather conditions, seasonal variations, installation conditions, shading and soiling effects, Etc (Makrides et al., 2014; Visa et al., 2016). Nevertheless, the evolution of these variables over time has been commonly fitted using statistical methods such as linear regression to estimate the performance loss over time (Phinikarides et al., 2014).

In the case of emerging technologies such as PSCs, no international standards have been fully established, and most published works have focused on laboratory-scale cells (i.e., 1 cm^2 or smaller in size); consequently, various methods and materials have been used to evaluate the stability and degradation performance of these technologies (Anoop et al., 2020; Cheacharoen et al., 2018; Domanski et al., 2018; Holzhey and Saliba, 2018; Tress et al., 2019; Yang et al., 2015). In this regard, a broadly-supported consensus statement on reporting data related to stability assessment was recently published, highlighting certain particularities of PSC technology that must be taken into account (Khenkin et al., 2020). For instance, in contrast to mature photovoltaic technologies such as Si and GaAs, PSCs show performance loss reversibility under day-night cycles (Domanski et al., 2017; Khenkin et al., 2018); a hysteresis effect in the current-voltage (I-V) curves, which could induce errors in performance determination (Christians et al., 2015); and a lower dependence of performance and V_{oc} on temperature (Schwenzer et al., 2018). Nevertheless, while these peculiarities of PSCs could be seen as drawbacks for their systematic analysis, they also provide new characterization opportunities (Hoye et al., 2017). This technology is in its infancy, and there are few statistical data

available for large devices operated outdoors (Hu et al., 2019). Therefore, insufficient data are available to fully establish or identify the degradation modes and mechanisms of PSCs and their impact on outdoor performance evolution.

Related to perovskite, the International Summit on Organic Photovoltaic Stability (ISOS) suggests 3 protocols for outdoor. ISOS-O-1 suggests periodically record the J-V curve at STC using a solar simulator (indoor). ISOS-O-2 suggests periodically record the J-V curve under outdoor conditions, keeping the device at the Maximum Power Point (MPP) or open-circuit voltage. In contrast, the ISOS-O-3 suggests periodically recording the J-V curve using a solar simulator, keeping the device at MPP. Despite that these cases are related to outdoor, the electrical characterization is usually performed under indoor conditions to evaluate the performance degradation over time or device stability under the conditions suggested by the protocols. Hence, the protocols suggest reporting the normalized data (per unit) considering the first value to normalize the data and obtain the degradation behavior to estimate degradation rate or lifetime according to the accepted definition.

Considering that ISOS-O protocols and IEC 61853-1 standard are based on the data extracted from the I-V curve, the outdoor performance of perovskite technology could be estimated with no trouble based on the IEC, including different power rating conditions to evaluate the impact of weather variables on performance. This procedure could be applied to evaluate any technology.

3.2 Monitoring System to Evaluate the Outdoor Performance

The outdoor monitoring station was implemented in the facilities of the Solar Cell Outdoor Performance Laboratory of the University of Antioquia (OPSUA) in Medellín-Colombia (6° 15′ 38″ N 75° 34′ 05″W, facing south at a fixed angle of 10°) intended to evaluate the outdoor performance of solar devices under natural sunlight without a tracker. The performance of photovoltaic technologies could be evaluated in terms of power (***Figure 3-1***) measuring the I-V curve of devices under different illumination and temperature conditions. In this sense, the monitoring system was implemented to record and store the weather variables (irradiance and temperatures, ***Figure 3-2***a) and electrical data (I-V curve, ***Figure 3-2***b). These data are processed to estimate the impact of weather variables on performance (Outdoor performance). Finally, based on the outdoor performance (OP), the status and performance of photovoltaic devices could be estimated considering the power rating conditions suggested by IEC 61853-1.

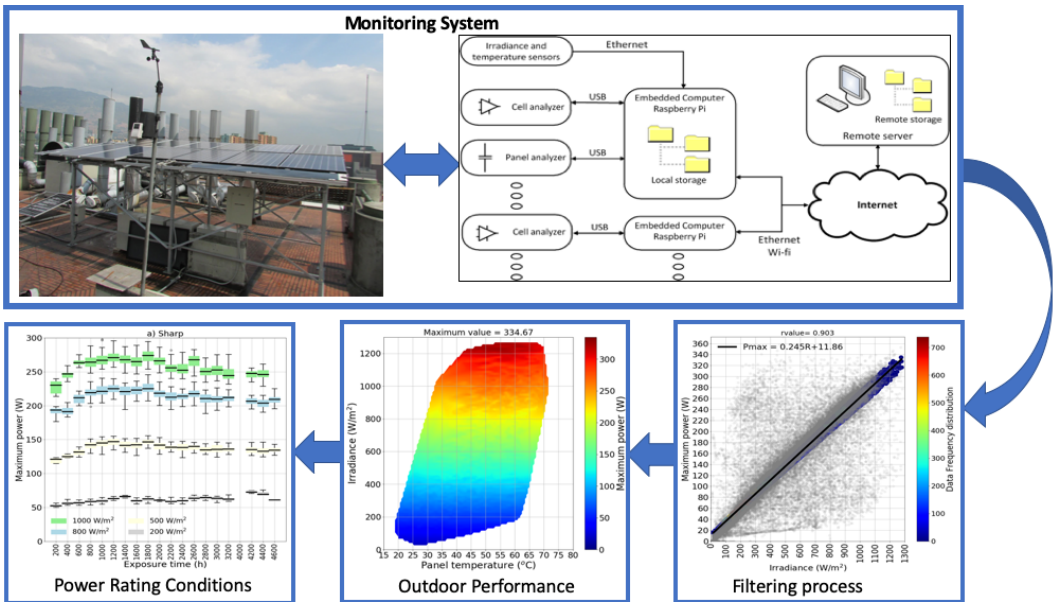

Figure 3-1. Schematic to evaluate the outdoor performance.

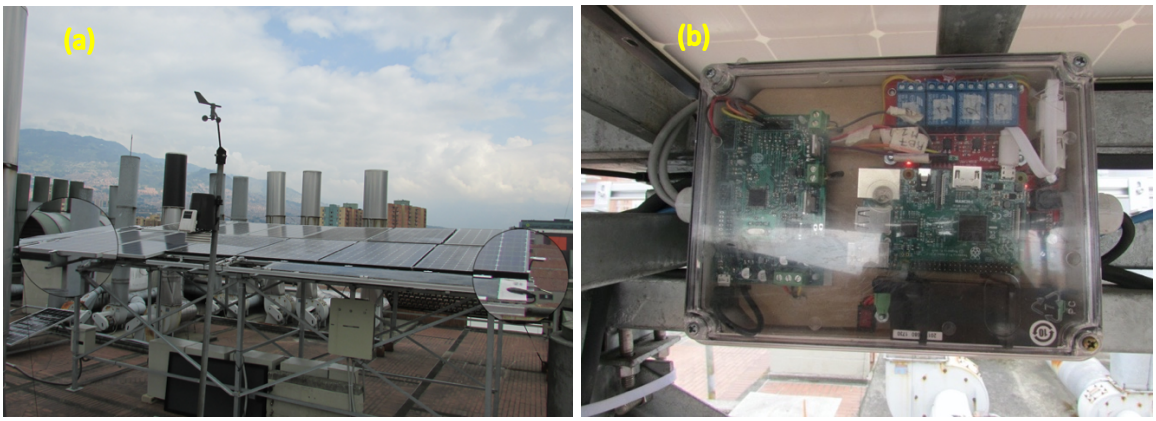

Figure 3-2. The Outdoor Monitoring Station to evaluate the outdoor performance.
a) *zoom to weather sensors.* ***b)*** *Photo of the developed solar cell tracer installed to record the I-V curves under outdoor conditions.*

3.2.1 Weather Variables

To record the weather variables, the irradiance was measured using two Spektron 210 sensors by TRITEC International located at the end of the solar station, to validate the values recorded. Ambient and panel/cell temperatures were measured using PT-1000 sensors by TRITEC International. Ambient temperature sensors were located close to irradiance sensors (***Figure 3-2***a), and the surface temperature sensors were located on the back of the devices under test. The weather data were collected using a Sensor Box Datalogger by FRONIUS International. These data are available online. Besides, two Raspberries were programmed to read the weather data from the datalogger via Ethernet communication every minute for local storage, keeping the same text file (CSV) and including the timestamp. Finally, the records (irradiance levels and temperatures) are synchronized every hour with a remote server using Rsync service on SSH (***Figure 3-1***).

3.2.2 I-V Curve Tracers

To measure the I-V curve of solar devices, different hardware techniques have been used (Duran et al., 2008). For instance, a resistor is connected to the device under test (DUT), changing the resistance between a value close to zero (short circuit) and a higher value considered as the open circuit (Nikoletatos and Halambalakis, 2018). It is remarked that additional hardware is required to change the resistance value, such as potentiometer-motor systems, relay commuted series and parallel resistors arrays, digital potentiometers, among others (Van Dyk et al., 2005). Moreover, MOSFET transistors have been used as variable loads for I-V curve measurement, allowing easier control of the DUT operation point without the intervention of mechanical or electromechanical devices (Hassaine et al., 2014; Papageorgas et al., 2015; Willoughby et al., 2014; Willoughby and Osinowo, 2018). In both cases, heat dissipation is a concern, limiting the applicability to high-power solar panels. Furthermore, DC/DC converters are used on I-V curve characterization (Enrique et al., 2005; Faifer et al., 2015). In this case, a Pulse Width Modulation (PWM) signal controls the operation points of DUT, allowing controlling the sweep over the I-V curve. However, this technique's complexity and the number of components increase compared to the resistive or transistor load technics.

On the other hand, capacitive loads have also been reported to measure the I-V curve (Agroui, 2012; Cano et al., 2015). These devices work by connecting a discharged capacitor to the DUT, registering the voltage and current waveforms during the transient response. This technique has several advantages; it is suitable for high-power applications; the capacitor dynamics achieve the sweep over the curve without using any external mechanism; the capacitor has no heat dissipation issues. However, it is impossible to modify the scan direction (from short circuit to open circuit) and the sweep speed because it depends on the capacitance, DUT characteristics, and light conditions.

Also, it is possible to use a controlled voltage source to trace the I-V curve (Duran et al., 2008), allowing a complete characterization including the reverse bias region and voltages higher than the open-circuit voltage. Therefore, it is possible to directly control the voltage change rate (V/s rate) and control the sweep direction (forward and reverse), making it practical for hysteresis measurements (Li et al., 2017). However, this technique involves an additional power supply increasing costs and system complexity.

Taking into account the advantages and disadvantages of the aforementioned techniques, two different types of I-V curve tracers (solar analyzer, SA) were implemented. The I-V curve tracers are an improved version of previous work (Cano et al., 2015), intended to improve portability, local data storage, low cost, and faster response (Velilla et al., 2019a). One SA is based on the capacitive load technique due to simplicity, power dissipation, and cost concerns. This prototype is intended for devices that operate for voltages up to 250 V and currents up to 12.5 A (solar panels, ***Figure 3-3***a-b). Another SA is based on the four-quadrant DC supply due to greater flexibility on sweep direction and speed. This prototype is intended for devices that operate for voltages up to 8 V and currents up to 3 A (solar cells and solar minimodules, ***Figure 3-3***c-d).

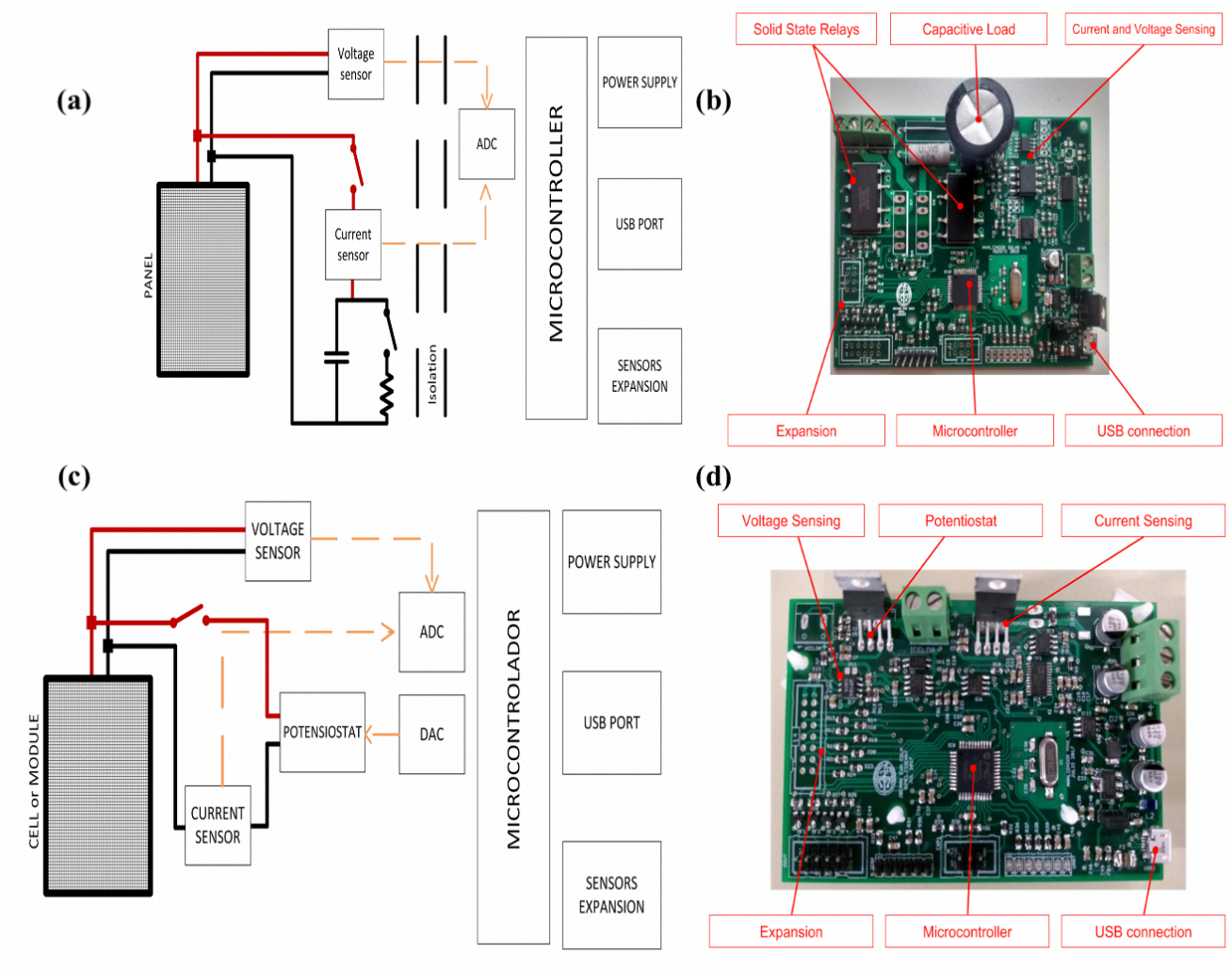

***Figure 3-3**. **Developed I-V curve tracers**.*
***a-c)** Box diagram of I-V curve tracers. **b-d)** printed circuit boards. Corresponding to potentiostat for solar panel **a-b)** and **c-d)** for solar cells or minimodules.*

In the case of the solar analyzer for panels, the potentiostat involved different elements, ***Figure 3-3***a. A capacitive load, solid-state relays for charging and discharging control, voltage sensor (AMC1200-Isolation amplifier, Texas Instruments), current sensor (ACS-711 series - Hall effect, Allegro), an analog to digital converter (ADC), and the microcontroller. The control and communication systems were implemented on a 32 bits microcontroller (PIC32MX230F064D, Microchip). For safety reasons, isolation between power (load, sensors, relays) and control circuit sections (microcontroller, communications) was implemented because the panel's voltage and current levels. Voltage and current signals are digitalized by a sigma-delta analog to digital converter (AD7172-2, Analog devices). Serial port interface communication was implemented between the converter and microcontroller. This setup allows sampling times of 0.32 ms for each I-V curve point (the total time to take a voltage sample sequentially and a current sample). Sampling time is critical to determine the minimum capacitance value required to measure the charging transient. A serial port emulation protocol was implemented over USB, providing a command set to control analyzer functions and retrieve data. Finally, the expansion sensors block allows direct connection to microcontroller's

analog-digital converter, intended for external sensor interfaces such as irradiance and temperature variables.

In the case of the solar analyzer for cells, the potentiostat circuit was implemented using linear circuits (operational amplifiers) due to the low voltage, current, and power of the solar cells (***Figure 3-3***c). The operational amplifiers series OPA548T by Texas Instruments was selected due to their output current characteristics. A trans-resistance amplifier configuration is used as a current sensor considering the identical operational amplifiers. A differential amplifier (LT1167, Linear Technologies) was used as a voltage sensor. A digital to analog converter (TLV5638, Texas Instruments) was used for the generation of the voltage references for the solar cells. Signal digitalization, processing, sensor expansion, and communications were carried out using the same components described for the panel analyzer.

In both cases, the potentiostats are programmed to connect the devices under test and record the V_{oc}. Then, the current and voltage values are registered (cell or panel). After the measure, the device is disconnected and keep in the open-circuit condition. Then, the data are sent via a USB port. Finally, to optimize the I-V curve process, an embedded computer (The Raspberry Pi 3) is connected to control each potentiostat and execute the following tasks:

a) System date and time are keeping updated using the Network Time Protocol Daemon (NTPD). It guarantees low error on measurement time stamps.
b) An SSH (Secure Shell) interface allows remote access to modify the system configuration settings (as measurement frequency, sensor calibration, Etc.) or scripts edition.
c) Cron service (Linux task programmer) is configured to execute every minute the python script to communicate the Raspberry with the potentiostat and start the measurement process. The registers (I-V data) are saved in a CSV file, including the timestamp.
d) Finally, CSV files are synchronized every hour with the remote server, using the Rsync service over SSH.

It is remarking that current and voltage sensors are calibrated to guarantee measurement accuracy before any on-field testing.

3.2.3 Proposed methodology to Estimate the Outdoor Performance

As mentioned before, electrical (I-V) and weather (irradiance and temperatures) records are uploaded to the remote server to provide backup, centralize the monitoring process, and process the data (***Figure 3-1***). In this sense, the implemented procedure to estimate the outdoor performance could be divided into two main parts: one part is related to the databases of exposed devices (which is framed into the flowchart shown in ***Figure 3-4***), another part is related to the analysis.

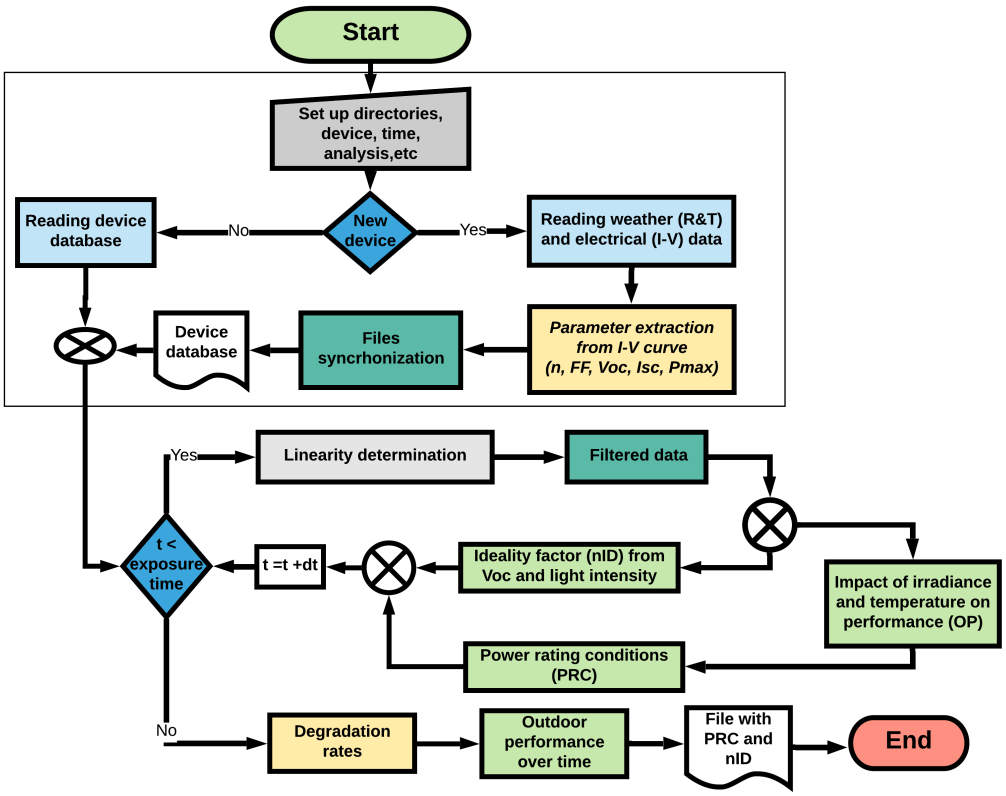

Figure 3-4. Flowchart to evaluate the outdoor performance.

Procedure to analyze and process the electrical data (I-V curve) and weather data (irradiance and temperature). In this way, atypical data o irradiance changes due to clouds or shades are minimized (linearity determination criteria). Then, the impact of weather variables on performance (OP), power rating conditions (PRCs), and ideality factor (n_{ID}) could be estimated.

The next steps are followed to construct the databases of devices:

a) The first step scans the text files related to weather variables (irradiance and temperatures) located in a specific folder (light blue box in the flowchart) to extract the values of the variables and organize the data by date (year-month-day-hour-minute-seconds). Here, two sensors of irradiance, ambient temperature, and surface temperature, are used to record the weather data during the exposure time.

b) The second step scans the text files related to I-V curve data located in a specific folder according to the solar tracer identification (light blue box in the flowchart). Hence, the electrical data (I-V curve) recorded during the exposure time by the solar tracer is processed to estimate the main parameters from the I-V curve data (Yellow box in the flowchart). In this process, different fitting processes are performed to improve the estimation of the main parameters (P_{max}, FF, V_{oc}, and I_{sc}). Moreover, the data is organized by date (year-month-day-hour-minute-seconds).

c) The third step correlates the weather data records (irradiance and temperature) with the I-V curve data records (Dark green box in the flowchart). Thus, for every set of main parameters extracted from the I-V curve records, their corresponding weather variables are assigned. With these organized data, a new text file is created, including the weather and electrical data (raw data). This CSV file could be read by other applications to perform different analyses.

The second part is related to the analysis. These analyses are included in the light green boxes in the flowchart, in which the arrows point out the sequences followed. In this sense, it is needed to highlight that before any analyses, the raw data were filtered based on the linearity determination criterion to minimize transient effects related to changes in irradiance, shadowing caused by clouds, or droplets. The linearity determination criterion is applied based on the linear behavior observed between P_{max} and the irradiance and validated by the coefficient of determination (r-value) (Velilla et al., 2019b, 2019a). ***Figure 3-5*** shows this procedure in three steps, one related to the raw data registered during the exposure time considered (***Figure 3-5***a), another related to the fit process performed to establish the linear behavior between P_{max} and irradiance. This consideration is reached if the estimated coefficient of determination (r-value) is close to 1 (***Figure 3-5***b). Finally, the best-fit data with a deviation of ±5 % is selected as the filtered data (***Figure 3-5***c), representing the exposure time's average conditions during.

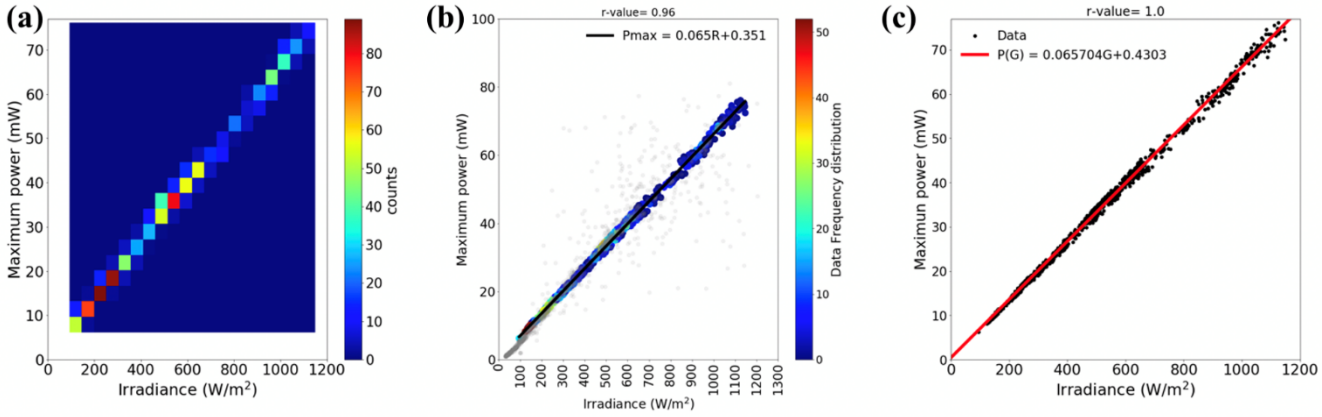

Figure 3-5**. **Linearity determination criteria.

***a)** Data distribution for 100 h of exposure. **b)** Procedure performed to filter the data from atypical data, related to unclear days, dirty or drop on the surface. At the top is shown the coefficient of determination (r-value) estimated from the fitting process between P_{max} and irradiance. Values close to 1 indicating a linear behavior between variables. The gray points correspond to data measured in the exposure time considered, and the color dots correspond to data considered as filtered and representative of the dataset. **c)** Filtered data marked as black points. In this case, the filtered data correspond to the average conditions during the exposure.*

Subsequently, the filtered data are used to perform the analyses:

a) **Outdoor performance (OP)**: the impact of weather variables on performance is estimated, considering the filtered data. The results are usually depicted in a map to illustrate the performance as a function of irradiance and temperature, representing the average outdoor performance during the evaluated time and indicating the variables' operative range (***Figure 3-6***a). A full description of these maps was shown in previous work (Velilla et al., 2019b, 2019a).

b) **Power rating conditions (PRCs):** the data shown in the form of maps (the average OP) are filtered considering a deviation of 5% from the irradiance levels corresponding to the power rating conditions indicated by IEC 61853-1 as previously mentioned, that is, 1000 W/m^2, corresponding to standard test conditions (STC); 800 W/m^2, corresponding to NOCT conditions; 500 W/m^2, corresponding to low-temperature conditions (LTC); and 200 W/m^2, corresponding to low-irradiance conditions (LIC). Hence, each power rating condition's data deviation is considered by the median value of data considered in each sampling time, ***Figure 3-6***b.

c) **Ideality factor (n_{ID}):** n_{ID} is calculated in accordance with **Equation 5** considering the filtered data and processing the data at different ambient temperatures between 25 and 35 ^{0}C (***Figure 3-6***c). Consequently, because different ideality factors can be calculated, the median value is considered the average value to consider the data dispersion representing the evaluated time window.

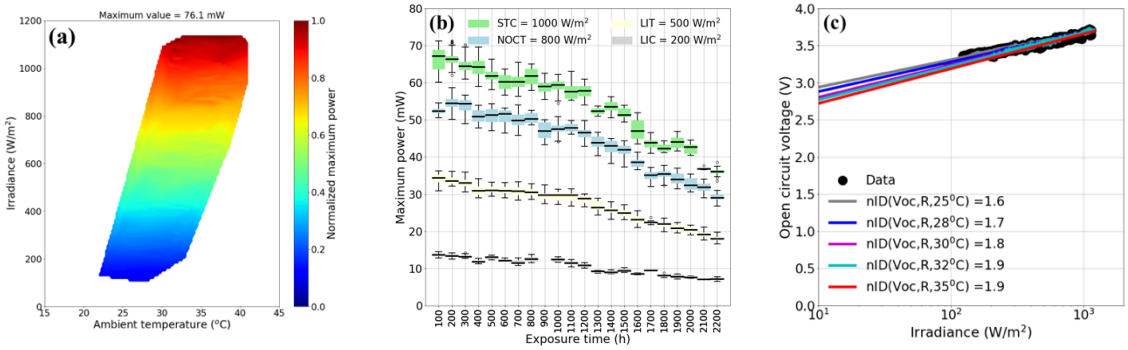

Figure 3-6. Outdoor analysis.

a) *Outdoor performance displayed in the form of a map to show the impact of weather variables on performance. This impact could be observed in other variables such as I_{sc}, and V_{oc}.* ***b)*** *Calculated PRCs over time by filtering the data by the irradiance levels defined by the power rating conditions.* ***c)*** *Ideality factor estimated considering the ambient temperature and the data shown in figure a).*

Finally, it is worth noting that these analyses are considered by the loop included in ***Figure 3-4***. For that, it is possible to divide the data by sets (batches) to estimate the average impact of weather variables on performance (OP), the power rating conditions or power loss tendency (degradation-shape), and ideality factor in every dataset (batch). Therefore, it is possible to analyze the performance's changes over time.

3.3 Evaluation of Outdoor Performance of Commercial Technologies

To validate the monitoring system and the proposed methodology to estimate the OP, commercial photovoltaic modules such as monocrystalline silicon (Sharp NU-RC290 and Yingli YL275D-30b), HIT (VBHN330SJ47), and CIGS (Miasolé Flex-02 120N) were monitoring under outdoor conditions, Table 3-1. The selection of these devices was mainly based on the datasheet specifications, including the STC and NOCT conditions. Therefore, the status of devices according to the datasheet could be evaluated following the procedure shown in ***Figure 3-4***.

Accordingly, ***Figure 3-7*****a,d,g, and j** show the relationship between irradiance and P_{max}. These data are processed by the linearity determination criterion to minimize transient effects related to changes in irradiance, shadowing caused by clouds or droplets, or atypical data (Velilla et al., 2019b). Then, these filtered data are shown in the form of a map to visualize the impact of weather variables on performance, ***Figure 3-7*****b,e,h, and k**. Finally, the outdoor performance over time was obtained by calculating the OP observed in the measurement sets, each of which contained measurements recorded over 200 hours of outdoor exposure (see ***Figure 3-7*****c,f,i, and l**). The data in each set were filtered considering a deviation of 5% from the irradiance levels corresponding to the power rating conditions (PRCs) indicated by IEC 61853-1(IEC 61853-1, 2011). The variables were recorded every minute during daylight hours, and the time considered to obtain the average OP was 200 h. This time is long enough to consider the data recorded in each set to be statistically valid, allowing reliable average values for tracking the performance evolution.

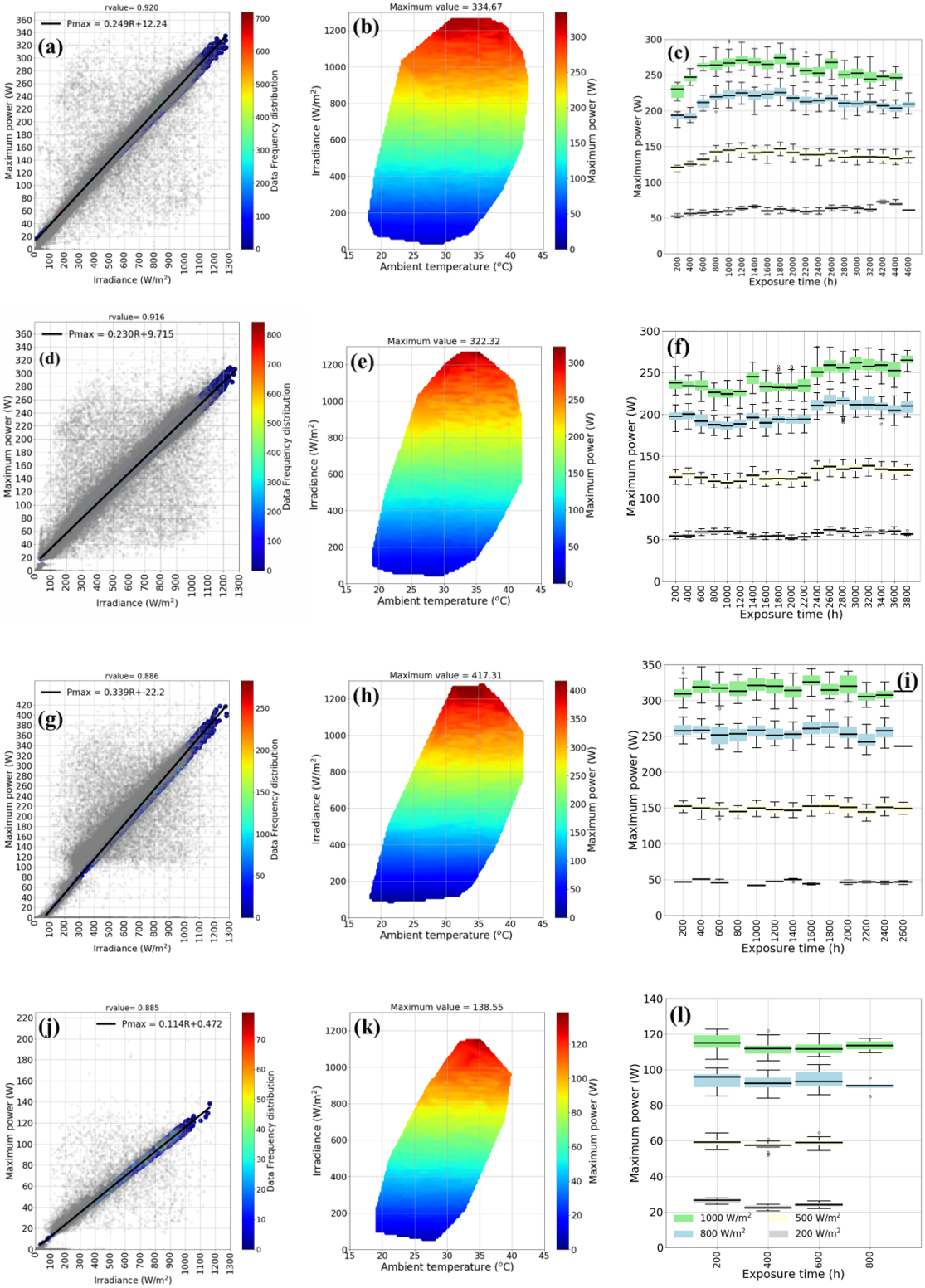

Figure 3-7. Impact of weather variables on performance.

*Corresponding **a-c)** to Sharp NU-RC290 (silicon monocrystalline), monitored between 2018-07-05 and 2019-01-20, **d-f)** to Yingli YL275D-30b (silicon monocrystalline), monitored between 2018-11-22 and 2019-04-24. **g-i)** to HIT VBHN330SJ47 (HIT), monitored between 2019-02-23 and 2019-06-03 and **j-l)** to Miasolé Flex-02*

120N (CIGS), monitored between 2019-05-09 and 2019-06-03. a,d,g, and j) Relationship between Pmax and irradiance. b,e,h, and k) Power delivery map as a function of irradiance and ambient temperature, the maximum value of power delivery is displayed at the top of each map. The color bar indicates the variable range. c,f,i, and l) Power rating conditions estimated by the dataset of 200 h of exposure. The block colors are related to the PRC as follows: green to 1000 W/m² (STC), blue to 800 W/m² (NOCT), yellow to 500 W/m² (LTI), and gray to 200 W/m² (LIC).

Despite the maps of power delivery allowed us to graphically visualize the impact of irradiance and temperature on devices' performance, two main points must be remarked. First, this performance is related to the most frequent conditions during the exposure time (average conditions). Second, due to the setup was carried out on tropical weather conditions, it is to expect that some PRC such as STC, HTC, and LTC rarely occur. Therefore, some PRC could not be included in the maps because these conditions could not be statistically representative. ***Figure 3-8*** shows the outdoor performance considering the device temperature to illustrate that lower temperature (lower than 25 ºC) correlated with lower irradiance (lower than 400 W/m^2). Therefore, the LTC and STC defined at 15 and 25 ºC, respectively, are omitted. Nevertheless, due to the exposure time exceeding 800 hours and the sampling time between measurements was 1 minute, the amount of data recorded is statistically, and the maps represent the average performance during the considered exposure time. Also, other PRC can be estimated using an extrapolation process as suggests (IEC 60891, 2009).

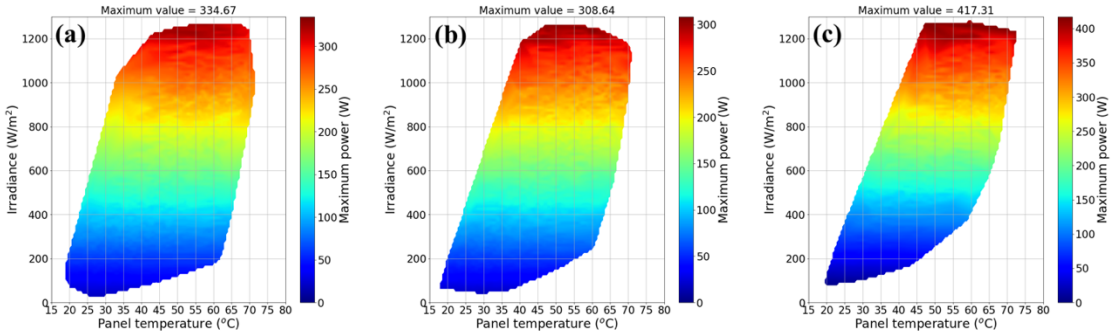

Figure 3-8. Outdoor performance as a function of device temperature. *Corresponding **a)** to Sharp NU-RC290 (silicon monocrystalline), monitored between 2018-07-05 and 2019-01-20, **b)** to Yingli YL275D-30b (silicon monocrystalline), monitored between 2018-11-22 and 2019-04-24. **c)** to HIT VBHN330SJ47 (HIT), monitored between 2019-02-23 and 2019-06-03. The color bar indicates the variable range.*

Because the devices were not cleaned during the exposure, to observe the changes over time on the PRC suggested by IEC 61853-1, taking into account the soiling and seasonal effects, the databases were processed by batches, ***Figure 3-7*****c,f,i, and l**. Every batch included the measurements recorded for 200 hours. These data are shown in the form of a boxplot to illustrate the measurements' median and standard deviation. Besides, due to the manufacturers commonly supplied the STC and NOCT on the datasheet, but not other conditions, these two PRC's average values over the exposure time were compared with manufacturers' data (**Table 3-1).** Hence, it is remarking that the NOCT was the most suitable power rating condition representing the outdoor performance, being the error within the range ± 5% for the evaluated modules. Moreover, normalizing the NOCT mean values concerning the manufacturer data (***Figure 3-9***), it was observed that most parts of exposure time the devices were within the range of ± 5 % (Velilla et al., 2019a). Therefore, the evaluation of the NOCT under outdoor conditions could be used to check the status of devices concerning manufacturer data and define cleaning maintenance or to identify the most suitable conditions of the device.

Table 3-1. STC and NOCT conditions for solar devices supplied by the manufacturer and obtained for the outdoor test.

Devices	Variables	STC (1000 W/m^2)				NOCT (800 W/m^2)			
		Data sheet	Mean	std	Error (%)	Data sheet	Mean	std	Error (%)
Sharp NU-RC290	P_{max} (W)	290	257.33	8.31	11.26	212	212.78	6.78	-0.36
	I_{sc} (A)	9.8	10.26	0.39	-4.69	7.93	8.16	0.38	-2.34
	V_{oc} (V)	39.3	35.67	0.50	9.23	36.2	35.78	0.44	1.16
Yingli YL275D-30b	P_{max} (W)	275	243.12	8.34	11.59	200.6	200.56	7.03	0.02
	I_{sc} (A)	9.34	9.62	0.37	-2.99	7.55	7.78	0.33	-3.04
	V_{oc} (V)	38.9	34.15	0.58	12.21	35.90	34.18	0.51	4.79
HIT VBHN330SJ47	P_{max} (W)	330	315.82	9.44	4.29	247.2	253.61	9.03	-2.59
	I_{sc} (A)	6.07	6.56	0.26	-8.07	4.91	5.15	0.25	-4.89
	V_{oc} (V)	69.7	64.35	0.80	-0.51	65.1	64.76	0.63	0.52
Miasolé Flex-02 120N	P_{max} (W)	120	113.10	3.70	5.75	N/A	93.67	4.20	N/A
	I_{sc} (A)	4.53	4.57	0.17	-0.88	N/A	3.76	0.18	N/A
	V_{oc} (V)	38.1	36.10	0.55	5.24	N/A	36.13	0.24	N/A

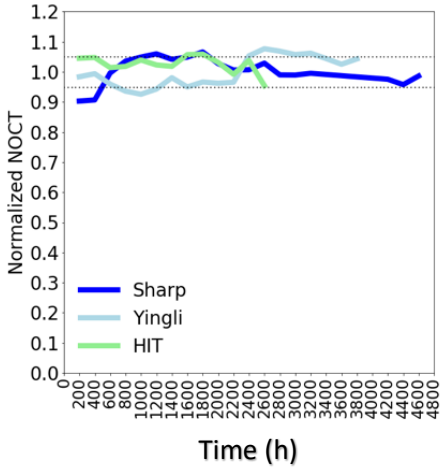

Figure 3-9. Normalized NOCT over time for commercial technologies.
The Pmax at NOCT was normalized by dividing the NOCT over time with the NOCT reported by the manufacturers. Dot lines are included as a visual guide to indicate the tolerance of ± 5%.

3.4 Evaluation of Outdoor Performance of Perovskite Devices

Outdoor performance of perovskite solar modules (PSM) and monocrystalline silicon set as reference were carried out in the city of Medellin – Colombia on the terrace of the University Research Center-SIU from the Universidad de Antioquia (60 15' 38'' N 750 34' 05''W), using the monitoring system developed in previous work (Velilla et al., 2019a) and described before, registering weather and electrical data every minute during the light-hours for 500 h to assure statistical validity of measurements. Therefore, we fabricated and encapsulated perovskite solar modules (***Figure 3-10***) considering active areas of 17, 50, and 70 cm^2 and 8 cells interconnected in series (Ramirez et al., 2019; Velilla et al., 2019b). Moreover, sensors and devices were frequently cleaned to eliminate dust issues.

Accordingly, the linearity determination criterion was applied to validate the linear relationship between P_{max} and the irradiance, represented by the high coefficient of determination (r-value) close to 1 (***Figure 3-11*****a-c),** and to minimize the influence of atypical data or data related to unclear days, shadowing, dirt, or droplets on the surface. From ***Figure 3-11*****a-c,** some principal aspects can be remarked. First, the high r-values indicated that both technologies' power delivery is a linear function of the irradiance. Second, the slopes defined as the ratio between the maximum power and irradiance represent the real outdoor ratio to transform solar power to electrical power during the exposure time involving ambient temperatures between 18 and 40 °C. Moreover, dividing these slopes by the active area of devices (the PSMs have 8 cells interconnected in series of 2.1 and 6.25 cm^2 while the silicon panel has 60 of 243.4 cm^2), it is possible to calculate an "average outdoor efficiency" of 4.76, 2.48 and 15.2 % respectively for the tested devices shown in ***Figure 3-10***. This set of results demonstrate the methodology's adaptability to evaluate and compare different solar technologies under real operating conditions. Finally, considering the best-fit data with a deviation of ±5% as the filtered data, representing the average conditions during the exposure time, the outdoor performance could be estimated, ***Figure 3-11*****d-e**, which can be normalized by dividing the filtered data by the maximum value of this data. ***Figure 3-12*** shows the results for P_{max}, I_{sc}, and V_{oc}. Hence, the plotted maps for the photovoltaic parameters as a function of temperature and irradiance allow us to graphically visualize

the device's performance in a broad range of measured atmospheric conditions during the exposure. The map's width and length of the maps correspond to the ambient temperature (ranging between 18 and 42 °C) and irradiance (ranging between 0 and 1200 W/m^2), respectively. These are representative ranges of the geographical zone.

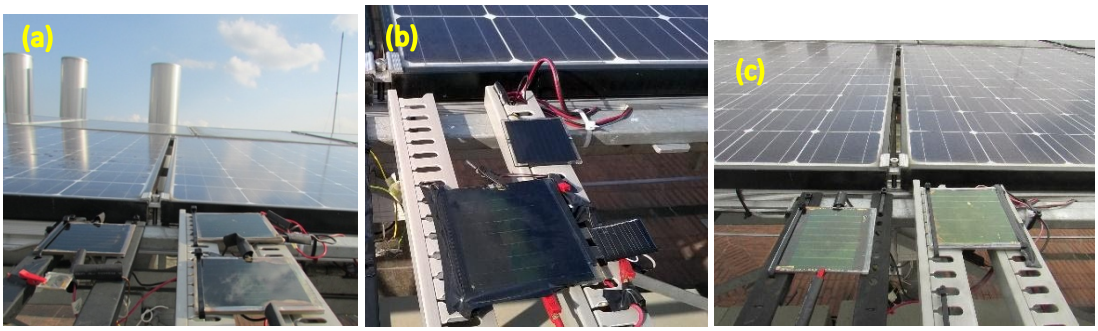

Figure 3-10. Outdoor test for the perovskite minimodules and silicon module.
a) *photo of evaluated minimodules and silicon modules at the top.* ***b)*** *photo of PSM of 17 cm^2 recently installed.* ***c)*** *photo of PSM of 50 cm^2 (left part) and PSM of 70 cm^2 (right part, which results were shown in previous work (Ramirez et al., 2019).*

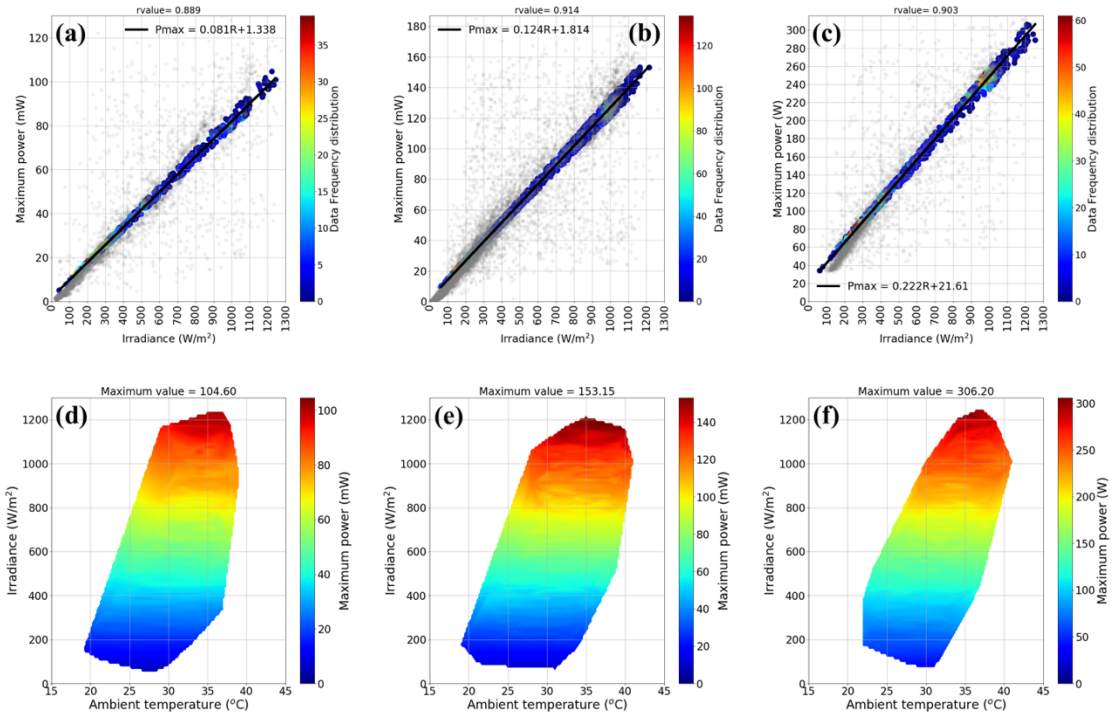

Figure 3-11. Outdoor performance for the perovskite minimodules and silicon module.
a-c) *A linearity determination criterion based on the linear behavior observed between P_{max} and the irradiance. The coefficient of determination (r-value) is shown at the top, and the fitted equation is included in the legend.* ***d-f)*** *Power delivery map as a function of irradiance and ambient temperature, the maximum value of power delivery is shown on the top of each map. The color bar indicates the variable range. Corresponding* ***a and d)*** *to perovskite minimodule of 17 cm2 of an active area.* ***b and e)*** *to perovskite minimodule of 50 cm^2 of an active area.* ***c and f)*** *to Sharp NU-RC290 (silicon monocrystalline) as reference.*

Based on the normalized contour maps behavior (***Figure 3-12***) is possible to see that P_{max} exhibited similar trends for both perovskite and silicon technologies, indicating that these variables are mainly a function of the irradiance and changes according to this variable (***Figure 3-12*****a-c)**. In terms of the normalized short circuit current, the entire contour color behavior indicates that lower I_{sc} is obtained for the case of silicon when compared to the PSMs. For instance, at an irradiance of 400 W/m^2 (blue region related to low irradiances), the normalized I_{sc} for PSM was approximately 0.4, while for the silicon panel was approximately 0.3. Moreover, the higher relative values of normalized current (higher than 0.7, orange-red region) are achieved for PSM at 800 W/m^2, while for the silicon panel, these values are achieved at 1000 W/m^2. This fact suggests that perovskite technology can produce higher relative current values in a broader range of irradiances (***Figure 3-12*****d-f).** In terms of the voltage, the V_{oc} maps show a remarkable non-homogenous distribution of this variable at the entire temperature and irradiance for the PSMs (***Figure 3-12*****g-i).**

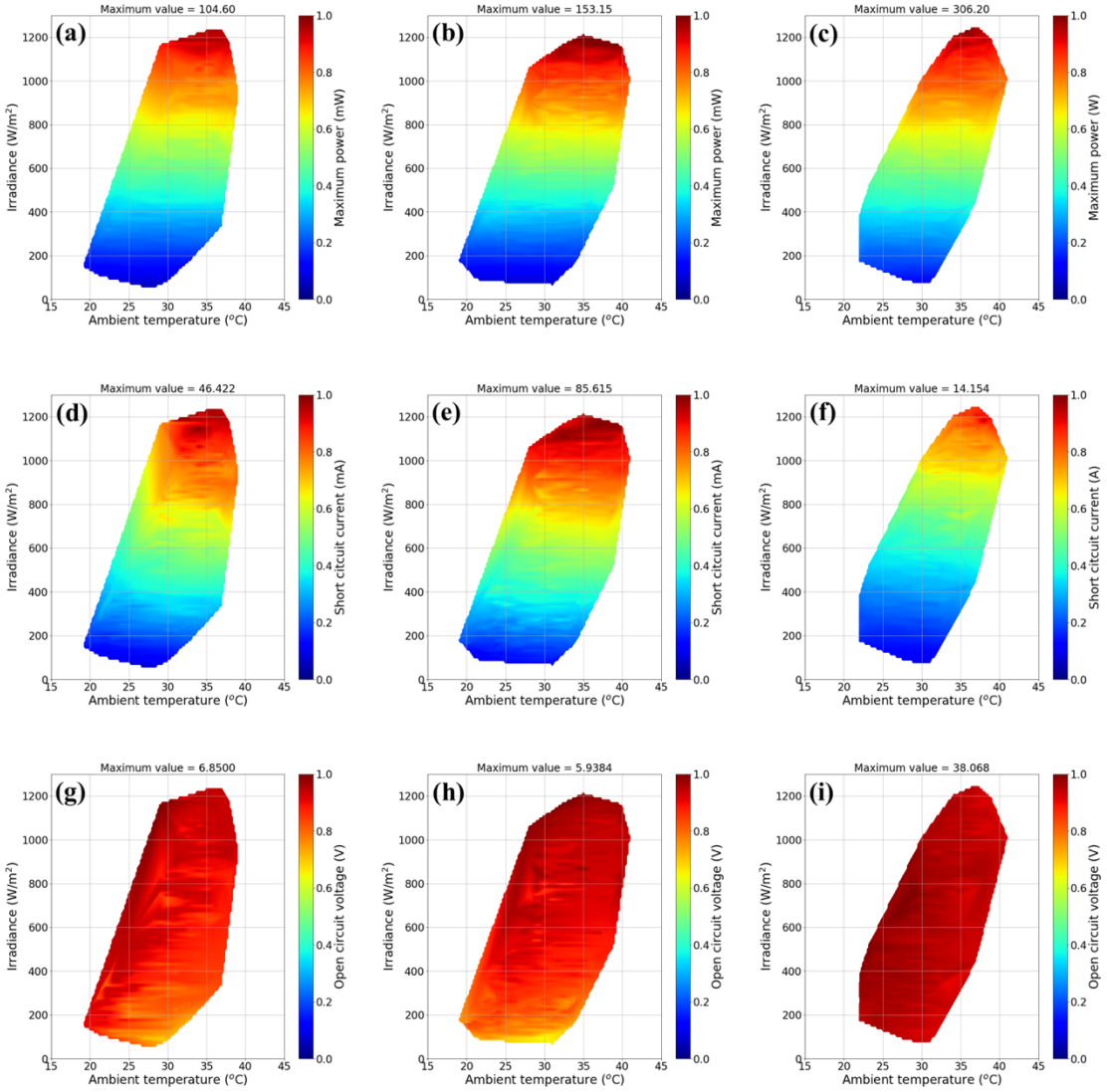

Figure 3-12. Normalized outdoor performance for the perovskite minimodules and silicon module.

*Corresponding **a-c)** to P_{max}. **d-f)** to I_{sc}. **g-i)** to V_{oc}. The color bar indicates the variable range. At the top is shows the value used to normalize the data.*

To get a thoughtful analysis of the obtained V_{oc} and identify differences between the perovskite and silicon technology, we detached the contribution of temperature and irradiance to the V_{oc} (***Figure 3-13***). From this figure, it is observed that the V_{oc} of perovskite exhibited a logarithmic dependence with irradiance as reported elsewhere for other solar cell technologies (Cowan et al., 2010). This dependence in solar cells indicated a voltage saturation that obeys a transition from monomolecular recombination at low light intensities to bimolecular recombination as the light intensity increases (Shao et al., 2014). In the case of silicon, the dependence of V_{oc} related to irradiance can be neglected based on the low r-value. Thus, an almost constant V_{oc} is observed in ***Figure 3-13***c for the irradiance range studied. Interestingly, when considering the dependence of V_{oc} with the ambient temperature (***Figure 3-13***d-f), the slopes of the linear fitted suggest that perovskite technology at outdoor exposure is affected positively by temperature (positive slope). In contrast, silicon is negatively affected as it is well known. This fact becomes more significant when the module area increases from 17 to 50 cm^2, as indicated by the coefficient of determination (0.14 to 0.722).

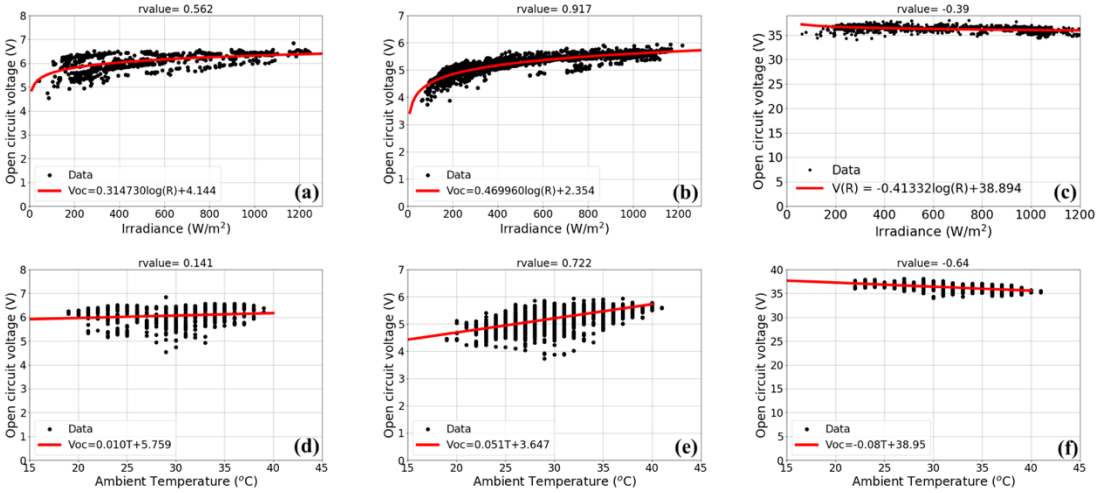

***Figure 3-13**. **Open-circuit voltage as a function of the irradiance and ambient temperature**. Corresponding **a)** to PSM of 17 cm^2. **b)** to PSM of 50 cm^2. **c)** to the silicon module.*

Figure 3-14 shows the V_{oc} dependence on the temperature at different irradiances (between 200 and 1000 W/m^2). These results suggested that the V_{oc} as a function of the temperature is linear for the silicon module in accordance with IEC-61853-1. In contrast, it is nonlinear for the perovskite module because of the slope changes at higher irradiances (800 W/m^2 for PSM 50 cm^2 and 900 W/m^2 for PSM 17 cm^2). This unusual behavior of perovskite technology can be explained in terms of lead halide perovskite materials' intrinsic properties. Through PL-temperature measurements, it has been proved an increase of the energy gap (E_g) with temperature contrary to other technologies such as Si, Ge, and GaAs. This behavior could result from the particular electron-phonon coupling in lead halide perovskites (Ramirez et al., 2018b). Due to the increase of the energy gap with the temperature and its direct relation to V_{oc}, this technology can operate at higher V_{oc} when the modules reach higher temperatures. This fact is relevant considering the limitation of current commercial silicon technology when exposed to a high-temperature environment.

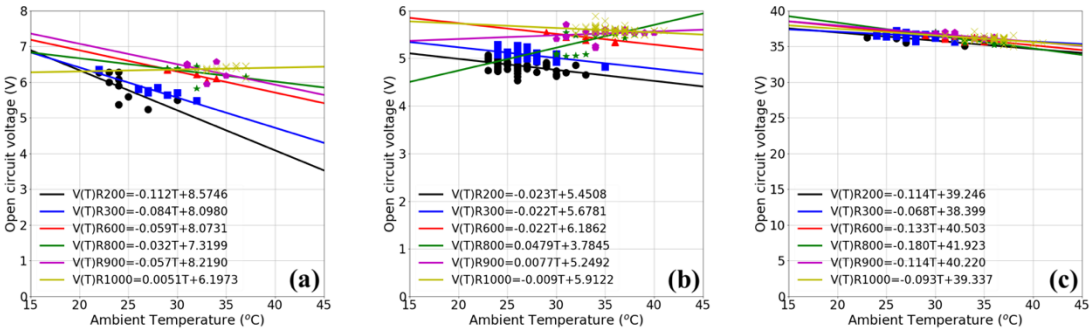

***Figure 3-14**. **Open-circuit voltage as a function of the irradiance and ambient temperature**. Corresponding **a)** to PSM of 17 cm^2. **b)** to PSM of 50 cm^2. **c)** to the silicon module. The data were filtered by irradiance levels to show the temperature effect on V_{oc}.*

3.5 Conclusions

Here, the developed monitoring system to evaluate the outdoor performance of different photovoltaic technologies, including perovskite, was fully described. Hence, the developed solar tracers were synchronized with the monitoring system to measure the I-V curve of photovoltaic modules and photovoltaic cells/minimodules. Moreover, a methodology following IEC 61853-1 was proposed and implemented to provide a complete characterization of the devices under various irradiance and temperature conditions, allowing determination of the impact of weather variables on P_{max}, V_{oc}, and I_{sc}. The impact was shown in the form of maps to improve the weather variables' visualization on performance.

The monitoring system and proposed methodology were successfully applied to commercial technologies such as silicon, HIT, and CIGs. In this way, processing the data according to the irradiance levels defined by the power rating conditions suggests by IEC 61583, it was possible to validate the datasheet's power rating conditions for the evaluated photovoltaic modules. Remarking that the NOCT was the most suitable power rating condition representing the outdoor performance, with an error within the range ± 5% for the modules evaluated during the exposure time. Hence, NOCT could be considered as the most suitable condition to check the status of the devices.

Finally, the outdoor performance shown in the form of maps allowed a comparison of this emerging perovskite technology with a well-known and optimized technology (silicon), observing similarities between photovoltaic parameters such as power delivery. Hence, higher values of the normalized short circuit current for perovskite modules were obtained when compared to the silicon modules, suggesting that perovskite technology can produce higher relative current values in a broader range of irradiances. Besides, the positive temperature dependence of the V_{oc} under high irradiance levels was also observed for perovskites minimodules. These results show for the first time that perovskite minimodules can be a robust PV technology to be used under outdoor conditions. This positive performance dependence on temperature and irradiance is a competitive fact in development of this technology.

4. Performance Evolution

This chapter analyzed the perovskite minimodules' performance evolution, degradation rate, and lifetime (T_{80}). The power loss tendencies or degradation-shape were compared with their corresponding estimated n_{ID} patterns under outdoor conditions, taking advantage of the lower correlations of performance and open-circuit voltage (V_{oc}) with temperature. Therefore, based on the linear relationship between T_{80} and the time to reach n_{ID}=2 (Tn_{ID2}), it was demonstrated that n_{ID} analysis could offer essential and complementary information with important implications for this technology's outdoor development, providing physical insight into the recombination mechanism dominating the performance. Hence, the complementarity between P_{max} and n_{ID} allowed improving the understanding of the degradation processes, device characterization, and lifetime estimation (Velilla et al., 2021).

4.1 Perovskite Degradation

Information on system state and performance collected over time is referred to as degradation data (Meeker et al., 2011). In solar devices (cells, modules, and panels), the natural indicator considered to evaluate the degradation is the performance, which is commonly obtained from the I-V curves data and contrasted to weather variables such as irradiance and temperature (IEC 61853-2, 2016). In this sense, the failure for an individual device is defined as the time at which the output power dropped to 20% below the initial output, being this the standard definition of the lifetime of photovoltaic devices (T_{80}). It depends on different factors such as materials and procedures used in the device fabrication, cell interconnects, weather conditions, seasonal variations, installation conditions, shading and soiling effects, an electrical mismatch between cells, among others (Makrides et al., 2014). This parameter is commonly obtained from the relationship between the maximum power and time in long-term analysis for devices under real outdoor operating conditions. Moreover, considering that the performance over time shows a seasonal behavior and a gradual performance loss tendency, it has been commonly fitted using statistical methods such as linear regression to estimate the degradation rate and the T_{80} (Phinikarides et al., 2014). Also, unsupervised machine learning has been employed for analyzing the time-series data and estimate the lifetime (Meyers et al., 2020).

Currently, the long-term stability or lifetime (T_{80}) of perovskite technology on average is only a few months, even for encapsulated devices, corresponding to a degradation rate higher than 100 %/year (He et al., 2020). This short lifetime is the result of intrinsic and external aspects (Boyd et al., 2019). The intrinsic degradation is mainly related to thermal and light soaking effects, while external degradation is mainly related to the ingress of water, moisture, or oxygen into the device. In a general way, the degradation effects can be observed as structural changes ($MAPbI_3$ from orthorhombic to tetragonal at a high temperature above 330 K), separation or transition phase from "black" perovskite (α-phase) into "yellow" perovskite (δ-phase). This effect is well-known as bleaching the perovskite to a yellow-white color (Domanski et al., 2018), passing before by the hydrated perovskite phase ($MA_4PbI_6{\cdot}2H_2O$) (Zhao et al., 2016). In these cases, chemical decomposition produces PbI_2 solid and the formation of NH_2CH_3, HI, NH_3, CH_3I ($MAPbI_3 \rightarrow PbI_2(s) + CH_3NH_3I$ (MAI), $CH_3NH_3I \rightarrow CH_3NH_2 + HI$) (Bisquert and Juarez-Perez, 2019; McLeod and Liu, 2018) or I_2 gases (for instance, under temperature: $MAPbI_3 \rightarrow CH_3I(g) + NH_3(g)$) (Motti et al., 2019). On the other hand, the ion migration observed in devices both with and without hysteresis (Calado et al., 2016) could be associated with structural rearrangement, incorporation of MA^+ ions or HI in the hole transporting

layer (for instance, spiro) that induces deep-level defects (Zhao et al., 2017) because MAI is very sensitive to moisture. This fact could quickly produce the release of MA^+ ions from perovskite film (Ma et al., 2017). Also, this ion migration could produce interfacial charge accumulation or redox reactions between metal contacts and iodide, fact observed for silver and aluminum electrodes (Grancini et al., 2017). This metal contacts' chemical degradation is characterized by the I-V curve's S-shape, highlighting that noble metals as Au also lead to corrosion (Guerrero et al., 2016b). Furthermore, it has been shown that the illumination-induced degradation in the case of NiO_x used as the hole transport layer, being the defects of this layer correlated to the interstitial oxygen or N_i^{2+} vacancies that occur as results of the creation of Ni^{3+} ($2NiO \rightarrow 2Ni^{3+}+Ni_v+2O^{2-}$) (Islam et al., 2017). These defects or deep traps sites act as sinks for electrons, with recombination of the trapped electrons occurring directly with the holes in the perovskite or the transporter layer (Wojciechowski et al., 2015).

Accordingly, it is possible to find different mechanisms to improve the lifetime, including the encapsulation process/method, kind of perovskite (2D, 3D, Etc.), selective charge contacts or other layers involved (Heo et al., 2019), passivation of the interfaces (Yang et al., 2020) or the grain boundaries (Zhang et al., 2020). Nevertheless, because the degradation is a complex process that depends on the structure (layers) and their interfaces, the degradation studies must be conducted in the complete device and not in isolated layers (Liu et al., 2020). Therefore, in this section, only encapsulated minimodules with an inverted structure were evaluated.

4.2 Outdoor Test

To evaluate the perovskite minimodules' outdoor performance evolution, weather variables such as irradiance and ambient temperature (T) as well as the devices' I-V curves were registered and stored every minute during daylight hours (5:30 AM to 6:30 PM) using a previously developed monitoring system (Velilla et al., 2019a). To ensure a complete I-V curve, V_{oc} was measured and recorded before the measurement. Subsequently, the curve was scanned between -0.5 V and $1.1 \cdot V_{oc}$ in the forward direction. After the scanning, the I-V tracer was disconnected, and the device was in the open-circuit condition.

The collected high-throughput data were processed following the flowchart shown in ***Figure 3-4***. In brief, from the I-V curves, photovoltaic parameters such as V_{oc}, the short-circuit current (I_{sc}), the fill factor (FF), the photoconversion efficiency, and P_{max} were extracted. The irradiances and ambient temperatures were also recorded during the I-V measurement (synchronously). Subsequently, the raw data were filtered based on the linearity determination criterion to minimize transient effects related to changes in irradiance, shadowing caused by clouds or droplets, or atypical data (Velilla et al., 2019b). Hence, the best-fit data with a deviation of ±5% were selected as the filtered data, representing the average conditions of the time window.

Moreover, the power loss tendency or degradation shape was obtained by calculating the OP observed in the measurement sets, each of which contained measurements recorded over 100 hours of outdoor exposure. The data in each set were filtered considering a deviation of 5% from the irradiance levels corresponding to the power rating conditions (PRCs) indicated by IEC 61853-1 (IEC 61853-1, 2011). That is, 1000 W/m^2 corresponds to standard test conditions (STC); 800 W/m^2 corresponds to NOCT conditions; 500 W/m^2 corresponds to low-temperature conditions (LTC); and 200 W/m^2 corresponds to low-irradiance conditions (LIC). The variables were recorded every minute during daylight hours, and the time considered to obtain the average OP was slightly longer than four days (100 h). This

time is long enough to consider the data recorded in each set to be statistically valid, allowing reliable average values for tracking the performance evolution.

Accordingly, ***Figure 4-1*** shows some photos of the perovskite minimodules exposed to natural sunlight, without a tracker, in the facilities of the Solar Cell Outdoor Performance Laboratory of the University of Antioquia (OPSUA) in Medellín, Colombia, during January-June 2019. The photos highlight physical changes observed for the evaluation of approximately 40 minimodules during January and June of 2019.

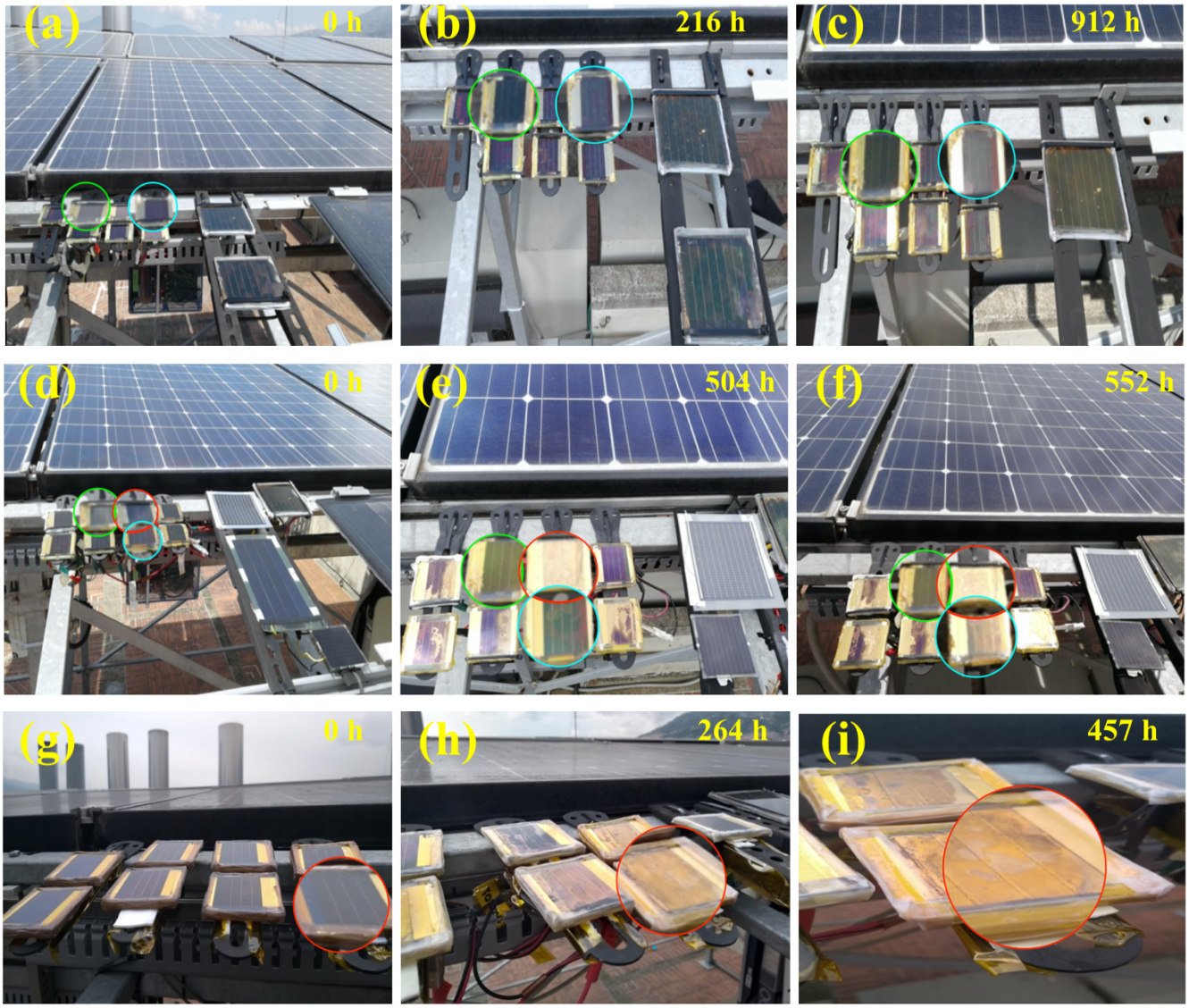

Figure 4-1. Installation of perovskite minimodules for the outdoor test.
a-i) *Photos of installed minimodules. These were located close to other solar technologies studied for independent works.* ***a-c)*** *corresponding to some samples of the same batch during the first 912 h of exposure.* ***d-f)*** *corresponding to some samples of another batch during the first 552 h of exposure.* ***g-i)*** *corresponding to samples that rapidly degraded. Some samples are highlighted with blue, green, and red circles to show physical changes observed during the test.*

4.3 P_{max} Patterns

Figure 4-2 shows a summary of P_{max} evolution for the minimodules evaluated under outdoor conditions following the procedure proposed in the last chapter (***Figure 3-4***). The NOCT conditions were selected because it is defined as the equilibrium mean solar cell junction temperature of the module in the describe environment (IEC 61215, 2003), these conditions reflecting adequately the real operating, indicating how the module temperature is affected by solar irradiation, ambient temperature and thermal properties of the photovoltaic material (Makrides et al., 2012), these conditions are included on the datasheets for commercial solar modules, and NOCT can be reached outdoors (Velilla et al., 2019a).

In this context, the evaluated outdoor samples exhibited three different P_{max} evolution patterns over time, named convex, linear, and concave patterns, because of the shapes they exhibit, ***Figure 4-2***a. These three distinctive patterns are commonly described for degradation processes in the literature to study possible degradation paths and estimate the failure time (Meeker et al., 2011). Therefore, these P_{max} behaviors were fitting to linear models to estimate the degradation rate and T_{80}. In this way, the T_{80} values for the evaluated samples were analyzed in ***Figure 4-2***b in a probability distribution plot. This plot indicates that the double Weibull distribution is more suitable to represent the data distribution with a shape parameter of c=0.6, suggesting higher mortality early of devices and that the failure rate decreases over time. Also, this plot shows three groups, one related to T_{80} lower than 200 h, another related to T_{80} between 380 and 700 h, and the last one related to T_{80} higher than 1250 h. These groups agree with the degradation shape of concave, linear, and convex patterns, respectively. Therefore, all the analyzed minimodules present behavior that can be statistically associated with these three patterns. Finally, ***Figure 4-2***c highlights the behavior of one representative sample of each pattern, corresponding to the lower degradation rate of the initial P_{max} of 0.29 %/day to the convex pattern, a moderate degradation rate of 1.39 %/day to the linear pattern, and faster degradation rate of 7.68 %/day to the concave pattern.

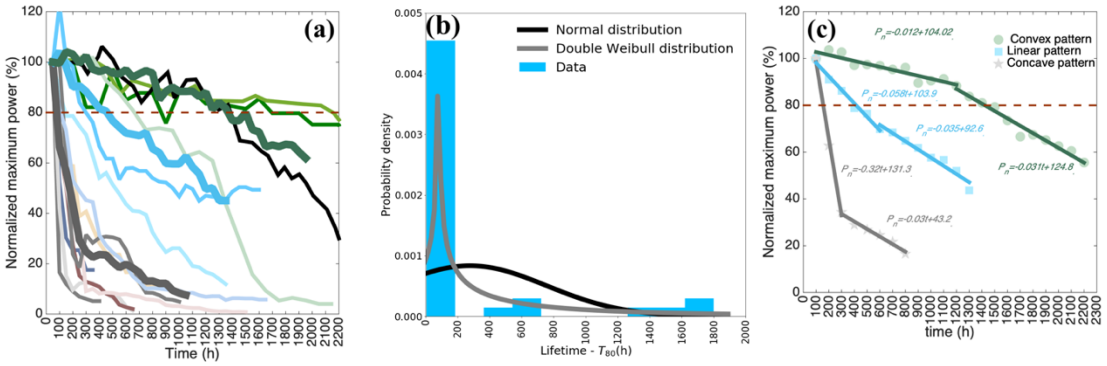

Figure 4-2. Summary of P_{max} evolution from the outdoor test.

a) *representative power loss tendencies for perovskite minimodules evaluated outdoor at NOCT, highlighting the three cases considered representative with thicker lines.* ***b)*** *Probability density of T_{80} for samples evaluated to outdoor test, considering the failure time as the first time at which the power drop 20%. Corresponding the blue bars to T_{80} data, black line to data fit to Normal Distribution function (being the parameters: μ=276.8 and std=478) and green line to data fit to Double Weibull Distribution function (being the parameters: c=0.6, loc=80 and scale=453.7). This result suggested 3 degradation levels based on the likelihood of T_{80} values. The first was related to faster degradation (T_{80} < 200 h) and the most likely, the second related to moderate degradation (350 < T_{80} <700 h), and the third related to lower degradation (T_{80} > 1250 h). These levels could be mainly attributed to the minimodules' manual encapsulation goodness that allowed the moisture or water income.* ***c)*** *Degradation Rate (DR) of three representative patterns of each*

group according to degradation levels suggested by the probability function distribution of T_{80}. Corresponding the DR to the slope of linear fitting showed (color lines). The slope of the fitted curves provides the degradation rate in %/h units.

Accordingly, ***Figure 4-3*** shows in the form of boxplots the P_{max} evolution of the three representative samples of each pattern at STC, NOCT, low irradiance, and low temperature conditions. In these cases, similar behaviors are observed for all evaluated power rating conditions related to each pattern, allowing validation of the pattern exhibited. In this way, these three P_{max} patterns have all been previously observed for PSCs (He et al., 2020). For instance, the convex pattern has been observed for encapsulated PSCs stored at room temperature, for which the P_{max} loss was attributed to interface deterioration inducing interfacial recombination, along with perovskite layer degradation related to the formation of deeper defect states (Khadka et al., 2018). The linear and convex patterns have both previously been observed in nonencapsulated cells under controlled relative humidity conditions, depending on the PbI_2/MAI ratio (Ma et al., 2017), while the concave pattern has been observed in encapsulated cells exposed to different levels of sunlight, suggesting that light intensity is the main variable that accelerates the degradation process (Anoop et al., 2020). Moreover, this shape has also been observed in nonencapsulated PSCs under different atmospheres and light intensities, with faster degradation under higher relative humidity (Domanski et al., 2018), and in nonencapsulated devices tested under air exposure, suggesting an increase in electrical traps due to ion migration from the perovskite layer to other layers as the main reason for the degradation (Lee et al., 2019). In these cases, the controlled atmospheres enabled correlation with the physical origins of the degradation, whereas under outdoor conditions, because various factors may be involved in the degradation process, determining the physical origin of the degradation is not always possible.

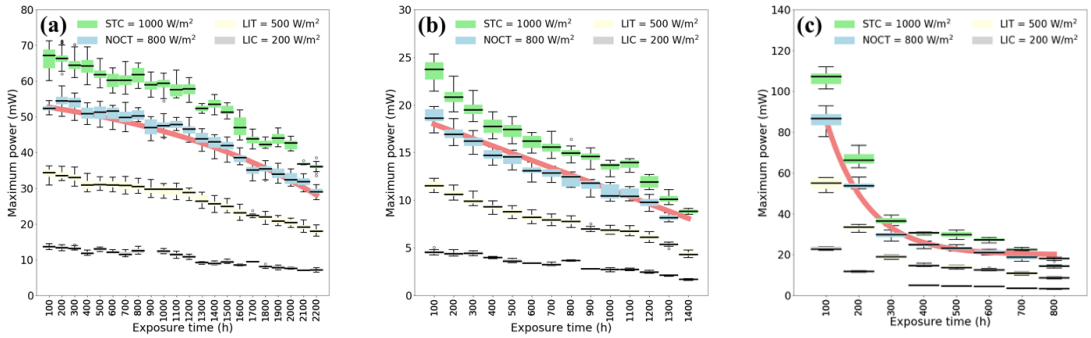

Figure 4-3. Degradation patterns in the maximum power.

a-c) *Maximum power under different power rating conditions suggested by IEC 61863 for the convex, linear, and concave patterns. Green boxes correspond to 1000 W/m² (STC), blue boxes correspond to 800 W/m² (NOCT), yellow boxes correspond to 500 W/m² (low-temperature condition), and gray boxes correspond to 200 W/m² (low-irradiance condition) for the* ***(a)*** *convex,* ***(b)*** *linear and* ***(c)*** *concave degradation behaviors. The thick black line on each box represents the average performance in the corresponding time window. The red line is included as a visual guide to illustrate the shapes related to the convex, linear, and concave patterns.*

Intended to obtain more information related to the P_{max} patterns, ***Figure 4-4*** shows in the form of contour the first 100 h of exposure for the main photovoltaic parameters extracted from the I-V curve. The corresponding maps show the average impact of weather variables on P_{max}, V_{oc}, and I_{sc} over a broad set of T values and irradiances, ranging between 18 and 42 °C and up to 1200 W/m², respectively. These ranges correspond to the most representative values of the weather variables and performances recorded during the time window considered. This figure allows us to identify some

trends, such as the low-temperature dependence of V_{oc}, which was identified as a competitive advantage of perovskite in the last chapter and remarked in (Velilla et al., 2019b). In this regard, the data related to the convex pattern (***Figure 4-4*****a,d,g**) and the linear pattern (***Figure 4-4*****b,e,h**) follow the expected trend, with P_{max}, I_{sc}, and V_{oc} increasing with increasing irradiance but showing only a low sensitivity to temperature. In contrast, concave pattern sample data do not exhibit this monotonic variation, instead of showing local maxima or minima at various irradiance levels and temperatures (***Figure 4-4*****c,f,i**). Moreover, when a lower total sampling time of 50 h is considered, the T_{80} of this sample is estimated to be 80 h (see ***Figure 4-5***), indicating that during the first 100 h of exposure, fast degradation occurs, causing the nonmonotonic behavior depicted in ***Figure 4-4*****c,f,i**. Also, based on ***Figure 4-2***c, it is observed that the sample with the concave shape degrades faster (T_{80}=80 h) than the sample with the linear pattern (T_{80}=414.2 h), while the one with the convex pattern shows the slowest degradation rate (T_{80}=1442.2 h).

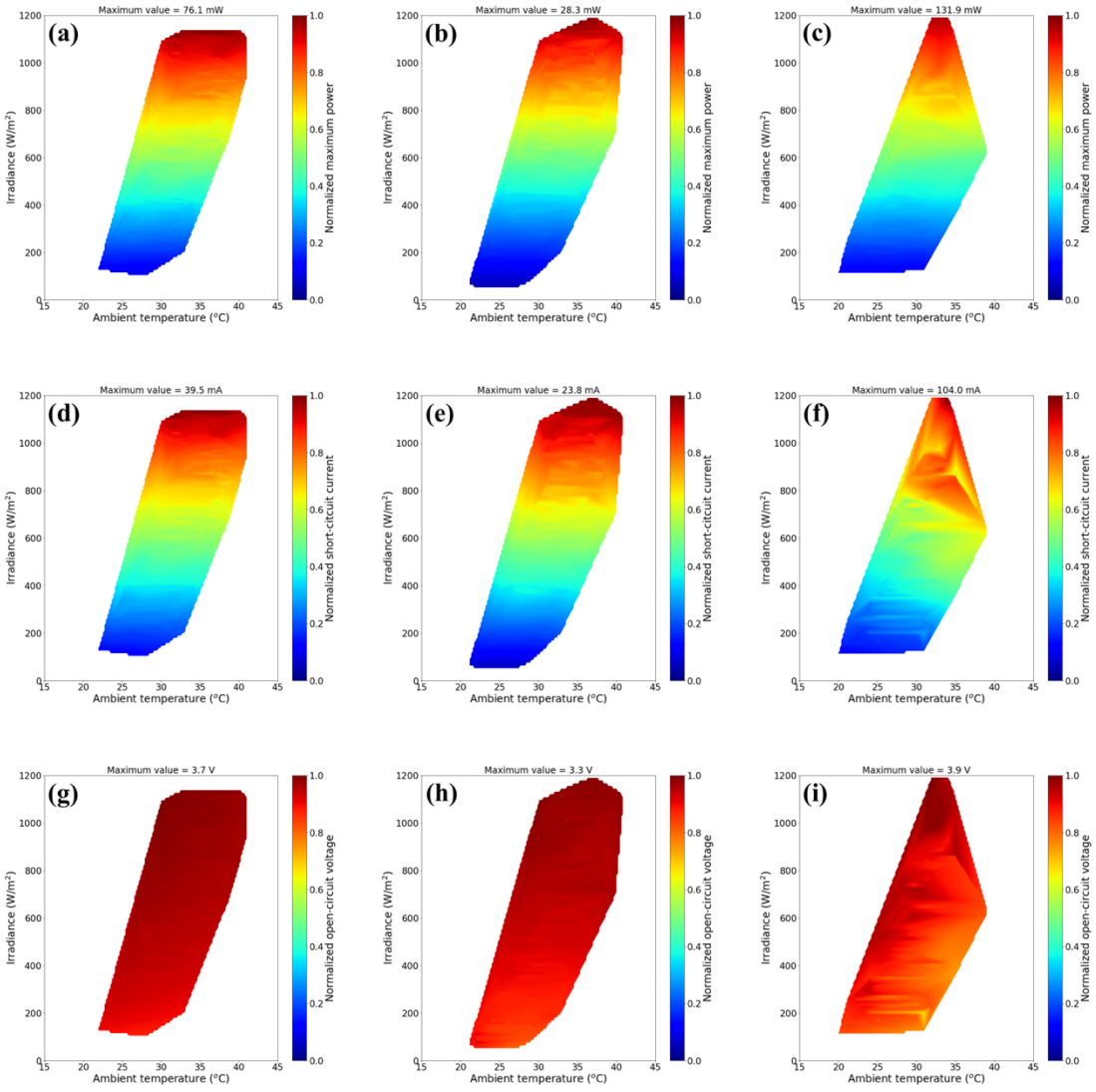

Figure 4-4. Normalized outdoor performance of the three representative samples.
a-c) *Maximum power; these data are also used to calculate the first point values for 100 h of exposition time plotted in* ***Figure 4-3a-c****.* ***d-f)*** *Short-circuit current.* ***g-i)*** *Open-circuit voltage. Panels* ***(a)****,* ***(d),*** *and* ***(g)***

*correspond to a device with a convex P_{max} shape, according to **Figure 4-3a**. Panels **(b)**, **(e)**, and **(h)** correspond to a device with a linear P_{max} shape, according to **Figure 4-3b**. Finally, panels **(c)**, **(f)**, and **(i)** correspond to a device with a concave P_{max} shape, according to **Figure 4-3c**. The color bar indicates the variable range. At the top of each plot, the maximum recorded value used to normalize each variable's data is shown. These figures only considered the data during the first 100 h of exposure.*

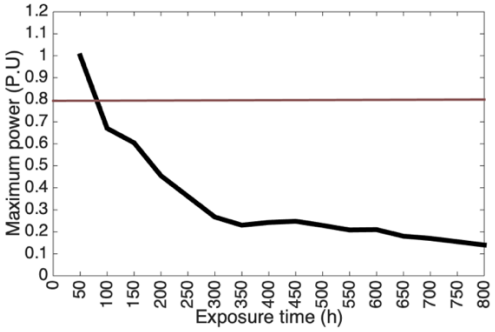

Figure 4-5. Concave P_{max} pattern.

P_{max} at NOCT considering a sampling time of 50 h. The solid red line corresponds to a 20% loss of power and is used to calculate T_{80}. Hence, the estimated T_{80} is 80 h.

In this context, the degradation in P_{max} can be mainly attributed to the decreases in V_{oc} and I_{sc} for the convex and linear patterns, respectively. In contrast, both parameters are significantly degraded for the concave pattern, as is shown in ***Figure 4-6*** and ***Figure 4-7***. These trends can be observed in a proper way normalizing the variables extracted from the I-V curve (***Figure 4-7***) concerning the initial values (***Figure 4-6***a-c), in order to fit their behaviors to linear regression models and estimate the degradation rates (DR) by sections (***Figure 4-6***d-f). Therefore, it is possible to observe some features:

a) Related to P_{max} convex pattern, this variable, and the V_{oc} can be modeled by 2 linear models, corresponding the DR value for the second section to 2 times first section's value for both variables. In contrast, the I_{sc} can be modeled by only one linear model characterized by a DR value of 0.0023 %/h. These results indicated that the main power drop is because of the changes in V_{oc}.
b) Related to P_{max} linear pattern, this variable, and the V_{oc} can be modeled by 2 linear models. Nevertheless, the corresponding DR value for the second section for P_{max} is lower than the DR value of the first section (0.035 and 0.058 %/h, respectively). For V_{oc}, the DR for the second section is 16 times the first section's value (0.035 and 0.0022 %/h, respectively). I_{sc} can be modeled by only one linear model characterized by a DR value of 0.0029 %/h. These results indicated that the main power drop is because of the changes in I_{sc}.
c) Related to P_{max} concave pattern, all variables can be modeled by 2 linear models, corresponding the second section's DR values to the lower DR values for each variable. Moreover, in the first section, similar DR values for V_{oc} and I_{sc} were obtained. These results indicated that the power drop is because of both variables' changes (I_{sc} and V_{oc}).
d) Accordingly, P_{max} convex and linear patterns share similar trends, characterized by constant DR for I_{sc}, indicating a constant reduction in the charge extraction. Also, both V_{oc} patterns shown a double increase in the DR after a specific time (1400 and 1000 h for convex and linear patterns). This fact could be associated with surface traps allowing the charge recombination, increasing the device's series resistance, and causing the voltage drop.

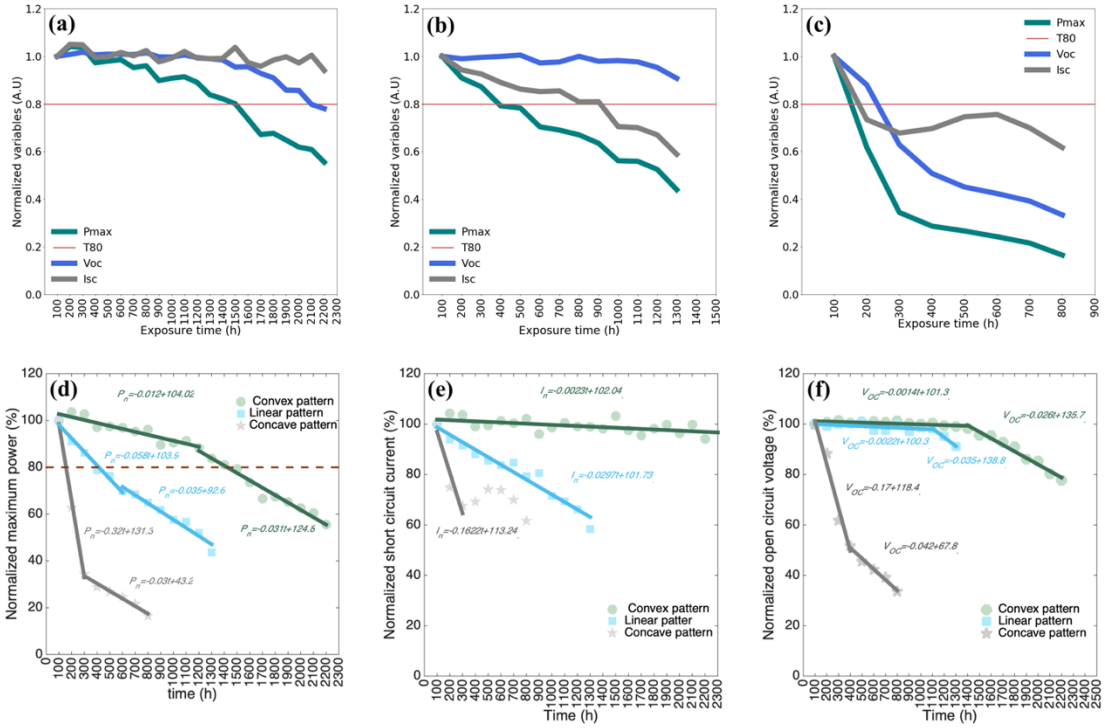

Figure 4-6. Normalized behavior for photovoltaic parameters.

Corresponding ***a)*** *for variables related to P_{max} convex pattern,* ***b)*** *for P_{max} linear pattern, and* ***c)*** *for P_{max} concave pattern.* ***d)*** *Maximum power for all patterns.* ***e)*** *I_{sc} for all patterns and* ***f)*** *V_{oc} for all patterns. The green color corresponds to P_{max} convex pattern, the blue color corresponds to P_{max} linear pattern, and the gray color corresponds to P_{max} concave pattern. Solid lines correspond to the fits and color markets to the data. The variables were normalized concerning each variable's initial value shown in* ***Figure 4-7****.*

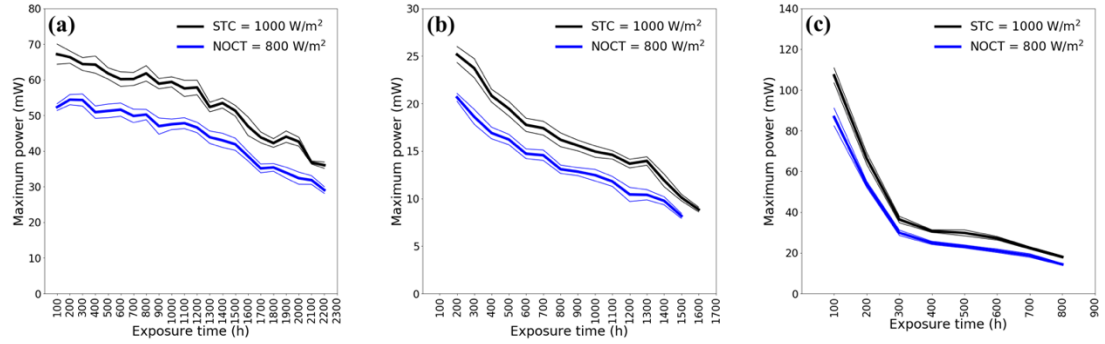

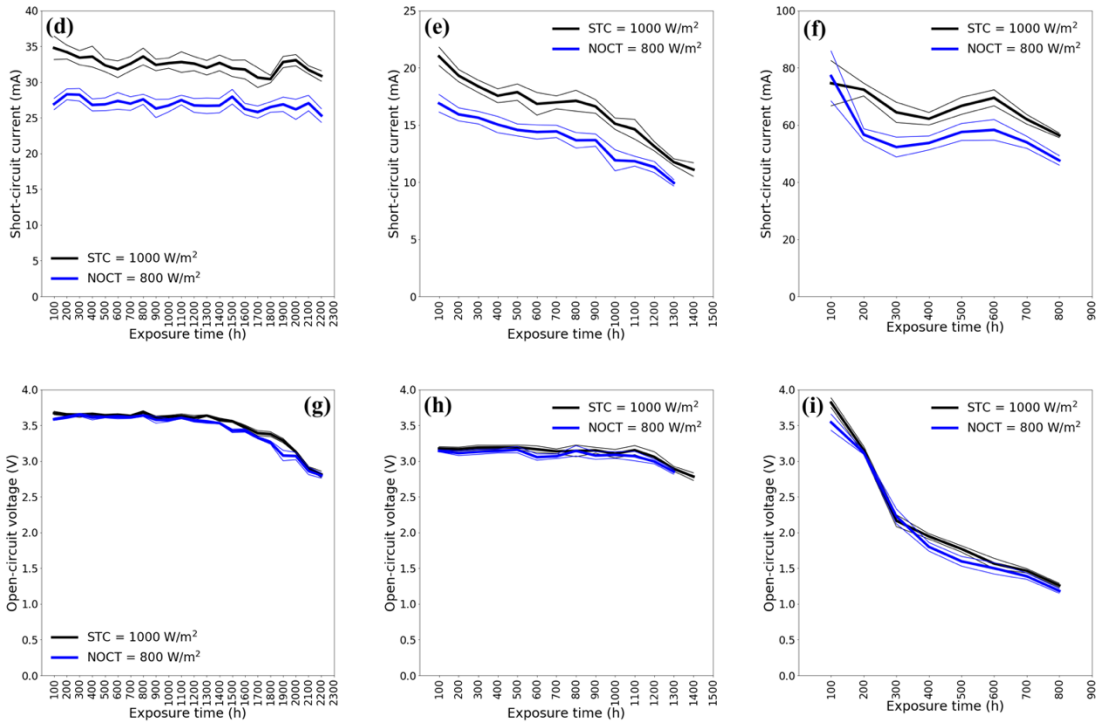

Figure 4-7. Outdoor performance for photovoltaic parameters.

*Corresponding **a-c)** for P_{max}, **d-f)** for I_{sc}, and **e-g)** for V_{oc}. **a,c, and g)** for convex pattern, **b,e and h)** for linear pattern and **c,f, and i)** for concave pattern. Black lines are related to STC and blue lines to NOCT. Thick lines correspond to the mean values of variables, while the thin lines correspond to the standard deviation of the variables in the window time.*

4.4 Ideality Factor Patterns

The outdoor data related to the three representative samples correlated to each P_{max} pattern (***Figure 4-3***) were analyzed following the methodology explained in the chapter 2 related to the ideality factor. Therefore, the average n_{ID} values were calculated using **Equation 5**, considering different measurements of V_{oc} recorded at different irradiance levels in every 100 hours of the high-throughput data under the flowchart ***Figure 3-4***, taking advantage of the different levels of illumination caused by day-night cycles to collect a large amount of data across a broad range of illumination conditions.

Figure 4-8 shows as an example the procedure to estimate the n_{ID} using the data for the sample with P_{max} convex pattern during the first 100 h of exposure. The raw data (full data during the first 100 h) are filtered, applying a linearity determination criterion to minimize the influence of atypical data or data related to unclear days, shadowing, dirt, or droplets on the surface. In this regard, the best-fit data with a deviation of $\pm$ 5% are selected as the filtered data, representing the average conditions during the exposure time,

Figure 4-8**a**. Then, the data are filtered by the ambient temperature to extract the V_{oc} and irradiance values correlated to this temperature. These V_{oc} and irradiance values are used in accordance with the **Equation 5** to estimate the n_{ID} values,

Figure 4-8**b**. Accordingly, to consider the deviations from the average value due to temperature changes, n_{ID} values are estimated by calculating this parameter in the measurement sets, filtering the

data by temperatures between 25 and 37 °C in steps of 2 °C with a deviation of ±1 °C. Then the mean value of each dataset is considered as the average n_{ID} value. The results during the exposure time for the representative samples are shown in ***Figure 4-9*** in the form of boxplots to illustrate the deviations from the average value and data distribution for the samples analyzed.

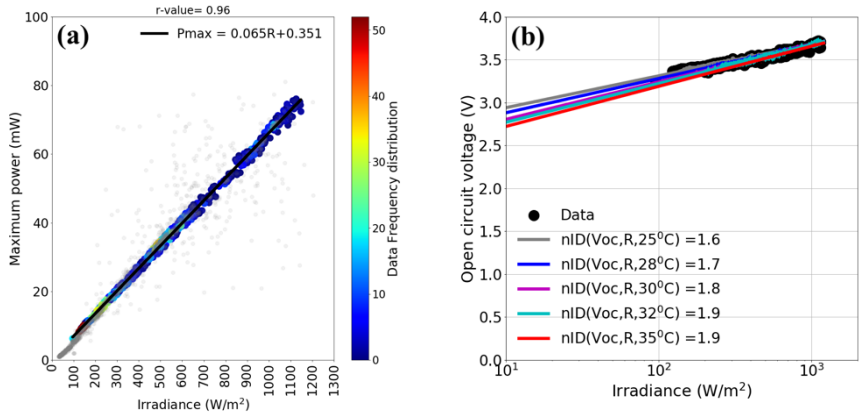

Figure 4-8. Procedure to estimate n_{ID} from Outdoor Data.

a) *Linearity determination criteria to filter the data from atypical data, related to unclear days, dirty or drop on the surface. At the top is shown the coefficient of determination (r-value), estimated from the fitting process between P_{max} and irradiance. This value is close to 1, indicating a linear behavior between variables. The gray points correspond to data measured in the exposure time considered, and the color dots correspond to data considered as filtered and representative of the dataset. In this case, the filtered data correspond to the average conditions during the 100 h of exposure.* ***b)*** *Ideality factor estimated considering different ambient temperatures and the data registered between 0 and 100 h of exposure. The parameters estimation of n_{ID} for the linear regression in accordance with* ***Equation 5*** *is shown in* ***Table 4-1****.*

Table 4-1. *Parameters related to the fit of V_{oc} and Irradiance to estimate n_{ID}.*

Temperature (^{0}C)	n_{ID}	r-value	Slope	Intercept
25	1.58	0.98	0.16	2.57
28	1.67	0.98	0.17	2.48
30	1.81	0.99	0.18	2.37
32	1.86	0.99	0.19	2.32
35	1.91	0.97	0.20	2.25

The n_{ID} results showed in ***Figure 4-9*** also exhibits three distinct evolution patterns or shapes. Precisely, a convex P_{max} evolution pattern corresponds to a concave n_{ID} evolution pattern (***Figure 4-9*****a**) and *vice versa* (***Figure 4-9*****c**). In contrast, for a linear P_{max} pattern, a linear n_{ID} pattern is observed (***Figure 4-9*****b**). In the cases of convex P_{max}/concave n_{ID} patterns (***Figure 4-3*****a** and ***Figure 4-9*****a**) and linear patterns (***Figure 4-3*****b** and ***Figure 4-9*****b**), at times earlier than T_{80} (1442.2 and 414.2 h, respectively), n_{ID} takes values between 1 and 2, indicating bulk Shockley-Read-Hall (SRH) recombination (Tress et al., 2018). It is a characteristic of most PSCs as this result was obtained from fresh devices characterized under indoor conditions in chapter one (***Figure 4-11***). For longer times, n_{ID} exhibits values above 2, characteristic of a multiple-trap distribution, originating from the formation of trap states, causing the performance degradation, as pointed out by Khadka et al.

(Khadka et al., 2018). In concave P_{max}/convex n_{ID} patterns (***Figure 4-3*c** and ***Figure 4-9*c**), the initial values of n_{ID} are higher than 2, indicating fast degradation in the first 100 h of exposure due to the formation of multiple trap states. Interestingly, after the initial increase in n_{ID}, a progressive decrease is observed in the concave (***Figure 4-9*c**) and convex (***Figure 4-9*c**) cases, suggesting evolution from bulk recombination to interfacial recombination. This behavior does not imply a recovery in device performance; it only indicates a transition between two different recombination regimes in the degradation process, from multiple-trap recombination to a regime with higher interfacial recombination.

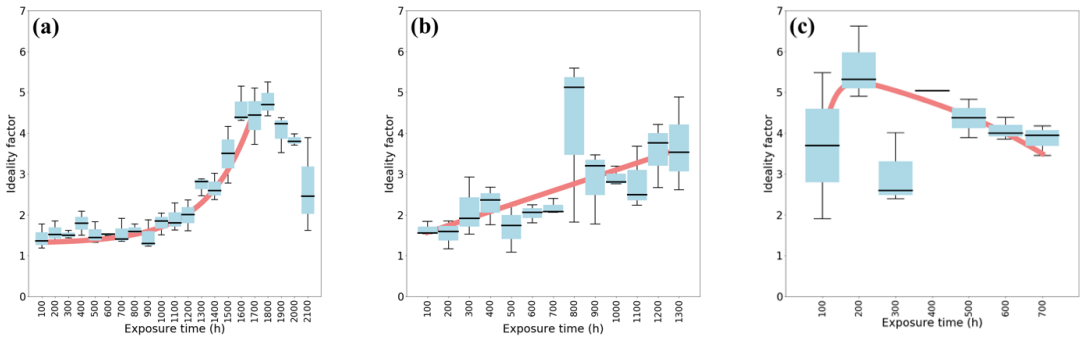

Figure 4-9. Patterns of the ideality factor.

***a-c)** Ideality factor analysis of the three samples: **(a)** n_{ID} exhibits a concave pattern for samples exhibiting a convex P_{max} pattern, **(b)** n_{ID} exhibits a linear pattern for samples exhibiting a linear P_{max} pattern, and **(c)** n_{ID} exhibits a convex pattern for samples exhibiting a concave P_{max} pattern. The average n_{ID} was calculated using all data points recorded during each 100 h period. The boxplots were estimated by calculating n_{ID}, filtering the data by T between 25 and 37 °C in steps of 2 °C with a deviation of ±1 °C, and obtaining the maximum and minimum n_{ID} to define the upper and lower bars, respectively. The thick black line on each box represents the average performance in the corresponding time window. The red line is included data as a visual guide to illustrate the shapes related to the convex, linear, and concave patterns.*

It is worth noting that results in ***Figure 4-9*** were estimated in accordance with **Equation 5** using the ambient temperature to simplify the methodology and the number of variables to record in the outdoor test. Nevertheless, to determine the impact of the device temperature in the estimation of the ideality factor, the data related to P_{max} convex pattern were used to estimate this parameter. In this sense, ***Figure 4-10*a** shows the relationship between ambient and device temperature, which depicted a linear behavior characterized by the figure's inset equation and demonstrated by the r-value close to 1 shown at the top. ***Figure 4-10*b** shows the results of calculating the n_{ID} using the device temperature. This behavior is very similar to the n_{ID} behavior obtained in ***Figure 4-9*a** using the ambient temperature. Therefore, to compare in a better way both behaviors, ***Figure 4-10*c** shows the average values and standard deviation of the variable in the measurements sets, which contain the data over 100 h of exposure. Hence, the error between both estimations was 4.3%, which was calculated using the Euclidean norm between the difference of both estimations. Consequently, it was possible to validate that using the ambient temperature instead of device temperature allowed us to estimate reliable values to track the evolution (because this estimation introduces a relative error lower than 5%) and simplifies the number of outdoor variables.

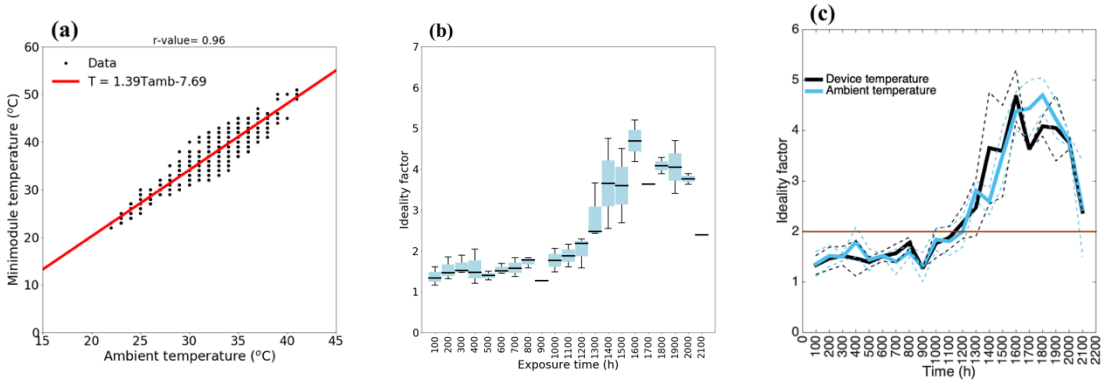

Figure 4-10. Estimated ideality factor using the device temperature.

a) *Relationship between ambient and minimodule temperature during the first 100 h of exposure. Corresponding the points to measured data and the solid red line to the linear regression fit. The corresponding coefficient of determination of the fits is shown at the top.* ***b)*** *Ideality factor calculated considering the device temperature instead of the ambient temperature. The boxplots were obtained by calculating the variables observed in the measurement sets, each of which contained measurements recorded over 100 hours of outdoor exposure. The thick black line on each box represents the median value, while the blue boxes represent 50 % of the data in the corresponding time window.* ***c)*** *Comparison of ideality factor calculated using the device and ambient temperature. Solid lines of each color correspond to the estimated average n_{ID} values and dotted lines to the standard deviation of the variables. These values were estimated by calculating the n_{ID} values in the corresponding time window for ambient temperatures ranging between 25 and 35 ^{0}C and device temperature between 25 and 45 ^{0}C in steps of 2 °C.*

Accordingly, two methods used for n_{ID} determination have been verified through indoor measurements in chapter one, ***Figure 2-24-Figure 2-27***. In this way, considering the excellent agreement with the n_{ID} values calculated with the implemented procedure, two representative samples of minimodules were analyzed following procedure shown in ***Figure 2-24***. ***Figure 4-11*****a** shows the n_{ID} calculated from the V_{oc} fitting at different light intensities using **Equation 5**, which is close to 1.6 by the new device and higher than 3 for the degraded device. ***Figure 4-11*****b** shows the impedance spectrum at various light intensities for both devices (fresh and degraded), which were fitted to the equivalent circuit to extract the R_{rec} and calculated the n_{ID} in accordance with **Equation 6,** considering negligible transport and charge transfer resistances in both the bulk and the contact layers and at interfaces (Yoo et al., 2019). Hence, n_{ID} value can be calculated from the slope of the logarithmic plot of R_{rec} *vs.* V_{oc}, estimating a value close to 1.5 by the new device and 3.4 for the degraded device, ***Figure 4-11*****c**. Here, both methodologies' estimated values show similar results, validating the procedure, allowing us to observe that the degraded device shows surface recombination based on the higher n_{ID} value, while the fresh device is characterized by SHR recombination in bulk.

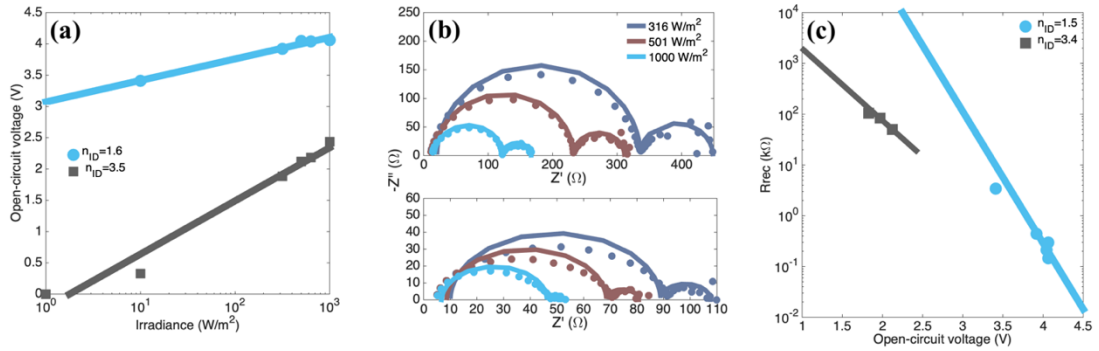

***Figure 4-11**. **Ideality factor under indoor conditions for minimodules**.*
***a)** Calculation of n_{ID} from the relationship between the open-circuit voltage and the irradiance level, where the solid lines correspond to fits in accordance with **Equation 5**. These data indicate that an n_{ID} = 1.6 for the new device and 3.5 for the degraded device. **b)** Nyquist diagrams of impedance at different light intensities (experimental data, plotted as dots) and their corresponding fits (plotted as solid lines) for the new device (upper plot) and for the degraded device (lower plot). The fits correspond to the best solutions obtained using a genetic algorithm combined with the simplex method to minimize the error between the experimental data and the circuit model according to **Equation 1**. **c)** Calculation of n_{ID} from the relationship between R_{rec} and V_{oc} using **Equation 6**. The linear regression fits indicate that n_{ID} = 1.5 for the fresh or new device and 3.4 for the degraded device. The measurements were carried out at room temperature (25°C).*

4.5 Complementary Analysis between P_{max} and n_{ID} Patterns

A complementary analysis to the P_{max} methodology can be performed by considering the average n_{ID} values over time. Hence, we normalized the average P_{max} under NOCT conditions concerning the average value obtained for each sample during the first 100 hours of outdoor exposure in order to estimate the T_{80} (***Figure 4-2*****c** and ***Figure 4-6***). This result is shown in ***Figure 4-12***, and by defining Tn_{ID2} as the time in which the value of n_{ID} first reaches 2, it is possible to observe that for times longer than T_{80} (***Figure 4-12*****a**), n_{ID} exhibits values higher than 2 (***Figure 4-12*****b**). Accordingly, ***Figure 4-12*****c** analyzes the relation between Tn_{ID2} and T_{80}, showing a strong linear relationship. This linear relationship indicates that these parameters are correlated and complementary probes of the degradation processes occurring in the devices. T_{80} provides valuable commercial information and a clear idea of a fundamental property of a photovoltaic module, namely, its lifetime, which is a key concern for the customer.

On the other hand, Tn_{ID2} has a physical meaning related to the transition point from bulk SRH recombination through a single level to recombination through multiple levels as a result of device degradation (Tress et al., 2018). The linear relationship between these parameters indicates that the degradation processes causing the reduction in device performance, as monitored by T_{80}, manifest as a change in the recombination mechanism, as tracked by T_{nID2}. Accordingly, the complementarity shown in ***Figure 4-12*** between these two parameters allows us to correlate the commercial parameter with a parameter that has physical meaning. This fact has important implications for the commercial development of perovskite photovoltaics for outdoor applications. Therefore, although it is not possible to extract direct conclusions from T_{80} regarding the degradation mechanisms and how the recombination pathways evolve during the degradation process, it is possible to obtain complementary information from Tn_{ID2} to correlate changes in n_{ID} with recombination mechanisms or degradation processes occurring in a device. Establishing this correlation will provide critical complementary insight regarding the fundamental recombination within PSCs, which can be linked to $T_{80.}$ This relationship can then be used to improve the characterization and understanding of the outdoor degradation processes affecting PSC technologies, aid in evaluating other cell configurations and/or encapsulants, and potentially assist in linking outdoor data to indoor tests.

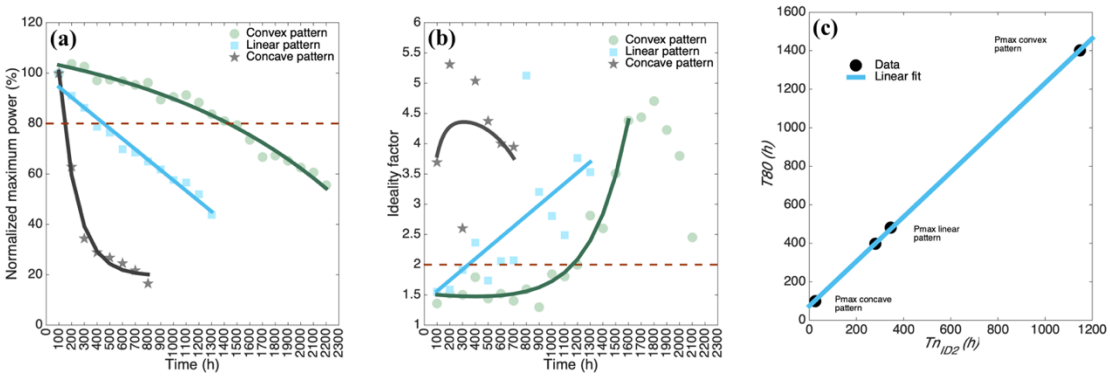

Figure 4-12. Relationship between T_{80} and n_{ID}.

a) *Average P_{max} under NOCT conditions for samples normalized concerning the initial average value during the first 100 h of exposure. The red dashed line corresponds to a 20% loss of power and is used to calculate T_{80}. The symbols represent the normalized average power (see **Figure 4-3**) for three samples exhibiting the three different characteristic patterns. The solid line of each color represents the corresponding fit to the experimental data (see **Table 4-2**).* ***b)*** *Ideality factor over time for the samples analyzed in **(a)**. The red dashed line corresponds to n_{ID} = 2 and is used to calculate Tn_{ID2}. The colored markers represent the average n_{ID} values extracted from the experimental data (see **Figure 4-9**). The solid line of each color corresponds to the fit to the data with the corresponding pattern (see **Table 4-2**).* ***c)*** *Relation between the time to reach a 20% power loss (T_{80}) and time to reach an n_{ID} value higher than 2 (Tn_{ID2}). The blue line corresponds to the fit to the data, $T_{80}=1.2Tn_{ID2}+60.1$. In all cases, solid lines correspond to fits (see **Table 4-2**), while colored symbols correspond to the fitted data.*

Table 4-2. *Fitted functions for Pmax and n_{ID}.*

Patterns	*Fitted function*
P_{max} convex /n_{ID} concave	$P_{max}(t)=100-15.9exp(6.4e^{-4}t)+20.2exp(-2.8e^{-11}t)$ $n_{ID}(t)=1.3+0.02exp(0.003t)-3.0exp(-3.33t)$
Linear	$P_{max}(t)=-0.04t+98.6$ $n_{ID}(t)=0.002t+1.4$
P_{max} concave /n_{ID} covex	$P_{max}(t)=100-83.4exp(-2.01e^{-10}t)+122.3exp(-0.008t)$ $n_{ID}(t)= 6-0.5382exp(0.0022t)-47.1329exp(-0.0319t)+0.5451exp(-0.0063t)$

Therefore, the faster power loss observed for samples with concave P_{max}/convex n_{ID} patterns can be associated with failures of the encapsulation that allowed moisture ingress, bleaching the perovskite to a yellow-white color (Domanski et al., 2018); see ***Figure 4-1***. Similarly, a rapid power drop, within less than 5 days, has also been observed in encapsulated perovskite minimodules under outdoor conditions due to a breach of the edge sealant that allowed water ingress, along with the associated color change (Stoichkov et al., 2018). For devices exhibiting convex P_{max}/concave n_{ID} data or linear data, there was no evidence of color change even after more than 900 hours of exposure; nevertheless, they also degraded, indicating another kind of degradation mechanism. Note that encapsulation protects against not only moisture ingress but also degradation originating from the release of organic components of $MAPbI_3$ into the atmosphere. Different $MAPbI_3$ degradation reactions result in the formation of a PbI_2 solid and NH_2CH_3, HI, NH_3, CH_3I (Bisquert and Juarez-Perez, 2019; McLeod and Liu, 2018), or I_2 gases (Motti et al., 2019). Correspondingly, samples exhibiting convex P_{max}/concave n_{ID} or linear patterns show different degradation rates associated with differences in the quality of the encapsulation process. During the first stage (when n_{ID}<2), the samples undergo SRH recombination dominated by lead vacancies and interstitial halogen (Motti et al., 2019). However, the

formation of different types of gases leads to the appearance of multiple trap states, causing n_{ID} to become higher than 2. These gases can be released into the atmosphere through tiny pores formed during the encapsulant preparation or produced by its degradation. Convex P_{max}/concave n_{ID} patterns could indicate of the latter case, where the rate of degradation increases after a specific time (see ***Figure 4-2*****c** and ***Figure 4-6***).

4.6 Comparison between $n_{ID,}$ P_{max} and R_{rec}.

The last section shows an essential and complementary analysis of n_{ID} to P_{max} to extract direct conclusions regarding the degradation mechanisms and how the recombination pathways evolve during the degradation process. Therefore, tracking the ideality factor helps us observe changes in the device recombination process, for instance, from bulk to surface recombination. This n_{ID} values can be validated under indoor conditions. Moreover, because the agreement between the n_{ID} values estimated from the recombination resistance extracted through IFR analysis and the values calculated from V_{oc} at different light intensities in accordance with **Equation 5**, it is also possible to correlate the P_{max} behavior with the R_{rec} behavior in order to obtain complementary information.

A comparative analysis intended to highlight the relationship between P_{max} and n_{ID}/R_{rec} related to recombination processes was performed in this regard. Hence, we simultaneously monitoring two minimodules with similar structure to the minimodules fabricated in this work (between May and November of 2018), but in large areas (50 and 70 cm^2, respectively) and using silver instead of gold as contact. P_{max} and n_{ID} were estimated from the outdoor data in accordance with the procedure shown in ***Figure 3-4***, while R_{rec} was estimated fitting the IFRs to the equivalent circuit shown in ***Figure 2-21*** to calculate the R_{rec} values.

Figure 4-13 shows some photos of monitored minimodules, remarking an important fact about the color change in the back electrode, which was visibly in the first hours of exposure. This color change was more evident in the device with an active area of 50 cm^2. Besides, considering that both samples never shown visual effects related to moisture ingress or bleaching the perovskite to a yellow-white color during the outdoor test, it was discarded that the color change in the back electrode could be related to moisture ingress.

Consequently, considering that the color of the back electrode changed, it is expected that behavior could be reflected in the impedance of the devices. In this way, some points related to the IFR over the time for both minimodules are remarked:

a) From the Nyquist diagram of impedances, ***Figure 4-14*** shows significant changes in the device's impedances with an active area of 50 cm^2 compared with the impedance of another device.
b) In a general way, related to the impedance at low frequencies, both samples showed a decreasing behavior until to reach the lower impedance values, corresponding these values to the impedance measured at 1541 h of exposure for both samples, ***Figure 4-14*****c,f**. This decreasing behavior was more progressive in the device with an active area of 70 cm^2, ***Figure 4-14*****b,e**.
c) From the impedance patterns in the Nyquist diagram, another arc's formation is observed at low frequencies. This arc could be correlated with superficial changes or charge accumulation in the surfaces of the device.

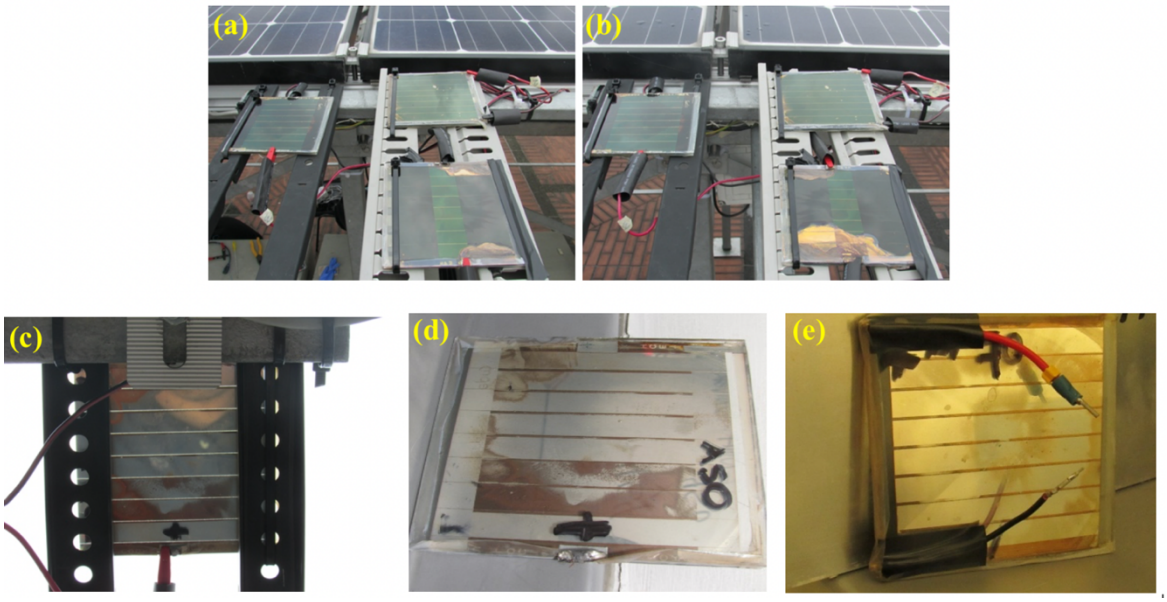

Figure 4-13. Evidence of electrode color change.

a-b) *photos of samples during a different time,* ***a)*** *installed day 0 h and* ***b)*** *168 h after installation.* ***c-e)*** *photos of the back part of the same sample located at the left top of the panel* ***(a)*** *to show the color change in the electrode. Corresponding* ***c)*** *to mounted sample in the outdoor test and* ***d)*** *to unmounted sample to observe the full-back part of device and* ***e)*** *to minimodule of 70 cm² located at the right top of the panel* ***(a).***

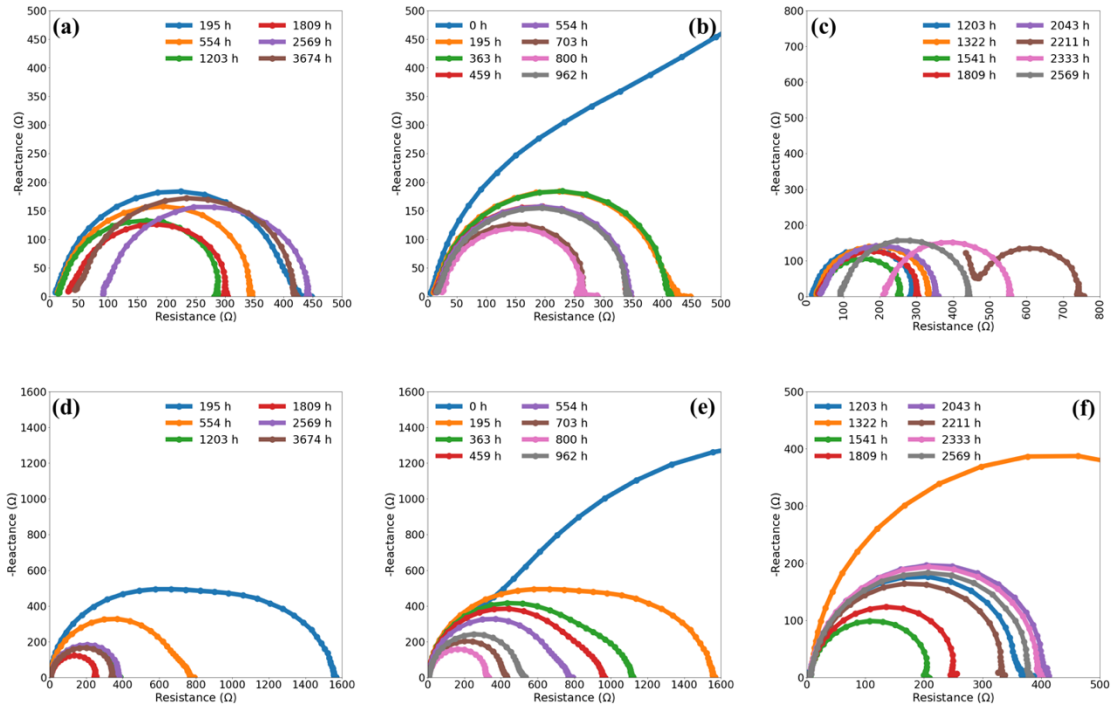

Figure 4-14. Nyquist diagram of impedance for larger minimodules.

Corresponding ***a-c)*** *to minimodule with an active area of 50 cm². d-f) to minimodule with an active area of 70 cm². a, and d) correspond to representative patterns, while b, c, e, and f) correspond to total measurements divided into two sets.*

From the Bode diagrams, ***Figure 4-15*** and ***Figure 4-16***, other aspects could be remarking:

a) The magnitude impedances spectrums clearly show that during the first 1000 h of exposure, the main changes were performed at low frequencies, while the impedances at high frequencies were almost constant, ***Figure 4-15*****b,e**. Notably, for the device that not evidenced significant color change in the back electrode (the device with an active area of 70 cm^2), the impedance at high frequencies was constant during the exposure. While the other device showed significant changes at high frequencies, suggesting that the impedance changes could be associate with the color change observed in the device, ***Figure 4-13***.

b) The capacitance spectrums shown in ***Figure 4-16*** allowed us to validate the last statement because the bulk capacitance observed at high frequencies was almost constant for larger device (70 cm^2). However, this bulk capacitance changed dramatically for the device that showed a significant color change in the back electrode. Suggesting that this behavior at high-frequencies could be correlated with the charge accumulation on the surface of devices, affecting the device's geometrical capacitance.

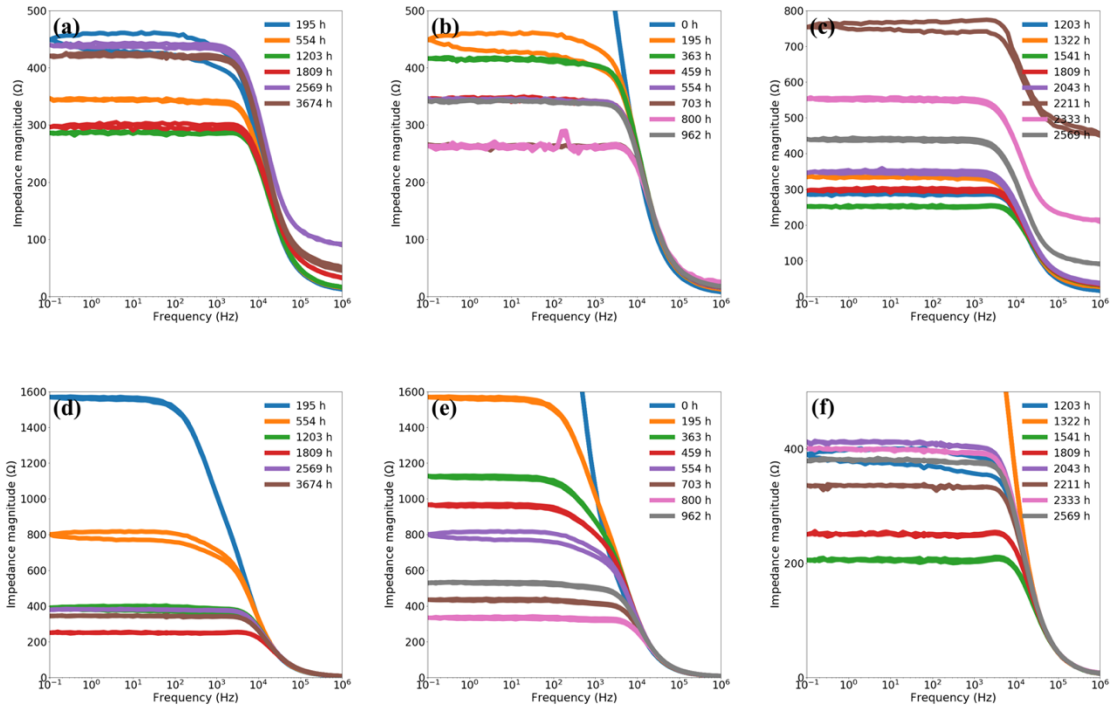

Figure 4-15. Bode diagram of impedance magnitude for larger minimodules.

*Corresponding **a-c)** to minimodule with an active area of 50 cm^2. **d-f)** to minimodule with an active area of 70 cm^2. **a, and d)** correspond to representative patterns, while **b, c, e, and f)** correspond to full measurements divided in two sets.*

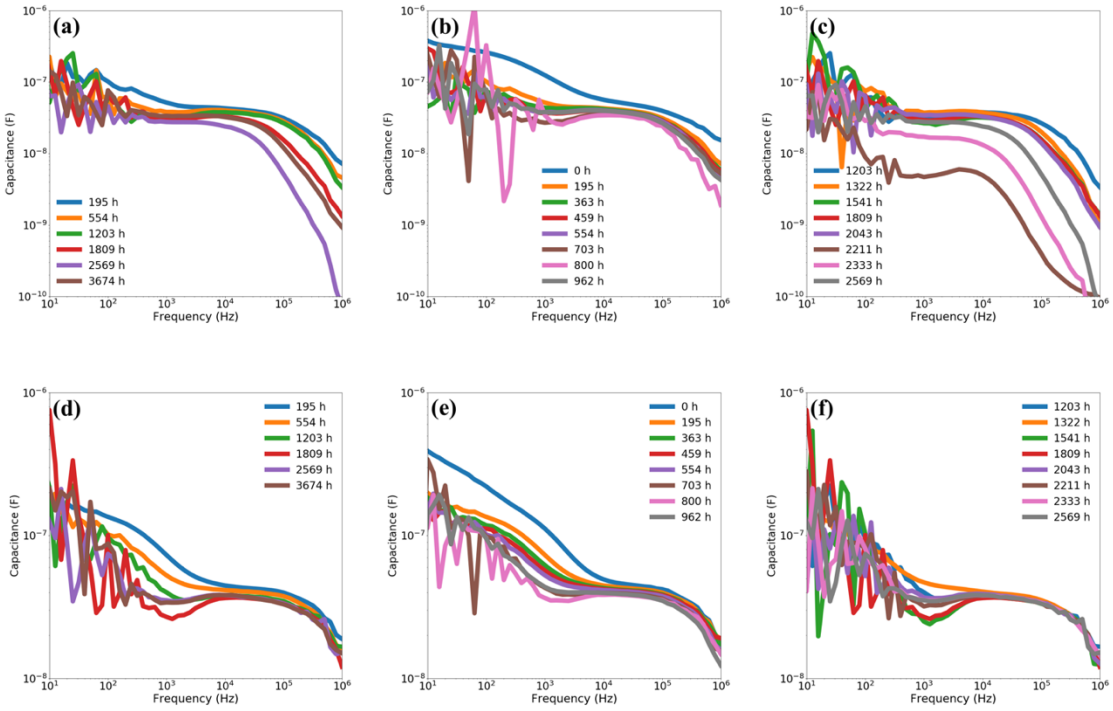

Figure 4-16. Bode diagram of capacitance for the larger minimodules.
*Corresponding **a-c)** to minimodule with an active area of 70 cm^2. **d-f)** to minimodule with an active area of 50 cm^2. **a, and d)** correspond to representative patterns, while **b, c, e, and f)** correspond to total measurements divided into two sets.*

Accordingly, to compare the P_{max} and n_{ID} behavior with the R_{rec} behavior, the R_{rec} values over time for both samples were estimated, fitting the IFR measurements to the equivalent circuit shown in ***Figure 2-21*** to extract this parameter. ***Figure 4-17*** compares the three variables normalized concerning the mean value of the first 100 h of exposure. The complete outdoor performance for both samples is shows in ***Figure 4-18*** and ***Figure 4-19***.

From the results shown in ***Figure 4-17***, it can be observed that P_{max} exhibits monotonic behavior, while n_{ID} and R_{rec} show similar and richer patterns that allow the changes in the recombination mechanism to be tracked more directly than can be achieved with P_{max}. For example, n_{ID} is constant in both examples during the first hours, while R_{rec} decreases, pointing to an increase in the SRH defects density. At 800 h, n_{ID} increases while R_{rec} increases. The n_{ID} evolution indicates multiple level defect formation while the R_{rec} increase points to an increase of transport resistance due to the apparition of defects, as recombination resistance and transport resistance are coupled in perovskite solar cells. These observations illustrate the valuable complementarity that the determination of n_{ID} can provide for studying and understanding outdoor PSM tests. This approach can be employed as a diagnostic tool to detect initial failures or validate the device's status.

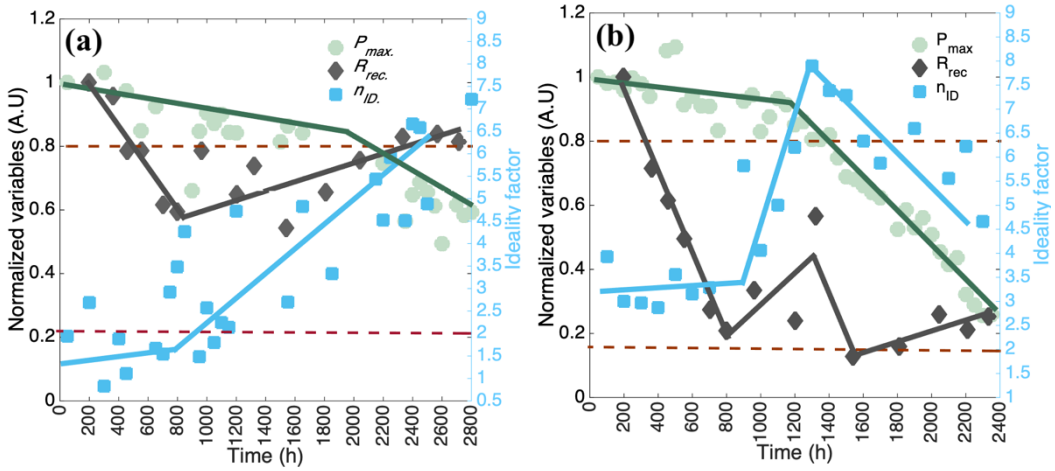

Figure 4-17. Comparison between P_{max}, n_{ID}, and R_{rec} from the outdoor test.

a) *data related to MAPI minimodule of 70 cm² of active area (sample on the top of left part in* ***Figure 4-13a-b****).* ***b)*** *data related to MAPI minimodule of 50 cm² of active area (sample on the top of right part in* ***Figure 4-13a-b****). P_{max} and R_{rec} are represented in the left axis, while the right axis is related to n_{ID}. Also, red dashed lines are included to indicate the T_{80} and Tn_{ID2}, while color lines are included as a visual guide to show the variables' behavior.*

It is worth noting that despite both devices were fabricated and evaluated under similar conditions, and both devices exhibited similar trends between P_{max} and I_{sc} (***Figure 4-18***e and ***Figure 4-19***e), hence, some particularities could be remarking:

a) The P_{max} evolution for the sample with an active area of 50 cm² could be correlated to the convex pattern, ***Figure 4-18*****a and e**. This pattern was also evidenced in the first 1500 h of exposure for the n_{ID} behavior depicted in ***Figure 4-18*****f**. Nevertheless, the initial n_{ID} values are higher than 2, pointing to surface recombination, fact in accordance with the lower V_{oc} (lower than 5.6 V), ***Figure 4-18*****d**. The V_{oc} exhibits a decreasing behavior that agrees with the impedance changes observed at high frequencies, which shown in a general way an increasing behavior over time (***Figure 4-15*****a-c**), suggesting changes on the surfaces or on the electrode contacts. Also, based on the capacitance behavior depicted in ***Figure 4-16*****a-c**, it is observed changes in the capacitance at low frequency, suggesting changes in the bulk. In contrast, changes at high frequency suggesting changes on the electrodes.

b) The P_{max} evolution for the sample with an active area of 70 cm² could be correlated to the linear pattern, ***Figure 4-19*****a and e**. Behavior in accordance with the linear n_{ID} behavior depicted in ***Figure 4-19*****f**. Which is characterized by n_{ID} values lower than 2 in the first hours of exposure and almost constant V_{oc} values (close to 7 V considering the 8 cells in series). Also, based on the capacitance behavior depicted in ***Figure 4-16*****d-f**, the capacitance's main changes were at low frequency, which suggests charge accumulation or changes on the electrodes' surface. This fact is evidenced in the formation of the second arc at low frequency in the Nyquist diagram.

c) Finally, based on the decreasing behavior shown by the photocurrent, the almost constant behavior by V_{oc}, and the increasing behavior shown by n_{ID} for both devices, it suggests that the decrease of the charge extraction observed by the I_{sc} behavior could be correlated to surface recombination because of the multiple level defect formation indicated by the n_{ID} values.

Although other analyses are necessary to correlate the ion migration or other physical/chemical phenomena with the change color of the back electrode. It is possible to infer that the capacitance changes at low frequency observed as the formation of another arc in the impedance Nyquist diagrams could be correlated with the electrode's charge accumulation (Caram et al., 2020). The charge accumulation on electrodes could produce the redox reactions between metal contacts and iodide for silver electrodes, as was pointed in (Grancini et al., 2017), producing the interfacial degradation of the metal contact (Guerrero et al., 2016b). This accumulation of negatively charged ions (I^-) in the ETL is because of the drift of ionic vacancies as it was observed in MAPI with symmetric gold electrodes (Li et al., 2018) or complete perovskite devices (Bertoluzzi et al., 2019). Therefore, this mechanism could be mainly correlated with the formation of multiple level defects observed in the n_{ID}/R_{rec} behavior.

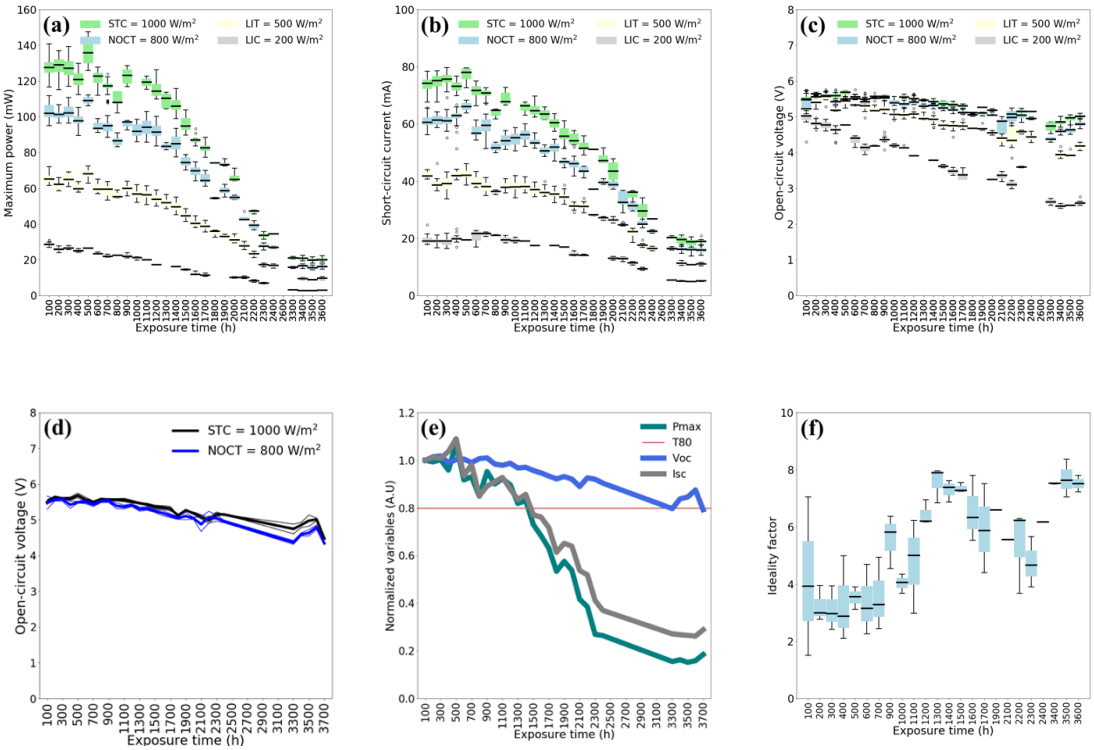

Figure 4-18. Outdoor performance for minimodules with an active area of 50 cm².
a) *Maximum power.* ***b)*** *short-circuit current.* ***c)*** *Open-circuit voltage.* ***d)*** *Open-circuit voltage at STC and NOCT.* ***e)*** *Normalized variables concerning the mean values of first 100 h of exposure.* ***f)*** *Ideality factor from outdoor data.*

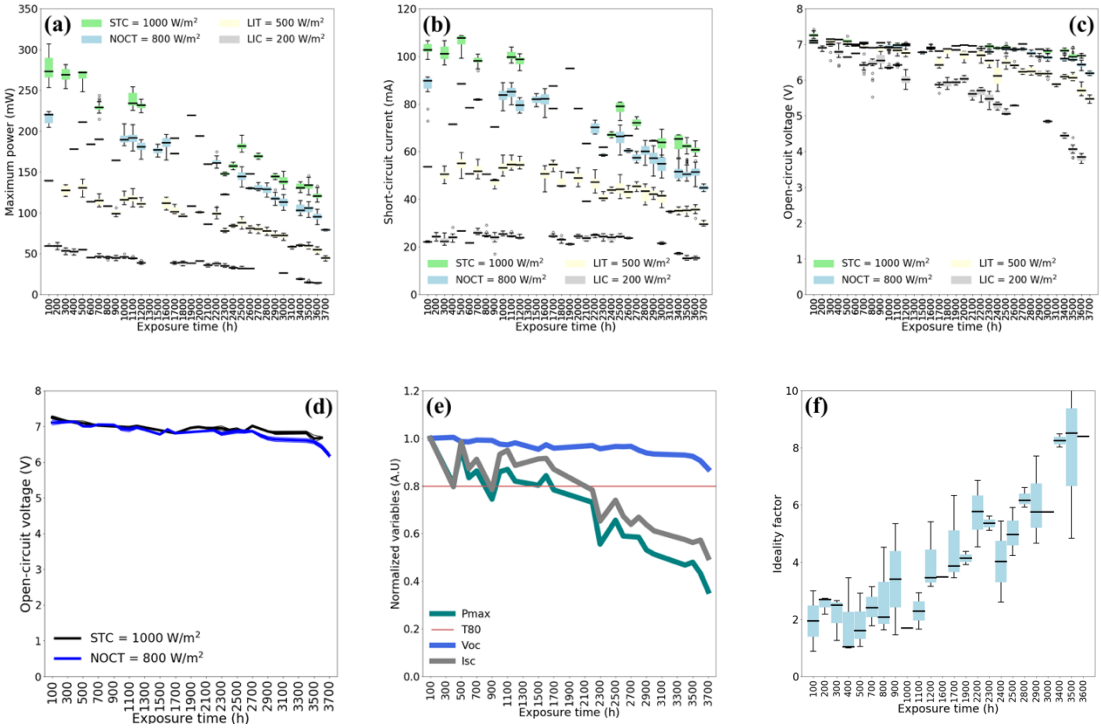

Figure 4-19. Outdoor performance for minimodule with an active area of 70 cm².

a) *Maximum power.* ***b)*** *short-circuit current.* ***c)*** *Open-circuit voltage.* ***d)*** *Open-circuit voltage at STC and NOCT.* ***e)*** *Normalized variables concerning the mean values of first 100 h of exposure.* ***f)*** *Ideality factor from outdoor data.*

4.7 Conclusions

This chapter presented a complementary methodology based on evaluating the ideality factor for monitoring the outdoor performance of halide perovskite solar cells, which can improve device characterization under outdoor testing conditions. This methodology takes advantage of the properties of this new class of photovoltaic technology and the direct relationship between n_{ID} and the recombination pathway to provide insight to enable improved data interpretation and understanding of the device degradation processes under outdoor conditions that are relevant to the commercial application of PSCs. By applying this methodology, a high-throughput outdoor performance analysis of $MAPbI_3$ minimodules was carried out following the international standard IEC 61853-1 to evaluate the impact of weather variables on performance. The collected data were processed in measurement sets based on measurements recorded over 100 h of exposure. In each set, n_{ID} was calculated while taking advantage of the different illumination conditions encountered during day-night cycles. The outdoor performance was calculated based on the NOCT power rating conditions identified in the IEC 61853-1 standard.

Taking advantage of the low dependence of PSCs on temperature, we proposed and then demonstrated an analysis of outdoor performance using n_{ID}. The main advantage of this approach is that it provides direct physical insight related to recombination processes. To this end, we defined Tn_{ID2} as the time at which n_{ID} first reaches a value of 2, with a physical meaning related to the transition point between bulk SRH recombination through a single level to recombination through multiple levels because of device degradation. We showed that the three different degradation patterns identified for P_{max} can also be identified by monitoring n_{ID}. Also, based on the linear relationship between T_{80} and Tn_{ID2}, these two indexes are correlated. Consequently, it is possible to take advantage of their complementarity for the future development of PSCs. While T_{80} provides direct commercial information, namely, the module lifetime, Tn_{ID2} provides direct information on recombination behavior and physical insight into the device state. Therefore, the proposed method provides a deeper understanding of the evolution of recombination processes originating from different degradation mechanisms, revealing not just the degradation profile but also how it is produced in terms of recombination pathways. This complementarity is especially interesting for photovoltaic devices whose outdoor behavior is under study, development, and optimization, as is currently the case for perovskite solar cells.

Finally, it should be noted that each technology has its peculiarities, which often necessitate the revision of characterization methods, and PSCs are no exception. Proof of this is provided by the very recent consensus related to the stability measurement of PSCs. Here, we contribute to this discussion by providing a high-throughput analysis that takes advantage of the peculiarities of perovskite technology to determine the outdoor performance of PSCs. Regarding future systematic studies of PSCs operating outdoors, we recommend reporting data collected under the NOCT power rating conditions suggested by IEC 61853-1, which are commonly addressed in datasheets for commercial technologies and are possible to achieve under outdoor tests. The complementary analysis and determination of n_{ID} can provide critical information for device characterization and the understanding of degradation processes to accelerate the optimization of this technology or other technologies with similar properties that could be under development.

5. General Conclusions

Here, minimodules of approximately 8 cm^2 and 4 sub-cells connected in series were fabricated and encapsulated with EVA. The reached higher efficiencies (close to 12 %) were in the current range reported in the literature for minimodules with a similar area, that is, between 10 and 17 % (Liu et al., 2020). Besides, the higher FF and V_{oc} allowed validation of the performed interconnection process to reduces electrical losses. This is the main advantage of the series connection of cells instead of large-area (monolithic) solar cells.

The devices were characterized not only by the I-V curve data but also by the ideality factor and impedance spectra. In this regard, an Autolab procedure was implemented to estimate the n_{ID} under indoor conditions, in accordance with the flowchart shown in ***Figure 2-26***. Therefore, an optimization process combining genetic algorithm and Simplex method was implemented to estimate the n_{ID} values from the impedance spectra as a function of light or form the I-V curve data. It is worth noting that the fitted impedance frequency response using the equivalent circuit model successfully reproduced the impedance patterns under different light conditions for minimodules, cells, and incomplete cells. This fact highlighted the accuracy of the implemented optimization process and the robustness of the selected equivalent circuit to model the perovskite devices' impedance frequency response.

To evaluate the outdoor performance of PV devices under natural sunlight without a tracker, the developed solar tracers were synchronized with the monitoring system to measure the I-V curve following IEC 61853-1, providing a complete characterization of the devices under various irradiance and temperature conditions, allowing determination of the impact of weather variables on P_{max}, V_{oc}, and I_{sc}. This procedure was implemented in Python functions on remote server to estimate the power rating conditions of photovoltaic technologies such as silicon, HIT, CIGS and perovskite.

The outdoor performance allowed a comparison of the emerging perovskite technology with a well-known and optimized silicon technology, observing similarities between photovoltaic parameters such as power delivery. Hence, higher values of the normalized short circuit current for perovskite modules were obtained when compared to the silicon modules, suggesting that perovskite technology can produce higher relative current values in a broader range of irradiances. Besides, the positive temperature dependence of the V_{oc} under high irradiance levels was also observed for perovskites minimodules. These results show for the first time that perovskite minimodules can be a robust PV technology to be used under outdoor conditions. This positive performance dependence on temperature and irradiance is a competitive fact in development of this technology.

On the other hand, the perovskite minimodules outdoor evaluation allowed observation of three maximum power (P_{max}) evolution patterns, named convex, linear, and concave patterns because of the exhibited shapes. In this sense, all the analyzed minimodules can be statistically associated with one of these three patterns, commonly described for degradation processes in the literature to study possible degradation paths and estimate the failure time. Therefore, to analyze these degradation behaviors (estimated at STC and NOCT), well-known statistical models such as linear regression models were used to estimate the degradation rate and lifetime (T_{80}).

Besides, due to the day-night cycles, including dawn and noon conditions, which can naturally provide a broad range of illumination conditions, it was proposed to estimate n_{ID} from the open-circuit voltage (V_{oc}) dependence on irradiance and ambient temperature (outdoor data). Consequently, because this parameter has been used to define solar device's electrical behavior due to its relationship with conduction, transport, recombination, and behavior at interface junctions, the changes in n_{ID}

could be correlated with the recombination mechanisms or degradation processes occurring in the device. In this context, it was observed that the three different degradation patterns identified for P_{max} can also be identified by n_{ID}, highlighting the importance for evaluating the ideality factor and monitoring the outdoor performance of halide perovskite solar cells.

Finally, taking advantage of the low dependence of PSCs on temperature, it was proposed and then demonstrated an analysis of outdoor performance using n_{ID}. The main advantage of this approach is that it provides direct physical insight related to recombination processes. To this end, we defined Tn_{ID2} as the time at which n_{ID} first reaches a value of 2, with a physical meaning related to the transition point between bulk SRH recombination through a single level to recombination through multiple levels because of device degradation. Also, based on the linear relationship between T_{80} and Tn_{ID2}, these two indexes are correlated. Consequently, it is possible to take advantage of their complementarity for the future development of PSCs. While T_{80} provides direct commercial information, namely, the module lifetime, Tn_{ID2} provides direct information on recombination behavior and physical insight into the device state.

6. References

Agarwal, S., Seetharaman, M., Kumawat, N.K., Subbiah, A.S., Sarkar, S.K., Kabra, D., Namboothiry, M.A.G., Nair, P.R., 2014. On the Uniqueness of Ideality Factor and Voltage Exponent of Perovskite-Based Solar Cells. J. Phys. Chem. Lett. 5, 4115–4121. https://doi.org/10.1021/jz5021636

Agroui, K., 2012. Indoor and Outdoor Characterizations of Photovoltaic Module Based on Mulicrystalline Solar Cells. Energy Procedia 18, 857–866. https://doi.org/10.1016/j.egypro.2012.05.100

Almora, O., Aranda, C., Mas-Marzá, E., Garcia-Belmonte, G., 2016. On Mott-Schottky analysis interpretation of capacitance measurements in organometal perovskite solar cells. Appl. Phys. Lett. 109, 173903. https://doi.org/10.1063/1.4966127

Almora, O., Cho, K.T., Aghazada, S., Zimmermann, I., Matt, G.J., Brabec, C.J., Nazeeruddin, M.K., Garcia-Belmonte, G., 2018. Discerning recombination mechanisms and ideality factors through impedance analysis of high-efficiency perovskite solar cells. Nano Energy 48, 63–72. https://doi.org/10.1016/j.nanoen.2018.03.042

Anoop, K.M., Khenkin, M. V., Di Giacomo, F., Galagan, Y., Rahmany, S., Etgar, L., Katz, E.A., Visoly-Fisher, I., 2020. Bias-Dependent Stability of Perovskite Solar Cells Studied Using Natural and Concentrated Sunlight. Sol. RRL 4, 1900335. https://doi.org/10.1002/solr.201900335

Araki, K., Yamaguchi, M., 2003. Novel equivalent circuit model and statistical analysis in parameters identification. Sol. Energy Mater. Sol. Cells 75, 457–466. https://doi.org/10.1016/S0927-0248(02)00204-0

Bai, J., Liu, S., Hao, Y., Zhang, Z., Jiang, M., Zhang, Y., 2014. Development of a new compound method to extract the five parameters of PV modules. Energy Convers. Manag. 79, 294–303. https://doi.org/10.1016/j.enconman.2013.12.041

Barsoukov, E., Macdonald, J.R., 2005. Impedance Spectroscopy, Second dit. ed, Impedance Spectroscopy: Theory, Experiment, and Applications. New Jersey. https://doi.org/10.1002/0471716243

Bashahu, M., Nkundabakura, P., 2007. Review and tests of methods for the determination of the solar cell junction ideality factors. Sol. Energy 81, 856–863. https://doi.org/10.1016/j.solener.2006.11.002

Bertoluzzi, L., Boyd, C.C., Rolston, N., Xu, J., Prasanna, R., O'Regan, B.C., McGehee, M.D., 2019. Mobile Ion Concentration Measurement and Open-Access Band Diagram Simulation Platform for Halide Perovskite Solar Cells. Joule. https://doi.org/10.1016/j.joule.2019.10.003

Bisquert, J., Juarez-Perez, E.J., 2019. The Causes of Degradation of Perovskite Solar Cells. J. Phys. Chem. Lett. 10, 5889–5891. https://doi.org/10.1021/acs.jpclett.9b00613

Booth, H., 2010. Laser processing in industrial solar module manufacturing. J. Laser Micro Nanoeng. 5, 183–191. https://doi.org/10.2961/jlmn.2010.03.0001

Boutana, N., Mellit, A., Haddad, S., Rabhi, A., Pavan, A.M., 2017. An explicit I-V model for

photovoltaic module technologies. Energy Convers. Manag. 138, 400–412. https://doi.org/10.1016/j.enconman.2017.02.016

Boyd, C.C., Cheacharoen, R., Leijtens, T., McGehee, M.D., 2019. Understanding Degradation Mechanisms and Improving Stability of Perovskite Photovoltaics. Chem. Rev. 119, 3418–3451. https://doi.org/10.1021/acs.chemrev.8b00336

Calado, P., Telford, A.M., Bryant, D., Li, X., Nelson, J., O'Regan, B.C., Barnes, P.R.F., 2016. Evidence for ion migration in hybrid perovskite solar cells with minimal hysteresis. Nat. Commun. 7, 13831. https://doi.org/10.1038/ncomms13831

Cano, J.B., Valencia, J., Jaramillo, F., Velilla, E., 2015. Desarrollo e implementación de prototipo electrónico para la caracterización de paneles solares en condiciones de exteriores 11, 41–50.

Caracciolo, F., Dallago, E., Finarelli, D.G., Liberale, A., Merhej, P., 2012. Single-Variable Optimization Method for Evaluating Solar Cell and Solar Module Parameters. IEEE J. Photovoltaics 2, 173–180. https://doi.org/10.1109/JPHOTOV.2011.2182181

Caram, J., García-Batlle, M., Almora, O., Arce, R.D., Guerrero, A., Garcia-Belmonte, G., 2020. Direct observation of surface polarization at hybrid perovskite/Au interfaces by dark transient experiments. Appl. Phys. Lett. 116, 183503. https://doi.org/10.1063/5.0006409

Carrero, C., Ramírez, D., Rodríguez, J., Platero, C.A., 2011. Accurate and fast convergence method for parameter estimation of PV generators based on three main points of the I–V curve. Renew. Energy 36, 2972–2977. https://doi.org/10.1016/j.renene.2011.04.001

Chan, D.S.H., Phillips, J.R., Phang, J.C.H., 1986. A comparative study of extraction methods for solar cell model parameters. Solid. State. Electron. 29, 329–337. https://doi.org/10.1016/0038-1101(86)90212-1

Cheacharoen, R., Rolston, N., Harwood, D., Bush, K.A., Dauskardt, R.H., McGehee, M.D., 2018. Design and understanding of encapsulated perovskite solar cells to withstand temperature cycling. Energy Environ. Sci. 11, 144–150. https://doi.org/10.1039/C7EE02564E

Chegaar, M., Azzouzi, G., Mialhe, P., 2006. Simple parameter extraction method for illuminated solar cells. Solid. State. Electron. 50, 1234–1237. https://doi.org/10.1016/j.sse.2006.05.020

Christians, J.A., Manser, J.S., Kamat, P. V., 2015. Best practices in perovskite solar cell efficiency measurements. Avoiding the error of Making Bad Cells Look Good. J. Phys. Chem. Lett. https://doi.org/10.1021/acs.jpclett.5b00289

Ciro, J., Mesa, S., Uribe, J.I., Mejía-Escobar, M.A., Ramirez, D., Montoya, J.F., Betancur, R., Yoo, H.-S., Park, N.-G., Jaramillo, F., 2017a. Optimization of the Ag/PCBM interface by a rhodamine interlayer to enhance the efficiency and stability of perovskite solar cells. Nanoscale 9, 9440–9446. https://doi.org/10.1039/C7NR01678F

Ciro, J., Ramírez, D., Mejía Escobar, M.A., Montoya, J.F., Mesa, S., Betancur, R., Jaramillo, F., 2017b. Self-Functionalization Behind a Solution-Processed NiO x Film Used As Hole Transporting Layer for Efficient Perovskite Solar Cells. ACS Appl. Mater. Interfaces 9, 12348–12354. https://doi.org/10.1021/acsami.6b15975

Contreras-Bernal, L., Ramos-Terrón, S., Riquelme, A., Boix, P.P., Idígoras, J., Mora-Seró, I., Anta, J.A., 2019. Impedance analysis of perovskite solar cells: A case study. J. Mater. Chem. A 7,

12191–12200. https://doi.org/10.1039/c9ta02808k

Cotfas, D.T., Cotfas, P.A., Kaplanis, S., 2013. Methods to determine the dc parameters of solar cells: A critical review. Renew. Sustain. Energy Rev. 28, 588–596. https://doi.org/10.1016/j.rser.2013.08.017

Cowan, S.R., Roy, A., Heeger, A.J., 2010. Recombination in polymer-fullerene bulk heterojunction solar cells. Phys. Rev. B 82, 245207. https://doi.org/10.1103/PhysRevB.82.245207

Cubas, J., Pindado, S., Victoria, M., 2014. On the analytical approach for modeling photovoltaic systems behavior. J. Power Sources 247, 467–474. https://doi.org/10.1016/j.jpowsour.2013.09.008

Dash, P.K., Gupta, N.C., Rawat, R., Pant, P.C., 2017. A novel climate classification criterion based on the performance of solar photovoltaic technologies. Sol. Energy 144, 392–398. https://doi.org/10.1016/j.solener.2017.01.046

de Blas, M.., Torres, J.., Prieto, E., García, A., 2002. Selecting a suitable model for characterizing photovoltaic devices. Renew. Energy 25, 371–380. https://doi.org/10.1016/S0960-1481(01)00056-8

Deceglie, M.G., Silverman, T.J., Marion, B., Kurtz, S.R., 2015. Real-Time Series Resistance Monitoring in PV Systems Without the Need for I–V Curves. IEEE J. Photovoltaics 5, 1706–1709. https://doi.org/10.1109/JPHOTOV.2015.2478070

Deng, Y., Van Brackle, C.H., Dai, X., Zhao, J., Chen, B., Huang, J., 2019. Tailoring solvent coordination for high-speed, room-temperature blading of perovskite photovoltaic films. Sci. Adv. 5, eaax7537. https://doi.org/10.1126/sciadv.aax7537

Domanski, K., Alharbi, E.A., Hagfeldt, A., Grätzel, M., Tress, W., 2018. Systematic investigation of the impact of operation conditions on the degradation behaviour of perovskite solar cells. Nat. Energy 3, 61–67. https://doi.org/10.1038/s41560-017-0060-5

Domanski, K., Roose, B., Matsui, T., Saliba, M., Turren-Cruz, S.-H., Correa-Baena, J.-P., Carmona, C.R., Richardson, G., Foster, J.M., De Angelis, F., Ball, J.M., Petrozza, A., Mine, N., Nazeeruddin, M.K., Tress, W., Grätzel, M., Steiner, U., Hagfeldt, A., Abate, A., 2017. Migration of cations induces reversible performance losses over day/night cycling in perovskite solar cells. Energy Environ. Sci. 10, 604–613. https://doi.org/10.1039/C6EE03352K

Duran, E., Piliougine, M., Sidrach-De-Cardona, M., Galan, J., Andujar, J.M., 2008. Different methods to obtain the I-V curve of PV modules: A review. Conf. Rec. IEEE Photovolt. Spec. Conf. https://doi.org/10.1109/PVSC.2008.4922578

Eltamaly, A.M., Farh, H.M.H., Othman, M.F., 2018. A novel evaluation index for the photovoltaic maximum power point tracker techniques. Sol. Energy 174, 940–956. https://doi.org/10.1016/j.solener.2018.09.060

Enrique, J.M., Duran, E., Sidrach-de-Cardona M, Andujar, J.M., Bohorquez, M.A., Carretero, J., 2005. A new approach to obtain I-V and P-V curves of photovoltaic modules by using DC-DC converters, in: Conference Record of the Thirty-First IEEE Photovoltaic Specialists Conference, 2005. IEEE, pp. 1769–1772. https://doi.org/10.1109/PVSC.2005.1488493

Fabregat-Santiago, F., Garcia-Belmonte, G., Mora-Seró, I., Bisquert, J., 2011. Characterization of nanostructured hybrid and organic solar cells by impedance spectroscopy. Phys. Chem. Chem. Phys. 13, 9083. https://doi.org/10.1039/c0cp02249g

Faifer, M., Cristaldi, L., Piegari, L., Soulatiantork, P., 2015. Design of a converter for photovoltaic panels testing. 5th Int. Conf. Clean Electr. Power Renew. Energy Resour. Impact, ICCEP 2015 674–681. https://doi.org/10.1109/ICCEP.2015.7177564

Gaglia, A.G., Lykoudis, S., Argiriou, A.A., Balaras, C.A., Dialynas, E., 2017. Energy efficiency of PV panels under real outdoor conditions–An experimental assessment in Athens, Greece. Renew. Energy 101, 236–243. https://doi.org/10.1016/j.renene.2016.08.051

Galagan, Y., 2018. Perovskite Solar Cells: Toward Industrial-Scale Methods. J. Phys. Chem. Lett. 4326–4335. https://doi.org/10.1021/acs.jpclett.8b01356

Galagan, Y., Coenen, E.W.C., Verhees, W., Andriessen, R., 2016. Towards scaling up of perovskite solar cells and modules. J. Mater. Chem. A 4, 5700–5705. https://doi.org/10.1039/C6TA01134A

Ghahremanirad, E., Bou, A., Olyaee, S., Bisquert, J., 2017. Inductive Loop in the Impedance Response of Perovskite Solar Cells Explained by Surface Polarization Model. J. Phys. Chem. Lett. 8, 1402–1406. https://doi.org/10.1021/acs.jpclett.7b00415

Gonzalez-Pedro, V., Juarez-Perez, E.J., Arsyad, W.-S., Barea, E.M., Fabregat-Santiago, F., Mora-Sero, I., Bisquert, J., 2014. General Working Principles of CH 3 NH 3 PbX 3 Perovskite Solar Cells. Nano Lett. 14, 888–893. https://doi.org/10.1021/nl404252e

Grancini, G., Roldán-Carmona, C., Zimmermann, I., Mosconi, E., Lee, X., Martineau, D., Narbey, S., Oswald, F., De Angelis, F., Graetzel, M., Nazeeruddin, M.K., 2017. One-Year stable perovskite solar cells by 2D/3D interface engineering. Nat. Commun. 8, 15684. https://doi.org/10.1038/ncomms15684

Green, M.A., Blakers, A.W., Osterwald, C.R., 1985. Characterization of high-efficiency silicon solar cells. J. Appl. Phys. 58, 4402–4408. https://doi.org/10.1063/1.336286

Green, M.A., Dunlop, E.D., Hohl-Ebinger, J., Yoshita, M., Kopidakis, N., Ho-Baillie, A.W.Y., 2020. Solar cell efficiency tables (Version 55). Prog. Photovoltaics Res. Appl. 28, 3–15. https://doi.org/10.1002/pip.3228

Green, M.A., Emery, K., Hishikawa, Y., Warta, W., Dunlop, E.D., Levi, D.H., Ho-Baillie, A.W.Y., 2017. Solar cell efficiency tables (version 49). Prog. Photovoltaics Res. Appl. 25, 3–13. https://doi.org/10.1002/pip.2855

Green, M.A., Hishikawa, Y., Dunlop, E.D., Levi, D.H., Hohl-Ebinger, J., Ho-Baillie, A.W.Y., 2018. Solar cell efficiency tables (version 51). Prog. Photovoltaics Res. Appl. 26, 3–12. https://doi.org/10.1002/pip.2978

Guerrero, A., Garcia-Belmonte, G., Mora-Sero, I., Bisquert, J., Kang, Y.S., Jacobsson, T.J., Correa-Baena, J.-P., Hagfeldt, A., 2016a. Properties of Contact and Bulk Impedances in Hybrid Lead Halide Perovskite Solar Cells Including Inductive Loop Elements. J. Phys. Chem. C 120, 8023–8032. https://doi.org/10.1021/acs.jpcc.6b01728

Guerrero, A., You, J., Aranda, C., Kang, Y.S., Garcia-Belmonte, G., Zhou, H., Bisquert, J., Yang,

Y., 2016b. Interfacial Degradation of Planar Lead Halide Perovskite Solar Cells. ACS Nano 10, 218–224. https://doi.org/10.1021/acsnano.5b03687

Gustavsen, B., Semlyen, A., 1999. Rational approximation of frequency domain responses by vector fitting. IEEE Trans. Power Deliv. 14, 1052–1059. https://doi.org/10.1109/61.772353

Hamou, S., Zine, S., Abdellah, R., 2014. Efficiency of PV module under real working conditions. Energy Procedia 50, 553–558. https://doi.org/10.1016/j.egypro.2014.06.067

Harald, Ñ., Seeland, M., Muhsin, B., 2012. Optimal geometric design of monolithic thin-film solar modules: Architecture of polymer solar cells. Sol. Energy Mater. Sol. Cells 97, 119–126. https://doi.org/10.1016/j.solmat.2011.09.037

Hasan, M.A., Parida, S.K., Lindroos, J., Savin, H., Humada, A.M., Hojabri, M., Mekhilef, S., Hamada, H.M., Gupta, N.D., Janyani, V., Courel, M., Pulgarín-Agudelo, F.A., Andrade-Arvizu, J.A., Vigil-Galán, O., Kumar, P., Bilen, C., Vaughan, B., Zhou, X., Dastoor, P.C., Belcher, W.J., Chine, W., Mellit, A., Lughi, V., Malek, A., Sulligoi, G., Massi Pavan, A., Hejri, M., Mokhtari, H., Azizian, M.R., Söder, L., Barbato, M., Barbato, A., Meneghini, M., Cester, A., Mura, G., Tonini, D., Voltan, A., Cellere, G., Meneghesso, G., Yildiran, N., Tacer, E., Lan, D., Green, M.A., Wang, D., Wright, M., Elumalai, N.K., Uddin, A., Almosni, S., Rale, P., Cornet, C., Perrin, M., Lombez, L., Létoublon, A., Tavernier, K., Levallois, C., Rohel, T., Bertru, N., Guillemoles, J.F., Durand, O., Ma, J., Man, K.L., Guan, S.-U., Ting, T.O., Wong, P.W.H., Sharma, V., Singh, V., Arora, M., Arora, S., Tandon, R.P., Xiong, J., Yang, B., Cao, C., Wu, R., Huang, Y., Sun, J., Zhang, J., Liu, C., Tao, S., Gao, Y., Yang, J., Gretener, C., Perrenoud, J., Kranz, L., Cheah, E., Dietrich, M., Buecheler, S., Tiwari, A.N., Ghannam, M., Abdulraheem, Y., Shehada, G., Urbain, F., Smirnov, V., Becker, J.-P., Lambertz, A., Rau, U., Finger, F., Dubey, A., Adhikari, N., Venkatesan, S., Gu, S., Khatiwada, D., Wang, Q., Mohammad, L., Kumar, M., Qiao, Q., Ayodele, T.R., Ogunjuyigbe, A.S.O., Ekoh, E.E., Karakaya, E., Liao, T., Chen, X., Lin, B., Chen, J., Du, Y., Fell, C.J., Duck, B., Chen, D., Liffman, K., Zhang, Y., Gu, M., Zhu, Y., Belarbi, M., Boudghene-Stambouli, A., Belarbi, E.-H., Haddouche, K., Huang, Q., Reuter, K.B., Zhu, Y., Deline, V.R., Shahbazi, M., Wang, H., Arredondo, B., Martín-López, M.B., Romero, B., Vergaz, R., Romero-Gomez, P., Martorell, J., Zhou, Y., Gray-Weale, A., Gong, J., Sumathy, K., Liang, J., Felekidis, N., Wang, E., Kemerink, M., 2016. Performance evaluation and parametric optimum design of a vacuum thermionic solar cell. Sol. Energy Mater. Sol. Cells 147, 4476–4486. https://doi.org/10.1016/j.seta.2015.11.003

Hasan, O., Arif, A.F.M., 2014. Performance and life prediction model for photovoltaic modules: Effect of encapsulant constitutive behavior. Sol. Energy Mater. Sol. Cells 122, 75–87. https://doi.org/10.1016/j.solmat.2013.11.016

Hassaine, L., Mraoui, A., Khelif, M., 2014. Low cost electronic load for out-door testing of photovoltaic panels. IREC 2014 - 5th Int. Renew. Energy Congr. 1–6. https://doi.org/10.1109/IREC.2014.6826944

He, S., Qiu, L., Ono, L.K., Qi, Y., 2020. How far are we from attaining 10-year lifetime for metal halide perovskite solar cells? Mater. Sci. Eng. R Reports 140, 100545. https://doi.org/10.1016/j.mser.2020.100545

Heo, S., Seo, G., Lee, Y., Seol, M., Kim, S.H., Yun, D.-J., Kim, Y., Kim, K., Lee, Junho, Lee, Jooho, Jeon, W.S., Shin, J.K., Park, J., Lee, D., Nazeeruddin, M.K., 2019. Origins of High

Performance and Degradation in the Mixed Perovskite Solar Cells. Adv. Mater. 31, 1805438. https://doi.org/10.1002/adma.201805438

Holzhey, P., Saliba, M., 2018. A full overview of international standards assessing the long-term stability of perovskite solar cells. J. Mater. Chem. A 6, 21794–21808. https://doi.org/10.1039/C8TA06950F

Hoye, R.L.Z., Schulz, P., Schelhas, L.T., Holder, A.M., Stone, K.H., Perkins, J.D., Vigil-Fowler, D., Siol, S., Scanlon, D.O., Zakutayev, A., Walsh, A., Smith, I.C., Melot, B.C., Kurchin, R.C., Wang, Y., Shi, J., Marques, F.C., Berry, J.J., Tumas, W., Lany, S., Stevanović, V., Toney, M.F., Buonassisi, T., 2017. Perovskite-Inspired Photovoltaic Materials: Toward Best Practices in Materials Characterization and Calculations. Chem. Mater. 29, 1964–1988. https://doi.org/10.1021/acs.chemmater.6b03852

Hu, Y., Chu, Y., Wang, Q., Zhang, Z., Ming, Y., Mei, A., Rong, Y., Han, H., 2019. Standardizing Perovskite Solar Modules beyond Cells. Joule. https://doi.org/10.1016/j.joule.2019.08.015

Huang, F., Li, M., Siffalovic, P., Cao, G., Tian, J., 2019. From scalable solution fabrication of perovskite films towards commercialization of solar cells. Energy Environ. Sci. https://doi.org/10.1039/c8ee03025a

IEC 60891, 2009. Photovoltaic devices – Procedures for temperature and irradiance corrections to measured I-V, Order A Journal On The Theory Of Ordered Sets And Its Applications.

IEC 61215-1-2, 2004. Terrestrial photovoltaic (PV) modules – Design qualification and type approval – Part 1-2: Special requirements for testing of thin-film Cadmium Telluride (CdTe) based photovoltaic (PV) modules.

IEC 61215, 2003. Crystalline silicon terrestrial photovoltaic (PV) modules – Design qualification and type approval, International Electrotechnical Committee.

IEC 61646, 2008. Thin-film terrestrial photovoltaic (PV) modules- Design qualification and type approval, International Electrotechnical Committee.

IEC 61853-1, 2011. Photovoltaic (PV) module performance testing and energy rating - Part 1: Irradiance and temperature performance measurements and power rating, International Electrotechnical Committee.

IEC 61853-2, 2016. Photovoltaic (PV) module performance testing and energy rating-Part 2_ Spectral responsivity, incidence angle and module operating temperature measurements.

Ishibashi, K., Kimura, Y., Niwano, M., 2008. An extensively valid and stable method for derivation of all parameters of a solar cell from a single current-voltage characteristic. J. Appl. Phys. 103, 094507. https://doi.org/10.1063/1.2895396

Islam, M.B., Yanagida, M., Shirai, Y., Nabetani, Y., Miyano, K., 2017. NiO x Hole Transport Layer for Perovskite Solar Cells with Improved Stability and Reproducibility. ACS Omega 2, 2291–2299. https://doi.org/10.1021/acsomega.7b00538

Jain, A., Kapoor, A., 2005. A new method to determine the diode ideality factor of real solar cell using Lambert W-function. Sol. Energy Mater. Sol. Cells 85, 391–396. https://doi.org/10.1016/j.solmat.2004.05.022

Karatepe, E., Boztepe, M., Colak, M., 2006. Neural network based solar cell model. Energy Convers. Manag. 47, 1159–1178. https://doi.org/10.1016/j.enconman.2005.07.007

Kendig, M., Scully, J.R., 1990. Basic aspects of electrochemical impedance application for the life prediction of organic coatings on metals. Corrosion 46, 22–29. https://doi.org/10.5006/1.3585061

Kern, R., Sastrawan, R., Ferber, J., Stangl, R., Luther, J., 2002. Modeling and interpretation of electrical impedance spectra of dye solar cells operated under open-circuit conditions. Electrochim. Acta 47, 4213–4225. https://doi.org/10.1016/S0013-4686(02)00444-9

Kerr, M.J., Cuevas, A., 2004. Generalized analysis of the illumination intensity vs. open-circuit voltage of solar cells. Sol. Energy 76, 263–267. https://doi.org/10.1016/j.solener.2003.07.027

Khadka, D.B., Shirai, Y., Yanagida, M., Miyano, K., 2018. Degradation of encapsulated perovskite solar cells driven by deep trap states and interfacial deterioration. J. Mater. Chem. C 6, 162–170. https://doi.org/10.1039/C7TC03733C

Khan, F., Baek, S.-H., Park, Y., Kim, J.H., 2013. Extraction of diode parameters of silicon solar cells under high illumination conditions. Energy Convers. Manag. 76, 421–429. https://doi.org/10.1016/j.enconman.2013.07.054

Khenkin, M. V., Anoop, K.M., Visoly-Fisher, I., Galagan, Y., Di Giacomo, F., Patil, B.R.R., Sherafatipour, G., Turkovic, V., Rubahn, H.-G.G., Madsen, M., Merckx, T., Uytterhoeven, G., Bastos, J.P.J.P.A., Aernouts, T., Brunetti, F., Lira-Cantu, M., Katz, E.A., Glagan, Y., Di Giacomo, F., Patil, B.R.R., Sherafatipour, G., Turkovic, V., Rubahn, H.-G.G., Madsen, M., Merckx, T., Uytterhoeven, G., Bastos, J.P.J.P.A., Aernouts, T., Brunetti, F., Lira-Cantu, M., Katz, E.A., 2018. Reconsidering figures of merit for performance and stability of perovskite photovoltaics. Energy Environ. Sci. 11, 739–743. https://doi.org/10.1039/c7ee02956j

Khenkin, M. V., Katz, E.A., Abate, A., Bardizza, G., Berry, J.J., Brabec, C., Brunetti, F., Bulović, V., Burlingame, Q., Di Carlo, A., Cheacharoen, R., Cheng, Y.-B., Colsmann, A., Cros, S., Domanski, K., Dusza, M., Fell, C.J., Forrest, S.R., Galagan, Y., Di Girolamo, D., Grätzel, M., Hagfeldt, A., von Hauff, E., Hoppe, H., Kettle, J., Köbler, H., Leite, M.S., Liu, S., Loo, Y.-L., Luther, J.M., Ma, C.-Q., Madsen, M., Manceau, M., Matheron, M., McGehee, M., Meitzner, R., Nazeeruddin, M.K., Nogueira, A.F., Odabaşı, Ç., Osherov, A., Park, N.-G., Reese, M.O., De Rossi, F., Saliba, M., Schubert, U.S., Snaith, H.J., Stranks, S.D., Tress, W., Troshin, P.A., Turkovic, V., Veenstra, S., Visoly-Fisher, I., Walsh, A., Watson, T., Xie, H., Yıldırım, R., Zakeeruddin, S.M., Zhu, K., Lira-Cantu, M., 2020. Consensus statement for stability assessment and reporting for perovskite photovoltaics based on ISOS procedures. Nat. Energy 5, 35–49. https://doi.org/10.1038/s41560-019-0529-5

Lee, H., Lee, C., Song, H.-J., 2019. Influence of Electrical Traps on the Current Density Degradation of Inverted Perovskite Solar Cells. Materials (Basel). 12, 1644. https://doi.org/10.3390/ma12101644

Li, C., Guerrero, A., Huettner, S., Bisquert, J., 2018. Unravelling the role of vacancies in lead halide perovskite through electrical switching of photoluminescence. Nat. Commun. 9, 5113. https://doi.org/10.1038/s41467-018-07571-6

Li, C., Guerrero, A., Zhong, Y., Huettner, S., 2017. Origins and mechanisms of hysteresis in

organometal halide perovskites. J. Phys. Condens. Matter 29, 193001. https://doi.org/10.1088/1361-648X/aa626d

Li, J., Dewi, H.A., Wang, H., Lew, J.H., Mathews, N., Mhaisalkar, S., Bruno, A., 2020. Design of Perovskite Thermally Co-Evaporated Highly Efficient Mini-Modules with High Geometrical Fill Factors. Sol. RRL 4, 2000473. https://doi.org/10.1002/solr.202000473

Li, Y., Huang, W., Huang, H., Hewitt, C., Chen, Y., Fang, G., Carroll, D.L., 2013. Evaluation of methods to extract parameters from current–voltage characteristics of solar cells. Sol. Energy 90, 51–57. https://doi.org/10.1016/j.solener.2012.12.005

Liu, Z., Qiu, L., Ono, L.K., He, S., Hu, Z., Jiang, M., Tong, G., Wu, Z., Jiang, Y., Son, D., Dang, Y., Kazaoui, S., Qi, Y., 2020. A holistic approach to interface stabilization for efficient perovskite solar modules with over 2,000-hour operational stability. Nat. Energy. https://doi.org/10.1038/s41560-020-0653-2

Ma, C., Shen, D., Qing, J., Thachoth Chandran, H., Lo, M.-F., Lee, C.-S., 2017. Effects of Small Polar Molecules (MA + and H 2 O) on Degradation Processes of Perovskite Solar Cells. ACS Appl. Mater. Interfaces 9, 14960–14966. https://doi.org/10.1021/acsami.7b01348

Makrides, G., Zinsser, B., Georghiou, G.E., Schubert, M., Werner, J.H., 2008. Outdoor efficiency of different photovoltaic systems installed in Cyprus and Germany, in: 2008 33rd IEEE Photovolatic Specialists Conference. IEEE, pp. 1–6. https://doi.org/10.1109/PVSC.2008.4922830

Makrides, G., Zinsser, B., Norton, M., E., G., 2012. Performance of Photovoltaics Under Actual Operating Conditions, in: Third Generation Photovoltaics. InTech. https://doi.org/10.5772/27386

Makrides, G., Zinsser, B., Schubert, M., Georghiou, G.E., 2014. Performance loss rate of twelve photovoltaic technologies under field conditions using statistical techniques. Sol. Energy 103, 28–42. https://doi.org/10.1016/j.solener.2014.02.011

Marinova, N., Tress, W., Humphry-Baker, R., Dar, M.I., Bojinov, V., Zakeeruddin, S.M., Nazeeruddin, M.K., Grätzel, M., 2015. Light Harvesting and Charge Recombination in CH 3 NH 3 PbI 3 Perovskite Solar Cells Studied by Hole Transport Layer Thickness Variation. ACS Nano 9, 4200–4209. https://doi.org/10.1021/acsnano.5b00447

McLeod, J.A., Liu, L., 2018. Prospects for Mitigating Intrinsic Organic Decomposition in Methylammonium Lead Triiodide Perovskite. J. Phys. Chem. Lett. 9, 2411–2417. https://doi.org/10.1021/acs.jpclett.8b00323

Meeker, W., Hong, Y., Escobar, L., 2011. Degradation Models and Analyses, in: Encyclopedia of Statistical Sciences. John Wiley & Sons, Inc., Hoboken, NJ, USA, pp. 1–23. https://doi.org/10.1002/0471667196.ess7148

Mellit, A., Kalogirou, S.A., 2008. Artificial intelligence techniques for photovoltaic applications: A review. Prog. Energy Combust. Sci. 34, 574–632. https://doi.org/10.1016/j.pecs.2008.01.001

Meyers, B., Deceglie, M., Deline, C., Jordan, D., 2020. Signal Processing on PV Time-Series Data: Robust Degradation Analysis Without Physical Models. IEEE J. Photovoltaics 10, 546–553. https://doi.org/10.1109/JPHOTOV.2019.2957646

Mialhe, P., Charles, J.P., Khoury, A., Bordure, G., 1986. The diode quality factor of solar cells under illumination. J. Phys. D. Appl. Phys. 19, 483–492. https://doi.org/10.1088/0022-3727/19/3/018

Moon, S.J., Yum, J.H., Lofgren, L., Walter, A., Sansonnens, L., Benkhaira, M., Nicolay, S., Bailat, J., Ballif, C., 2015. Laser-Scribing Patterning for the Production of Organometallic Halide Perovskite Solar Modules. IEEE J. Photovoltaics 5, 1087–1092. https://doi.org/10.1109/JPHOTOV.2015.2416913

Motti, S.G., Meggiolaro, D., Barker, A.J., Mosconi, E., Perini, C.A.R., Ball, J.M., Gandini, M., Kim, M., De Angelis, F., Petrozza, A., 2019. Controlling competing photochemical reactions stabilizes perovskite solar cells. Nat. Photonics 13, 532–539. https://doi.org/10.1038/s41566-019-0435-1

Murayama, M., Mori, T., 2006. Equivalent Circuit Analysis of Dye-Sensitized Solar Cell by Using One-Diode Model: Effect of Carboxylic Acid Treatment of TiO 2 Electrode. Jpn. J. Appl. Phys. 45, 542–545. https://doi.org/10.1143/JJAP.45.542

Nikoletatos, J., Halambalakis, G., 2018. Standards, Calibration, and Testing of PV Modules and Solar Cells, in: McEvoy's Handbook of Photovoltaics. Elsevier, pp. 452–467. https://doi.org/10.1016/B978-0-12-809921-6.00033-1

Oliveira, M.C.C. de, Diniz Cardoso, A.S.A., Viana, M.M., Lins, V. de F.C., 2018. The causes and effects of degradation of encapsulant ethylene vinyl acetate copolymer (EVA) in crystalline silicon photovoltaic modules: A review. Renew. Sustain. Energy Rev. 81, 2299–2317. https://doi.org/10.1016/j.rser.2017.06.039

Osterwald, C.R., Glatfelter, T., Burdick, J., 1987. COMPARISON OF THE TEMPERATURE COEFFICIENTS OF THE BASIC I-V PARAMETERS FOR VARIOUS TYPES OF SOLAR CELLS., in: Conference Record of the IEEE Photovoltaic Specialists Conference. pp. 188–193.

Osterwald, C.R., McMahon, T.J., 2009. History of accelerated and qualification testing of terrestrial photovoltaic modules: A literature review. Prog. Photovoltaics Res. Appl. 17, 11–33. https://doi.org/10.1002/pip.861

Papageorgas, P., Piromalis, D., Valavanis, T., Kambasis, S., Iliopoulou, T., Vokas, G., 2015. A low-cost and fast PV I-V curve tracer based on an open source platform with M2M communication capabilities for preventive monitoring. Energy Procedia 74, 423–438. https://doi.org/10.1016/j.egypro.2015.07.641

Phang, J.C.H., Chan, D.S.H., Phillips, J.R., 1984. Accurate analytical method for the extraction of solar cell model parameters. Electron. Lett. 20, 406. https://doi.org/10.1049/el:19840281

Phinikarides, A., Kindyni, N., Makrides, G., Georghiou, G.E., 2014. Review of photovoltaic degradation rate methodologies. Renew. Sustain. Energy Rev. 40, 143–152. https://doi.org/10.1016/j.rser.2014.07.155

Pitarch-Tena, D., Ngo, T.T., Vallés-Pelarda, M., Pauporté, T., Mora-Seró, I., 2018. Impedance Spectroscopy Measurements in Perovskite Solar Cells: Device Stability and Noise Reduction. ACS Energy Lett. 3–7. https://doi.org/10.1021/ACSENERGYLETT.8B00465

Qiu, L., He, S., Ono, L.K., Liu, S., Qi, Y., 2019. Scalable Fabrication of Metal Halide Perovskite Solar Cells and Modules. ACS Energy Lett. https://doi.org/10.1021/acsenergylett.9b01396

Ramirez, D., Schutt, K., Montoya, J.F., Mesa, S., Lim, J., Snaith, H.J., Jaramillo, F., 2018a. Meso-Superstructured Perovskite Solar Cells: Revealing the Role of the Mesoporous Layer. J. Phys. Chem. C 122, 21239–21247. https://doi.org/10.1021/acs.jpcc.8b07124

Ramirez, D., Uribe, J.I., Francaviglia, L., Romero-Gomez, P., Fontcuberta i Morral, A., Jaramillo, F., 2018b. Photophysics behind highly luminescent two-dimensional hybrid perovskite ($CH_3(CH_2)_2NH_3)_2(CH_3NH_3)_2Pb_3Br_{10}$ thin films. J. Mater. Chem. C. https://doi.org/10.1039/C8TC01582A

Ramirez, D., Velilla, E., Montoya, J.F.J.F., Jaramillo, F., 2019. Mitigating scalability issues of perovskite photovoltaic technology through a p-i-n meso-superstructured solar cell architecture. Sol. Energy Mater. Sol. Cells 195, 191–197. https://doi.org/10.1016/j.solmat.2019.03.014

Riquelme, A., Bennett, L.J., Courtier, N.E., Wolf, M.J., Contreras-Bernal, L., Walker, A., Richardson, G., Anta, J.A., 2020. Deducing the key physical properties of a perovskite solar cell from its impedance response: insights from drift-diffusion modelling. Appl. Phys.

Santakrus Singh, N., Jain, A., Kapoor, A., 2009. Determination of the solar cell junction ideality factor using special trans function theory (STFT). Sol. Energy Mater. Sol. Cells 93, 1423–1426. https://doi.org/10.1016/j.solmat.2009.03.013

Schwenzer, J.A., Rakocevic, L., Gehlhaar, R., Abzieher, T., Gharibzadeh, S., Moghadamzadeh, S., Quintilla, A., Richards, B.S., Lemmer, U., Paetzold, U.W., 2018. Temperature Variation-Induced Performance Decline of Perovskite Solar Cells. ACS Appl. Mater. Interfaces 10, 16390–16399. https://doi.org/10.1021/acsami.8b01033

Shao, G., Glaz, M.S., Ma, F., Ju, H., Ginger, D.S., 2014. Intensity-Modulated Scanning Kelvin Probe Microscopy Intensity-Modulated Scanning Kelvin Probe Microscopy for Probing Recombination in Organic Photovoltaics 10799–10807. https://doi.org/10.1021/nn5045867

Shi, L., Young, T.L., Kim, J., Sheng, Y., Wang, L., Chen, Y., Feng, Z., Keevers, M.J., Hao, X., Verlinden, P.J., Green, M.A., Ho-Baillie, A.W.Y., 2017. Accelerated Lifetime Testing of Organic-Inorganic Perovskite Solar Cells Encapsulated by Polyisobutylene. ACS Appl. Mater. Interfaces 9, 25073–25081. https://doi.org/10.1021/acsami.7b07625

Stoichkov, V., Bristow, N., Troughton, J., De Rossi, F., Watson, T.M., Kettle, J., 2018. Outdoor performance monitoring of perovskite solar cell mini-modules: Diurnal performance, observance of reversible degradation and variation with climatic performance. Sol. Energy 170, 549–556. https://doi.org/10.1016/j.solener.2018.05.086

Toledo, F.J., Blanes, J.M., 2016. Analytical and quasi-explicit four arbitrary point method for extraction of solar cell single-diode model parameters. Renew. Energy 92, 346–356. https://doi.org/10.1016/j.renene.2016.02.012

Tress, W., Domanski, K., Carlsen, B., Agarwalla, A., Alharbi, E.A., Graetzel, M., Hagfeldt, A., 2019. Performance of perovskite solar cells under simulated temperature-illumination real-world operating conditions. Nat. Energy 4, 568–574. https://doi.org/10.1038/s41560-019-0400-8

Tress, W., Yavari, M., Domanski, K., Yadav, P., Niesen, B., Correa Baena, J.P., Hagfeldt, A., Graetzel, M., 2018. Interpretation and evolution of open-circuit voltage, recombination, ideality factor and subgap defect states during reversible light-soaking and irreversible degradation of perovskite solar cells. Energy Environ. Sci. 11, 151–165. https://doi.org/10.1039/C7EE02415K

Van Dyk, E.E., Gxasheka, A.R., Meyer, E.L., 2005. Monitoring current-voltage characteristics and energy output of silicon photovoltaic modules. Renew. Energy 30, 399–411. https://doi.org/10.1016/j.renene.2004.04.016

Velilla, E., Cano, J., Jimenez, K., Valencia, J., Ramirez, D., Jaramillo, F., 2018. Numerical Analysis to Determine Reliable One-Diode Model Parameters for Perovskite Solar Cells. Energies 11, 1963. https://doi.org/10.3390/en11081963

Velilla, E., Cano, J.B.J.B., Jaramillo, F., 2019a. Monitoring system to evaluate the outdoor performance of solar devices considering the power rating conditions. Sol. Energy 194, 79–85. https://doi.org/10.1016/j.solener.2019.10.051

Velilla, E., Jaramillo, F., Mora-Seró, I., 2021. High-throughput analysis of the ideality factor to evaluate the outdoor performance of perovskite solar minimodules. Nat. Energy 6, 54–62. https://doi.org/10.1038/s41560-020-00747-9

Velilla, E., Ramirez, D., Uribe, J.-I.J.-I., Montoya, J.F.J.F., Jaramillo, F., 2019b. Outdoor performance of perovskite solar technology: Silicon comparison and competitive advantages at different irradiances. Sol. Energy Mater. Sol. Cells 191, 15–20. https://doi.org/10.1016/j.solmat.2018.10.018

Velilla, E., Restrepo, S., Jaramillo, F., 2017. Cluster analysis of commercial photovoltaic modules based on the electrical performance at standard test conditions. Sol. Energy 144, 335–341. https://doi.org/10.1016/j.solener.2017.01.037

Velilla, E., Valencia, J., Jaramillo, F., 2014. Performance evaluation of two solar photovoltaic technologies under atmospheric exposure using artificial neural network models. Sol. Energy 107, 260–271. https://doi.org/10.1016/j.solener.2014.04.033

Visa, I., Burduhos, B., Neagoe, M., Moldovan, M., Duta, A., 2016. Comparative analysis of the infield response of five types of photovoltaic modules. Renew. Energy 95, 178–190. https://doi.org/10.1016/j.renene.2016.04.003

Wang, E., Yang, H.E., Yen, J., Chi, S., Wang, C., 2013. Failure modes evaluation of PV module via materials degradation approach. Energy Procedia 33, 256–264. https://doi.org/10.1016/j.egypro.2013.05.066

Wang, M., Ma, X., Huang, W.H., Liu, J., Curran, A.J., Schnabel, E., Köhl, M., Davis, K.O., Brynjarsdóttir, J., Braid, J.L., French, R.H., 2018. Evaluation of Photovoltaic Module Performance Using Novel Data-driven I-V Feature Extraction and Suns-V OC Determined from Outdoor Time-Series I-V Curves, in: 2018 IEEE 7th World Conference on Photovoltaic Energy Conversion, WCPEC 2018 - A Joint Conference of 45th IEEE PVSC, 28th PVSEC and 34th EU PVSEC. IEEE, pp. 778–783. https://doi.org/10.1109/PVSC.2018.8547772

Wang, Q., Gra, M., 2005. Electrochemical Impedance Spectroscopic Analysis of Dye-Sensitized Solar Cells. Response 14945–14953.

Wetzelaer, G.-J.A.H., Scheepers, M., Sempere, A.M., Momblona, C., Ávila, J., Bolink, H.J., 2015. Trap-Assisted Non-Radiative Recombination in Organic-Inorganic Perovskite Solar Cells. Adv. Mater. 27, 1837–1841. https://doi.org/10.1002/adma.201405372

Willoughby, A.A., Omotosho, T. V., Aizebeokhai, A.P., 2014. A simple resistive load I-V curve tracer for monitoring photovoltaic module characteristics. IREC 2014 - 5th Int. Renew. Energy Congr. 1–6. https://doi.org/10.1109/IREC.2014.6827028

Willoughby, A.A., Osinowo, M.O., 2018. Development of an electronic load I-V curve tracer to investigate the impact of Harmattan aerosol loading on PV module performance in southwest Nigeria. Sol. Energy 166, 171–180. https://doi.org/10.1016/j.solener.2018.03.047

Wojciechowski, K., Leijtens, T., Siprova, S., Schlueter, C., Hörantner, M.T., Wang, J.T.-W., Li, C.-Z., Jen, A.K.Y., Lee, T.-L., Snaith, H.J., 2015. C 60 as an Efficient n-Type Compact Layer in Perovskite Solar Cells. J. Phys. Chem. Lett. 6, 2399–2405. https://doi.org/10.1021/acs.jpclett.5b00902

Yang, B., Suo, J., Mosconi, E., Ricciarelli, D., Tress, W., De Angelis, F., Kim, H.-S., Hagfeldt, A., 2020. Outstanding Passivation Effect by a Mixed-Salt Interlayer with Internal Interactions in Perovskite Solar Cells. ACS Energy Lett. 5, 3159–3167. https://doi.org/10.1021/acsenergylett.0c01664

Yang, J., Siempelkamp, B.D., Liu, D., Kelly, T.L., 2015. Investigation of CH 3 NH 3 PbI 3 Degradation Rates and Mechanisms in Controlled Humidity Environments Using in Situ Techniques. ACS Nano 9, 1955–1963. https://doi.org/10.1021/nn506864k

Yoo, S.-M., Lee, S.-Y., Kim, G., Hernandez, E.V., Mora-Seró, I., Yoon, S.J., Shin, T., Lee, S.-H., Ahn, S., Song, M.-K., Kim, M., Lee, H.J., 2021. Preparation of nanoscale inorganic CsPbIxBr3-x perovskite photosensitizers on the surface of mesoporous TiO2 film for solid-state sensitized solar cells. Appl. Surf. Sci. 551, 149387. https://doi.org/10.1016/j.apsusc.2021.149387

Yoo, S.-M., Lee, S., Velilla Hernandez, E., Kim, M., Kim, G., Shin, T., Nazeeruddin, M.K., Mora-Seró, I., Lee, H.J., 2020. Nanoscale Perovskite-Sensitized Solar Cell Revisited: Dye-Cell or Perovskite-Cell? ChemSusChem 13, 2571–2576. https://doi.org/10.1002/cssc.202000223

Yoo, S.-M., Yoon, S.J., Anta, J.A., Lee, H.J., Boix, P.P., Mora-Seró, I., 2019. An Equivalent Circuit for Perovskite Solar Cell Bridging Sensitized to Thin Film Architectures. Joule 3, 2535–2549. https://doi.org/10.1016/j.joule.2019.07.014

Zagrouba, M., Sellami, A., Bouaïcha, M., Ksouri, M., 2010. Identification of PV solar cells and modules parameters using the genetic algorithms: Application to maximum power extraction. Sol. Energy 84, 860–866. https://doi.org/10.1016/j.solener.2010.02.012

Zarazua, I., Han, G., Boix, P.P., Mhaisalkar, S., Fabregat-Santiago, F., Mora-Seró, I., Bisquert, J., Garcia-Belmonte, G., 2016. Surface Recombination and Collection Efficiency in Perovskite Solar Cells from Impedance Analysis. J. Phys. Chem. Lett. 7, 5105–5113. https://doi.org/10.1021/acs.jpclett.6b02193

Zhang, S., Liu, Z., Zhang, W., Jiang, Z., Chen, Weitao, Chen, R., Huang, Y., Yang, Z., Zhang, Y., Han, L., Chen, Wei, 2020. Barrier Designs in Perovskite Solar Cells for Long-Term Stability. Adv. Energy Mater. 2001610, 2001610. https://doi.org/10.1002/aenm.202001610

Zhao, L., Kerner, R.A., Xiao, Z., Lin, Y.L., Lee, K.M., Schwartz, J., Rand, B.P., 2016. Redox Chemistry Dominates the Degradation and Decomposition of Metal Halide Perovskite Optoelectronic Devices. ACS Energy Lett. 1, 595–602. https://doi.org/10.1021/acsenergylett.6b00320

Zhao, Y., Zhou, W., Tan, H., Fu, R., Li, Q., Lin, F., Yu, D., Walters, G., Sargent, E.H., Zhao, Q., 2017. Mobile-Ion-Induced Degradation of Organic Hole-Selective Layers in Perovskite Solar Cells. J. Phys. Chem. C 121, 14517–14523. https://doi.org/10.1021/acs.jpcc.7b04684